



AFRL-RB-WP-TR-2008-3171

**UNIQUE STEALTH UNMANNED AERIAL VEHICLE
(UAV) HOUCK AIRCRAFT DESIGN PROGRAM
Volume 2: Prototype Report**

Timothy Fry

University of Dayton

**NOVEMBER 2008
Final Report**

Approved for public release; distribution unlimited.

See additional restrictions described on inside pages

STINFO COPY

**AIR FORCE RESEARCH LABORATORY
AIR VEHICLES DIRECTORATE
WRIGHT-PATTERSON AIR FORCE BASE, OH 45433-7542
AIR FORCE MATERIEL COMMAND
UNITED STATES AIR FORCE**

NOTICE

Using Government drawings, specifications, or other data included in this document for any purpose other than Government procurement does not in any way obligate the U.S. Government. The fact that the Government formulated or supplied the drawings, specifications, or other data does not license the holder or any other person or corporation; or convey any rights or permission to manufacture, use, or sell any patented invention that may relate to them.

This report was cleared for public release by the Air Force Research Laboratory Wright-Patterson Air Force Base (WPAFB) Public Affairs Office and is available to the general public, including foreign nationals. Copies may be obtained from the Defense Technical Information Center (DTIC) (<http://www.dtic.mil>).

AFRL-RB-WP-TR-2008-3171 HAS BEEN REVIEWED AND IS APPROVED FOR PUBLICATION IN ACCORDANCE WITH THE ASSIGNED DISTRIBUTION STATEMENT.

//signature//

CALE H. ZEUNE
Aerospace Engineer
Aerodynamic Configuration Branch
Aeronautical Sciences Division

//signature//

CHRISTOPHER P. GREEK
Chief
Aerodynamic Configuration Branch
Aeronautical Sciences Division

//signature//

DR. CARL TILMANN
Technical Advisor
Aerodynamic Configuration Branch
Aeronautical Sciences Division

This report is published in the interest of scientific and technical information exchange and its publication does not constitute the Government's approval or disapproval of its ideas or findings.

*Disseminated copies will show "//signature//" stamped or typed above the signature blocks.

REPORT DOCUMENTATION PAGE

Form Approved
OMB No. 0704-0188

The public reporting burden for this collection of information is estimated to average 1 hour per response, including the time for reviewing instructions, searching existing data sources, gathering and maintaining the data needed, and completing and reviewing the collection of information. Send comments regarding this burden estimate or any other aspect of this collection of information, including suggestions for reducing this burden, to Department of Defense, Washington Headquarters Services, Directorate for Information Operations and Reports (0704-0188), 1215 Jefferson Davis Highway, Suite 1204, Arlington, VA 22202-4302. Respondents should be aware that notwithstanding any other provision of law, no person shall be subject to any penalty for failing to comply with a collection of information if it does not display a currently valid OMB control number. **PLEASE DO NOT RETURN YOUR FORM TO THE ABOVE ADDRESS.**

1. REPORT DATE (DD-MM-YY) November 2008	2. REPORT TYPE Final	3. DATES COVERED (From - To) 01 January 2006 – 01 May 2008
---	--------------------------------	--

4. TITLE AND SUBTITLE UNIQUE STEALTH UNMANNED AERIAL VEHICLE (UAV) HOUCK AIRCRAFT DESIGN PROGRAM Volume 2: Prototype Report	5a. CONTRACT NUMBER FA8652-05-3-9017
	5b. GRANT NUMBER
	5c. PROGRAM ELEMENT NUMBER 0602201

6. AUTHOR(S) Timothy Fry	5d. PROJECT NUMBER A0AA
	5e. TASK NUMBER
	5f. WORK UNIT NUMBER 0A

7. PERFORMING ORGANIZATION NAME(S) AND ADDRESS(ES) University of Dayton 300 College Park Dayton, OH 45469-0210	8. PERFORMING ORGANIZATION REPORT NUMBER
--	---

9. SPONSORING/MONITORING AGENCY NAME(S) AND ADDRESS(ES) Air Force Research Laboratory Air Vehicles Directorate Wright-Patterson Air Force Base, OH 45433-7542 Air Force Materiel Command United States Air Force	10. SPONSORING/MONITORING AGENCY ACRONYM(S) AFRL/RBAA
	11. SPONSORING/MONITORING AGENCY REPORT NUMBER(S) AFRL-RB-WP-TR-2008-3171

12. DISTRIBUTION/AVAILABILITY STATEMENT Approved for public release; distribution unlimited.
--

13. SUPPLEMENTARY NOTES Report contains color. PAO case number AFMC-2008-0082; cleared 06 January 2009. See also Volume 1 (AFRL-RB-WP-TR-2008-3170).
--

14. ABSTRACT This report covers the collaborative activities conducted under the leadership of the University of Dayton Research Institute on the Unique Stealth Unmanned Aerial Vehicle (UAV) Houck Aircraft Design Program. This was organized in five phases: aerodynamic evaluation of 6-inch model; aerodynamic evaluation of 24-inch model; design exploration for the Preferred System Concept; design of Preferred System Concept; and fabrication of flying prototype aircraft. Overall, this configuration, as modeled, was found not to have aerodynamic characteristics markedly better than existing small unmanned aircraft. It may have potential to show benefit over existing aircraft in other areas though, including structural weight required as a result of the joined tips, size required to package the aircraft for man-portability due to its limited span, and range of c.g. travel owing to large longitudinal wing spacing for trim. To understand potential benefits in these areas, these characteristics would need to be assessed in further studies using different, higher fidelity methods.
--

15. SUBJECT TERMS Houck, biplane, end plates, flow guides, wing tips, gap, stagger, low Reynold's number, prototype, UAV construction

16. SECURITY CLASSIFICATION OF:			17. LIMITATION OF ABSTRACT: SAR	18. NUMBER OF PAGES 156	19a. NAME OF RESPONSIBLE PERSON (Monitor) Cale H. Zeune 19b. TELEPHONE NUMBER (Include Area Code) (937) 255-0161
a. REPORT Unclassified	b. ABSTRACT Unclassified	c. THIS PAGE Unclassified			

Table of Contents

Section	Page
List of Figures	v
List of Tables	vii
Preface.....	viii
Acknowledgements.....	x
Executive Summary	1
1 Phase I: Aerodynamic Evaluation of the 6-inch Model	3
1.1 Introduction	3
1.2 Configuration Data.....	5
1.3 CAD Modeling.....	7
1.4 Aerodynamic Analysis	15
1.4.1 Wind Tunnel Analysis	15
1.4.2 AVUS CFD Analysis.....	31
1.4.3 FLUENT CFD Analysis	39
1.5 Results	46
1.6 Conclusions	47
2 Phase II: Aerodynamic Evaluation of the 24-inch Model.....	49
2.1 Introduction	49
2.2 Configuration Data.....	49
2.3 CAD Modeling.....	51
2.4 Aerodynamic Analysis	54
2.4.1 Wind Tunnel Analysis	54
2.4.2 Hot Wire Analysis.....	56
2.4.3 AVUS CFD Analysis.....	58
2.5 Results	67
2.6 Conclusions	67
3 Phase III & IV: Design Activities for the Preferred System Concept.....	68
3.1 Introduction	68
3.2 Mission Analysis	69
3.3 Configuration Data.....	71
3.4 Aerodynamic Analysis	75
3.5 Structural Analysis	81
3.6 Results	84
3.7 Conclusions	84
4 Phase V: Fabrication of Flying Prototype Aircraft	85
4.1 Summary	85
4.2 Build Notes.....	86
4.3 UAV Components.....	88
4.4 Recommendations	89
References.....	91
Appendix A: AFIT 24” Houck Model Data (Wind Tunnel & Hot Wire Results).....	92
Appendix B: Initial Aircraft Sizing Data by Mission	104

Appendix C: Interim Designs and Details in Configuration Development	109
Appendix D: VSAERO Evaluation Document.....	120
Appendix E: L/D_{\max} Calculations for Houck Concept.....	122
Appendix F: Houck UAV Prototype Design	126
Appendix G: Houck UAV Prototype Construction Methodology.....	133

List of Figures

Figure	Page
Figure 1: Sketch of Houck Airfoil Concept.....	3
Figure 2: Evaluation Model of Houck Airfoil	6
Figure 3: Picture of Laser Scan Geometry.....	7
Figure 4: Image from Original .STL Mesh of Airfoil.....	8
Figure 5: Chordwise Section Curves (a) and Section Detail (b).....	8
Figure 6: Surface Discontinuities: Quilted-surface Modeling Method.....	9
Figure 7: Chordwise Section Curves Using Unigraphics NX3	10
Figure 8: NX3 Modeling Approach for the Houck Six-inch Airfoil	11
Figure 9: GAMBIT Views of Airfoil Geometry.....	13
Figure 10: Three-View Drawing of 6" Houck Configuration.....	14
Figure 11: University of Dayton Low Speed Wind Tunnel.....	17
Figure 12: Houck Model Mounted in the UD LSWT.....	19
Figure 13: Lift Curves for the 6-inch Houck Model.....	20
Figure 14: Drag Coefficient Variation with Angle of Attack	21
Figure 15: Drag Polar for the Houck Configuration.....	21
Figure 16: Lift to Drag Ratio for the 6-inch Model Houck Configuration	22
Figure 17: Lift to Drag Ratio for the 15-inch Model Houck Configuration	23
Figure 18: Wake at 15 MPH for AOA = 6, 20 degrees	27
Figure 19: Wake at 35 MPH for AOA = 6, 20 degrees	28
Figure 20: Wake at 55 MPH for AOA = 6, 14, 20, 20 degrees	29
Figure 21: Leading Edge Vortex at 15 and 35 MPH and AOA = 20 degrees	30
Figure 22: Houck-Designed Six-inch Joined-Wing Aircraft.....	32
Figure 23: Computational Mesh Generated by AFRL/RBAC.....	32
Figure 24: Surface Pressure for the Coarse and Refined Grids	33
Figure 25: Mach Number Contours for the Coarse and Refined Grids	34
Figure 26: Surface Pressure: Inverted Configuration, Top View	35
Figure 27: Surface Pressure: Inverted Configuration, Bottom view.....	35
Figure 28: Planar Mach Number: Inverted Configuration, Front View	36
Figure 29: Lift to Drag Ratio versus AOA	37
Figure 30: Lift Coefficient versus AOA	37
Figure 31: Drag Coefficient versus AOA	38
Figure 32: Lift Coefficient versus Drag Coefficient.....	38
Figure 33: GAMBIT Mesh of the 6-inch Airfoil	40
Figure 34: Static Pressure Contours for 45 mph, AOA = 8°.....	42
Figure 35: CFD and Test Results for Lift and Drag Characteristics.....	44
Figure 36: Spanwise Section Cuts Illustrating Lack of Airfoil Camber	45
Figure 37: Houck Evaluation Model for Phase II.....	50
Figure 38: Inertial Data for Phase II Evaluation Model	51
Figure 39: Illustration of Coarse Edges in Scanned Model	52
Figure 40: Illustration of Initial Trailing Edge Definition.....	52
Figure 41: Rebuilding of the Fuselage Body	53
Figure 42: Lofted Curves Used to Rebuild Wing Surfaces	53

Figure 43: Angle of Attack Range Used in Wind Tunnel Testing	55
Figure 44: Lift Over Drag vs. AOA Wind Tunnel Results.....	56
Figure 45: Path of the Hot Wire Probe	57
Figure 46: Three Views of the Hot Wire Data Collection Zone.....	57
Figure 47: Sample Result of Hot Wire Testing	58
Figure 48: Computational Mesh Used by AFRL/RBAC.....	59
Figure 49: Example of Surface Imperfection.....	60
Figure 50: Initial Comparison of CL and CD Results	61
Figure 51: Comparison of CL vs. CD Results	61
Figure 52: Updated Test Data with Angle of Attack Correction.....	62
Figure 53: Comparison of L/D vs. AOA Results.....	63
Figure 54: Comparison of Pitching Moment vs. AOA.....	63
Figure 55: Velocity Vectors at Mid-span for 5.2° AOA.....	64
Figure 56: Streamline Traces at 5.2° AOA	64
Figure 57: Streamline Traces at 13.2° AOA	64
Figure 58: Velocity Vectors at Mid-span for 10.2° AOA.....	65
Figure 59: Velocity Vectors at Mid-span for 11.2° AOA.....	65
Figure 60: Velocity Vectors at Mid-span for 12.2° AOA.....	66
Figure 61: Velocity Vectors at Mid-span for 13.2° AOA.....	66
Figure 62: Four Options for Trimming the Aircraft	73
Figure 63: Preferred System Concept Configuration.....	74
Figure 64: Gas vs. Electric Propulsion System.....	75
Figure 65: Comparative Analysis of VSAERO vs. FLUENT Analysis	76
Figure 66: Predicted Lift Performance of the Preferred System Concept	77
Figure 67: Predicted Drag Performance of the Preferred System Concept	77
Figure 68: Pitching Moment vs. AOA.....	78
Figure 69: Elevator Angle for Trim	78
Figure 70: Various Center of Gravity Locations	79
Figure 71: Directional Stability Analysis	80
Figure 72: Roll Stability Analysis.....	81
Figure 73: Stress Plot of Houck Wing Using ABAQUS	82
Figure 74: Deflection Plot of Houck Wing Using ABAQUS.....	83
Figure 75: Houck UAV Prototype	86
Figure 76: Alternate View of Houck UAV Prototype	86

List of Tables

Table	Page
Table 1: Theoretical/Empirical Models Used in Analysis	16
Table 2: Minimum Base Drag and Maximum Lift to Drag Ratio Values	24
Table 3: Lift Curve Slope and Span Efficiency Factor Results: 6-inch Model	24
Table 4: Lift Curve Slope and Span Efficiency Factor: Single Monoplane Assumption	26
Table 5: Performance of the Houck Configuration.....	47
Table 6: Wind Tunnel Testing Conditions and Geometric Parameters	55
Table 7: Potential Mission Profile Descriptions	70
Table 8: Summary of Mission and Airplane Sizes	71
Table 9: Properties of Glass filled Vectra.....	82

Preface

Ronald G. Houck II, owner of Iron Hawk Enterprises (IHE), LLC developed aerodynamic lifting shapes over a period of years through self-study of basic aerodynamic concepts. Mr. Houck's lifting concept, as incorporated into an aircraft configuration, combines an upper and lower wing joined at the tips with flow guides (curved endplates) with the intent of significantly reducing vortex losses caused by concentrated wing tip vortices. Mr. Houck began drawing and prototyping his concepts using Styrofoam. His designs were modified and evolved to improve flight dynamics within Mr. Houck's limited capability to evaluate these characteristics.

Two significant events occurred during 2004-2005 which improved the viability for future development of the concept. First, the uniqueness of Mr. Houck's lifting foil concept enabled the concept to be awarded a patent by the United States Patent and Trademark Office (USPTO). As of submission of this report, the concept's utility patent and three design patents have been awarded. Second, during a meeting with US Representative David Hobson (Ohio 7th Congressional District), Mr. Houck had the opportunity to discuss his lifting foil and its potential benefit to aviation as well as demonstrate the concept using his models. Because of his keen interest in aerospace advancement and military readiness, Mr. Hobson sponsored evaluation of the Houck concept by the Air Force Research Laboratory, Air Vehicles Directorate with funding through a FY05 \$1.1 million congressional addition to the budget. With the funding secured, the formal kickoff of the current research effort began in January 2005

The University of Dayton Research Institute (UDRI) and Iron Hawk Enterprises (IHE), LLC were contracted by Wright Brothers Institute (WBI) to perform research and development activities on the UAV Houck Aircraft Design, or "Houck Configuration" as it has come to be called, for the Air Force Research Laboratory Air Vehicles Directorate (AFRL/RB). The work was performed under WBI contracts WBSC 9017UDF&IHE and AFRL contract FA8652-03-3-0005. UDRI worked with WBI, IHE, and AFRL to perform computational modeling and wind tunnel testing of the concept. Wind tunnel and hot wire tests were performed by Air Force Institute of Technology (AFIT) students^{2,3}. The AFRL Computational Sciences Branch (AFRL/RBAC) performed subsequent CFD analyses on the configuration and compared the

results to those of the wind tunnel and hot wire tests. Stress Engineering Services, Inc. (SES) was also involved in modeling efforts, as well as fabrication of a prototype vehicle. The University of Dayton, under the guidance of Dr. Aaron Altman, conducted research and vehicle analysis efforts, which are documented in Volume I¹ of this series of reports. The United States Air Force Academy, under the direction of Dr. Thomas Yechout, collaborated in this effort by wind tunnel testing a derivative configuration; this work has been documented in an AIAA technical paper⁴.

Acknowledgements

Although the work is titled under the University of Dayton Research Institute banner, it represents the work of many individuals. In particular, the following people have made a material contribution to the completion of the modeling, analysis, fabrication, and/or the documentation of the effort:

- Altman, Aaron – UD – Wind Tunnel Testing
- Altman, Servane – UDRI – Wind Tunnel Testing
- Bryant, Elaine – AFRL – Program Management
- Fry, Tim – UDRI – CFD, DOE, Program Management
- Fry, Tracy – UDRI – DOE, Documentation
- Gillum, Chris – SES – CAD Modeling
- Houck II, Ron – IHE – Concept Inventor, Prototype Build
- Maresca, Rich – WBI – Contract and Program Management
- Morrow, Colin – Radiance Technologies – Sensor Technology
- Neely, Mike – UDRI – CAD and CFD Modeling
- Reeder, Mark – AFIT – SLA, Wind Tunnel Testing & Prototyping
- Riley, Dave – DRA – Program Management
- Simpkins, Haskell – SES
- Staiger, John – AFRL - CFD
- Tyler, Charlie – AFRL – CFD
- Walker, Michael – AFIT – Wind Tunnel Testing & Prototyping
- Yoder, James – SES – Prototype Fabrication
- Zeune, Cale – AFRL – Program Management

Executive Summary

This report covers the collaborative activities conducted under the leadership of the University of Dayton Research Institute on the Unique Stealth Unmanned Aerial Vehicle Houck Aircraft Design Program. This effort (and subsequently, the report) is organized in five phases:

Phase I: Aerodynamic evaluation of 6-inch model

Phase II: Aerodynamic evaluation of 24-inch model

Phase III: Design exploration for the Preferred System Concept

Phase IV: Design of Preferred System Concept

Phase V: Fabrication of flying prototype aircraft

Phase I focused on the evaluation of a six-inch wingspan model. The objective of the work was to “assess the aerodynamic efficiency of the Houck airfoil concept with respect to performance measures relevant to an Air Force developed generic mission profile.” The AFRL established three quantitative aerodynamic measures of merit in Phase I of the program. Work concentrated on evaluating the 6-inch joined-wing configuration developed by Iron Hawk Enterprises against those target metrics; both experimental research and Computational Fluid Dynamics analyses were performed. Of the three quantitative measures of merit in Phase I of the program the zero-lift drag coefficient criteria and Oswald efficiency metrics were effectively met, while the lift curve slope criteria was not met. Analysis and research showed, in hindsight, that the lift curve slope criteria as originally established may have been unrealistic.

Phase II focused on the detailed performance evaluation of a twenty-four-inch wingspan model of a joined-wing configuration developed by Iron Hawk Enterprises. Because the Phase I effort showed only partial success in meeting the quantitative measures of merit, the Phase II work utilized a larger twenty-four-inch wingspan model with airfoils (as opposed to the six-inch wingspan model that utilized flat plate wing sections). As in Phase I, both experimental research and Computational Fluid Dynamics (CFD) analyses were performed. Analysis of the results showed that the experimental and CFD methods provide similar outputs in the expected operational range. Lift to drag ratios of nearly 8.0 were obtained in testing and corroborated by CFD.

Phases III and IV focused on continued aerodynamic controls research, design iteration to determine a Preferred System Concept (PSC) and a mission profile investigation. Specifically, Phase III efforts concentrated on understanding the flow physics of the Houck UAV configuration, while Phase IV efforts concentrated on applying those physics to create a vehicle useful to a feasible United States Air Force (USAF) mission. Based on an iterative process including mission analysis, aerodynamic analysis, and structural analysis a PSC has been determined. The 9 pound gross weight aircraft has been sized to accomplish several different reconnaissance missions carrying a 4 pound payload. It is estimated to have an endurance of 3 hours and a length and wingspan of around 80 inches. The aircraft has been designed to be stable in all three axes to offer good flying qualities. This design became the basis for future prototype and flight testing efforts.

Phase V focused on the production of a 60% scale radio-controlled prototype aircraft. The primary deliverable, an air-worthy prototype was delivered to the Air Force Research Laboratory on September 5, 2007. Documentation is provided for the fabrication of the prototype, aircraft components, and recommendations from this effort. Due to logistical difficulties the aircraft was not able to be tested as originally envisioned.

Overall, this configuration of aircraft, as modeled, was found not to have aerodynamic characteristics markedly better than existing small unmanned aircraft. It may have potential to show benefit over existing aircraft in other areas though, including structural weight required as a result of the joined tips, size required to package the aircraft for man-portability due to its limited span, and range of c.g. travel owing to large longitudinal wing spacing for trim. To understand potential benefits in these areas, these characteristics would need to be assessed in further studies using different, higher fidelity methods.

1 Phase I: Aerodynamic Evaluation of the 6-inch Model

1.1 Introduction

This section details the effort during Phase I of the Unique Stealth UAV Houck Aircraft Design Program. The purpose of this phase of the program was to employ theoretical and experimental techniques to better understand the aerodynamics of the Houck airfoil concept via the six-inch wingspan prototype. This section discusses the configuration, CAD modeling, aerodynamic modeling, results and conclusions of Phase I.

Figure 1 shows a sketch of the 6-inch Houck model taken from the United States Patent no. 7,100,867 covering the design.

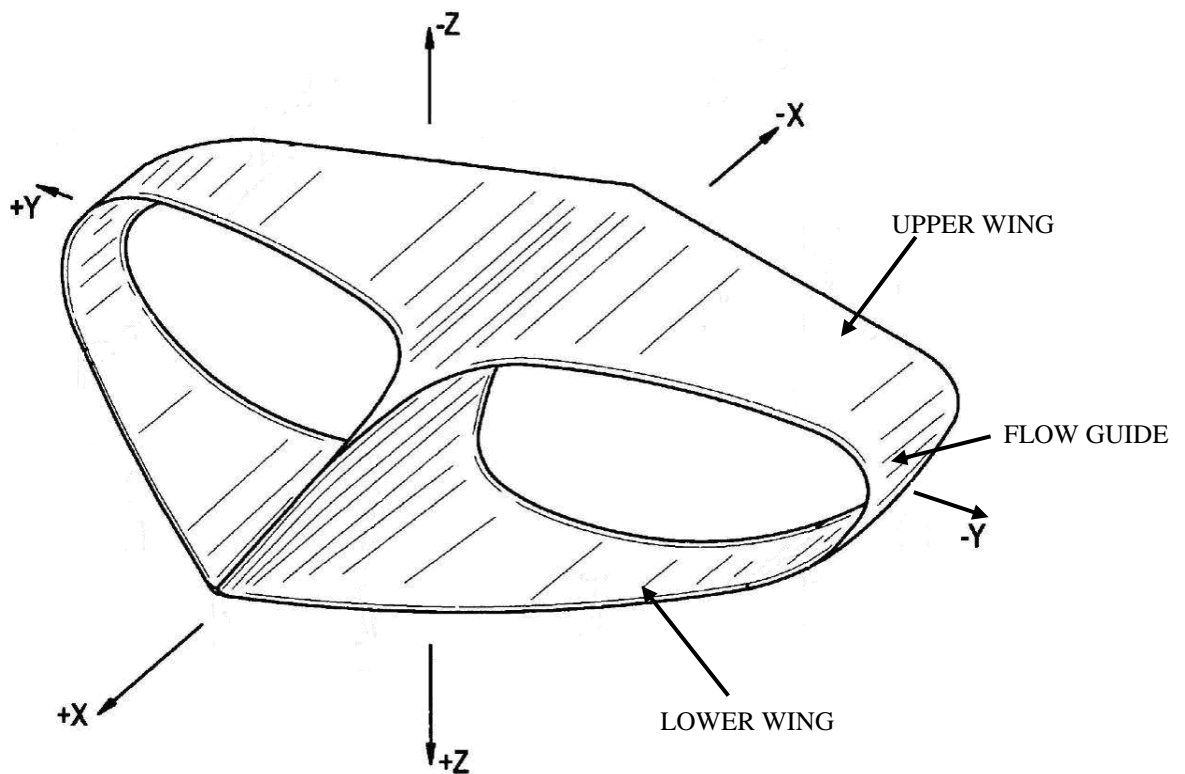


Figure 1: Sketch of Houck Airfoil Concept

A potential application for the Houck Airfoil is as a small-UAV used for either surveillance or reconnaissance. In these applications the mission profile requires a vehicle with high loiter time. The performance metrics for Phase I of this work are based on such a mission. Specifically, evaluation of the Houck concept design is based on meeting or exceeding threshold values of several key performance parameters. These parameters measure the effectiveness and efficiency of the Houck Airfoil's lift generating and reduced drag performance. These performance parameters are: wing lift curve slope ($C_{L\alpha}$), value of drag at zero-lift (C_{D0}), and Oswald's Efficiency Factor (e). The Air Vehicles Directorate established the threshold values for these three performance parameters at:

1. Drag Coefficient at Zero-Lift: $C_{D0} \leq 0.045$
2. Aircraft Lift Curve Slope: $C_{L\alpha} \geq 0.09 / \text{deg}$
3. Oswald's Efficiency Factor: $e \geq 0.8$

Principal Phase I participants of the collaborative team were IHE (model development), UDRI (wind tunnel testing and preliminary CFD computations), and AFRL/RBAC (CFD comparative analysis). Additionally, AFIT assisted the team effort by laser scanning the IHE model for CFD analysis.

Deliverables for Phase I were:

1. Engineering 3-view drawings of the selected model configuration
2. Outer mould line geometry
3. Estimates of mass properties (actually delivered in Phase II, after mission defined)
4. Wind tunnel data on lift coefficient, drag coefficient and pitching moment coefficient as functions of AOA
5. Data reduction substantiating that $C_{L\alpha}$, C_{D0} , and e criteria have been met
6. CFD data
7. Written documentation

1.2 Configuration Data

The Houck Airfoil consists of an upper and lower set of wings joined at the two wingtips by curved flow guides. These flow guides are claimed to reduce wingtip vortices associated with lift production of finite span aircraft wings. This reduction is accomplished by the gradual decrease of camber from the top of the lower wing as it transitions to the bottom of the upper wing where the camber is zero. Alternatively, the camber of the top of the upper wing gradually decreases as it transitions to the bottom of the lower wing where the camber is zero.

The Houck patent also claims that this camber transition maintains the camber needed on the top of the upper and lower wings necessary to sustain flight while employing a corresponding and equal camber decrease to a matching camber increase on the opposite side of the flow guides throughout entire the length of the curved connector. The two sets of wings are generally offset in the vertical plane and not intended to be directly over each other.

The Houck Airfoil design, as claimed, allows other classical wing parameters, such as chord, to vary along the length of either upper or lower wings sets. In addition, the relative angle can vary between the two wing sets. The frontal view of the wing set is generally elliptical in shape but the vertical separation as well as the span of the two joined wings on each side can vary. The Houck patent, as written, is general enough to allow for various combinations of these parameters.

The evaluation model used in Phase I of the R&D effort is similar in shape to that shown in Mr. Houck's Design Patent Number 1. The model is six inches in length and wingspan; Figure 2 is a picture of the evaluated model.



Figure 2: Evaluation Model of Houck Airfoil

The model was hand-shaped out of high density Styrofoam. It was then covered with a thin coat of epoxy resin to increase strength and impact resistance. Finally, the model was sanded smooth to reduce surface waviness and skin roughness effects. The Air Force Institute of Technology (AFIT) performed a laser scan of the model to generate a stereo-lithography file that would be used as the basis for a CAD model and subsequent CFD analyses. The model was painted flat white to aid the laser scanning process. This flat white paint was also necessary to facilitate wind tunnel evaluation. The model was subsequently modified to allow installation of the force balance for wind tunnel testing. Figure 3 is a picture of the laser can model.



Figure 3: Picture of Laser Scan Geometry

1.3 CAD Modeling

UDRI was tasked with modeling the 6-inch Houck airfoil in the CFD program FLUENT to determine its aerodynamic characteristics. To perform the CFD meshing and analysis, an accurate 3D solid model of the airfoil was needed. However, the CAD geometry provided (triangulated mesh derived from a laser-scan) was very coarse, and although UDRI was able to import the .STL mesh into the Rhino CAD program, the coarseness of the airfoil body made it unsuitable for meshing in GAMBIT.

In the CAD modeling phase of the project, the airfoil geometry was rebuilt in the 3D CAD program Unigraphics NX3, the NX3 body was exported to GAMBIT, and GAMBIT was used to generate the CFD mesh. The GAMBIT mesh was then exported to FLUENT, in which the boundary conditions and other parameters were assigned, and the CFD analysis was performed.

Figure 4 shows the original triangulated mesh from the laser-scanned .STL file. Figure 5a shows section curves created by cutting the body at equally spaced transverse intervals. Figure 5b is a detailed view comparing the original and smoothed cross-section curves. The magenta is the original curve from the laser-scan geometry. The green is the smoothed curve. Note the roughness of the original curves. This roughness made the model unsuitable for CFD modeling. Additional smoothing of the CAD model was required.

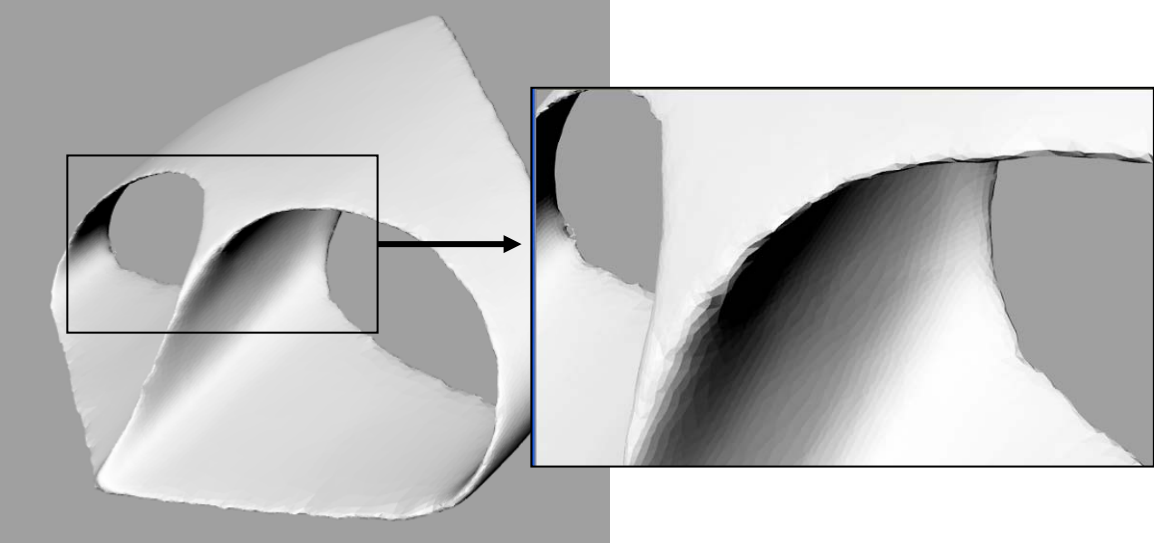
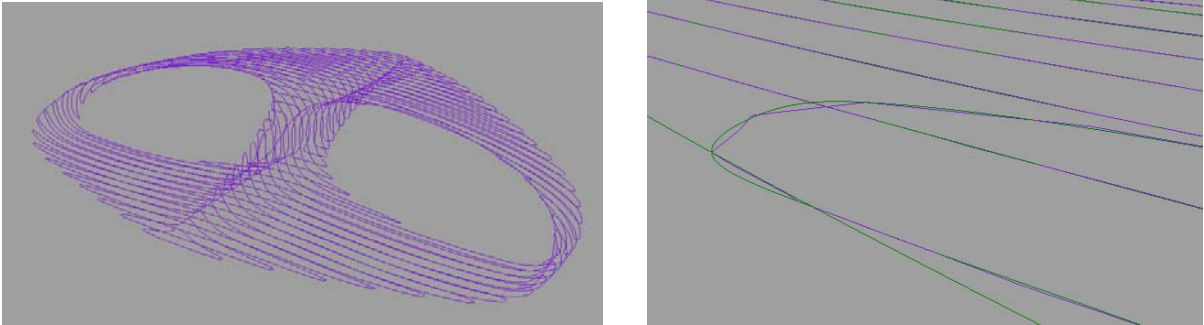


Figure 4: Image from Original .STL Mesh of Airfoil



(a) (b)
Figure 5: Chordwise Section Curves (a) and Section Detail (b)

Two attempts were made at generating high quality airfoil surfaces in the CAD program Rhino. In both efforts, the mid-body or transition region between the upper and lower wings presented

considerable difficulties, in that the surfaces-from-lofted-curves approach could not be used. The method based on a patchwork or “quilted” array of surfaces met with mixed results, with some areas containing poor surface-to-surface tangency, and other areas containing tiny gaps between adjacent surfaces. An example of surfaces with poor tangency conditions is shown in Figure 6.

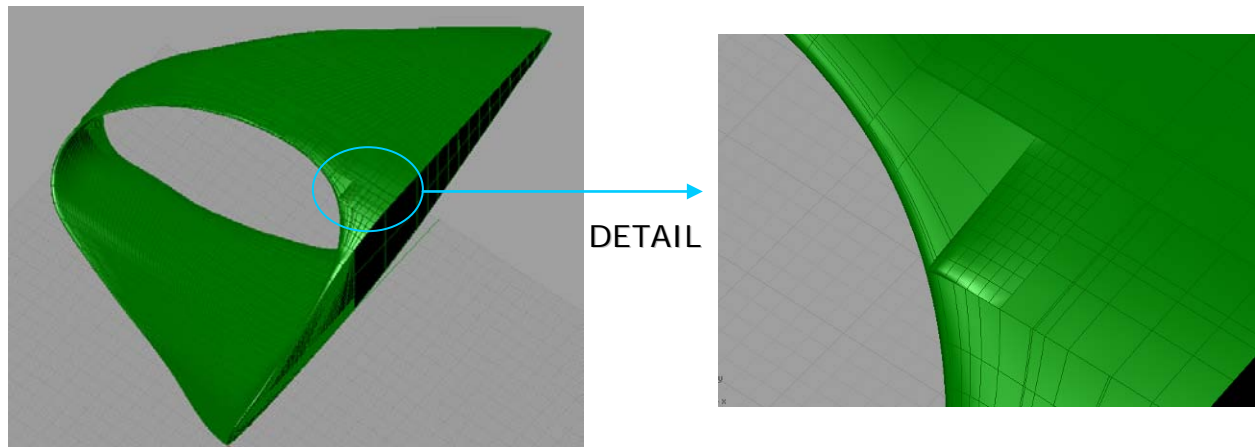


Figure 6: Surface Discontinuities: Quilted-surface Modeling Method

After falling short with the surface-based modeling method, UDRI undertook a three-dimensional, solids-based approach using the CAD program Unigraphics NX3. Unigraphics NX3 is widely used in the aerospace and automotive industries, and is regarded as one of the “high-end” CAD packages along with Pro/ENGINEER and CATIA. In Unigraphics NX3, the upper and lower wings could be modeled in much the same way as in Rhino, using lofted section curves. In Unigraphics NX3, the end-curves were capped and the bounding surfaces sewn together to form a solid body.

In the case of the airfoil transition region, or mid-body, a different approach was used. The mid-body had presented modeling difficulties because of the complex way in which curves flow through it from the upper and lower wings. The complexity of the mid-body made it difficult to use lofted-curve sections for generating airfoil surfaces.

Before starting the modeling work in Unigraphics NX3, airfoil section curves were imported from Rhino and modified such that the curves were set on constant chordwise planes at increments of 10 mm. The curves used to develop the geometry in Unigraphics NX3 are shown in Figure 7.

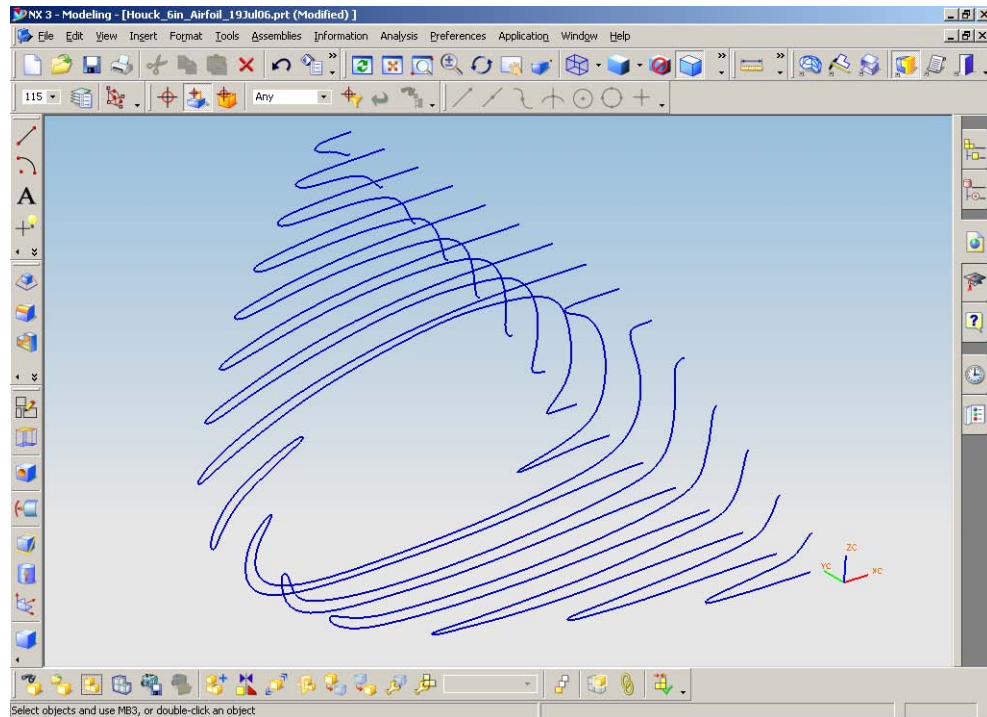
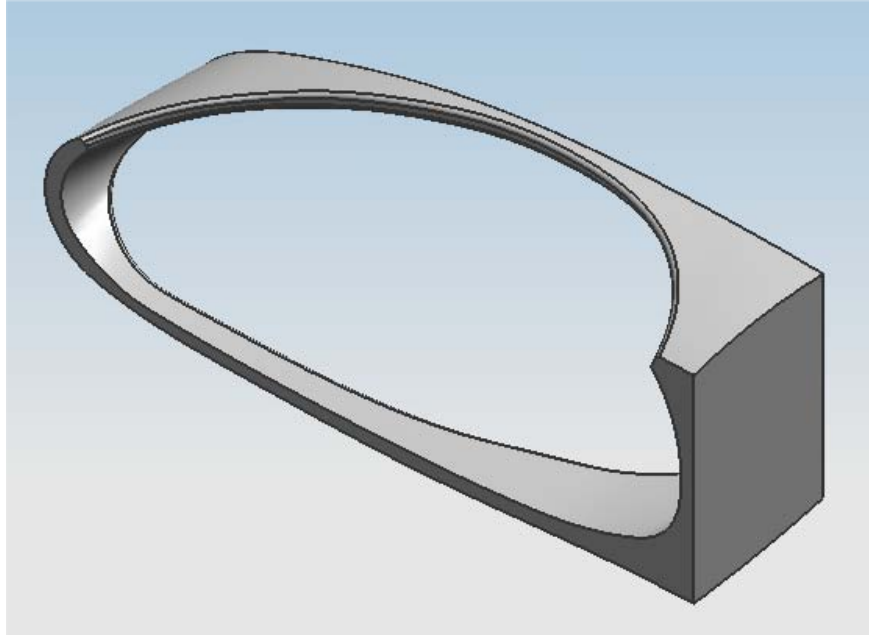
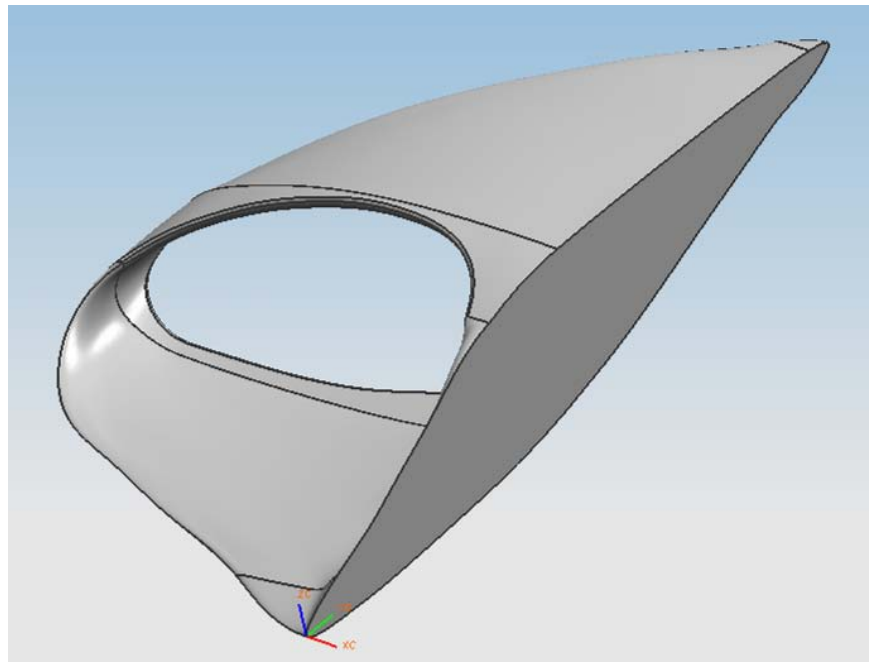


Figure 7: Chordwise Section Curves Using Unigraphics NX3

The vehicle transition region (mid-body) was built as a solid, filled body from which a smaller solid with an oval cross section was subtracted. Edge blends were added at the inlet and outlet of the mid-body to create rounded surfaces in these areas. The solid mid-body created in Unigraphics NX3 had none of the surface irregularities of the Rhino surfaces shown in Figure 6. The Unigraphics NX3 solid mid-body geometry is shown in Figure 8a. By uniting the lower wing, transition region and upper wing, a single solid body of the airfoil was created, as shown in Figure 8b.



(a) solid model of transition region



(b) solid model of half-airfoil

Figure 8: NX3 Modeling Approach for the Houck Six-inch Airfoil

In FLUENT the symmetry boundary condition was applied at the spanwise mid-plane. Therefore, only half of the aircraft needed to be modeled in NX3. This had the added benefit of reducing the grid count and computation time.

The *Rhino* 3D CAD program was used to import the .STL file, cut several cross sections, and develop smoother section curves using free-form splines through interpolated points. These curves were exported to NX3 when the surface-based modeling approach proved to be unworkable. Three-dimensional solid bodies were created in NX3 from the Rhino curves. The upper wing, transition region (mid-body) and lower wing were united in NX3 to form a single solid body. Parasolid and STEP files were exported from NX3 for use in GAMBIT.

Summary of files received and files created:

Original .STL file of scanned body: *iron-hawk-2mag-ascii.stl*

Rhino 3D file, curves, and surfaces: *Houck_with_Surfaces_30Apr06.3dm*

Unigraphics NX3 part file: *Houck_6in_Airfoil_18Jul06-4.prt*

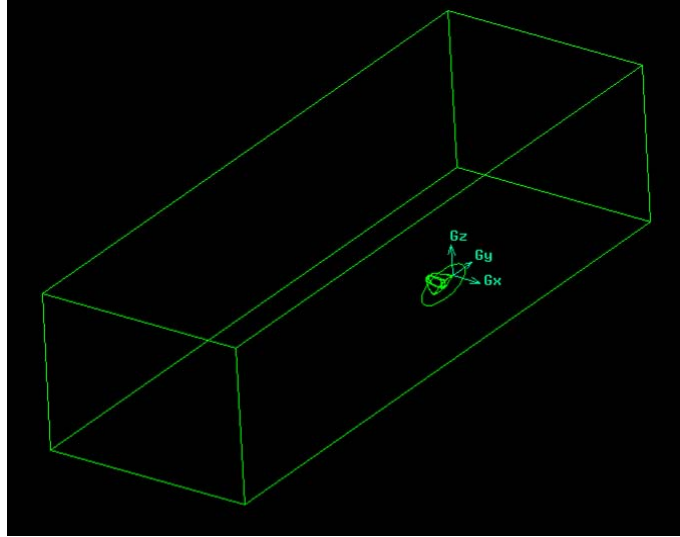
Parasolid file exported from NX3: *Houck_6in_Airfoil_18Jul06-2.x_t*

STEP file exported from NX3: *Houck_6in_Airfoil_18Jul06-4.stp*

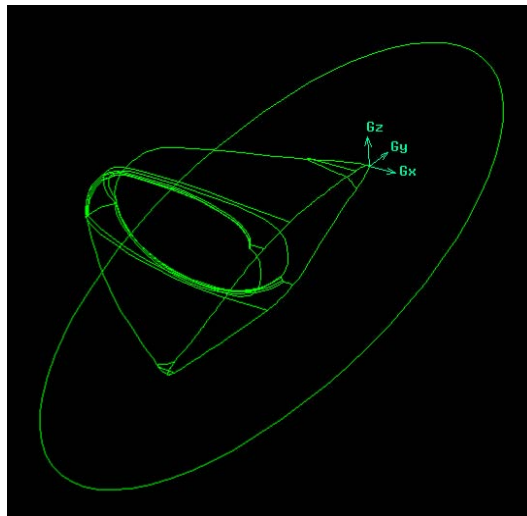
Due to the roughness of the original CAD geometry, UDRI made assumptions concerning the placement of points and curves on the airfoil. No tolerances were specified by the customer regarding the original .STL file.

The airfoil geometry was exported from NX3 and imported into GAMBIT. Figure 9 shows the airfoil geometry in GAMBIT. There were no problems encountered when meshing this geometry, as indicated by the lack of small surfaces slivers and surface-to-surface gaps in the GAMBIT geometry.

The airfoil solid was subtracted from a larger solid block representing the flow domain. The Boolean subtraction of the airfoil from the block was performed successfully, and resulted in so-called “real” geometry in GAMBIT.



(a) full flow domain



(b) airfoil detail

Figure 9: GAMBIT Views of Airfoil Geometry

Another deliverable, a three-view drawing of the 6-inch airfoil, is shown in Figure 10.

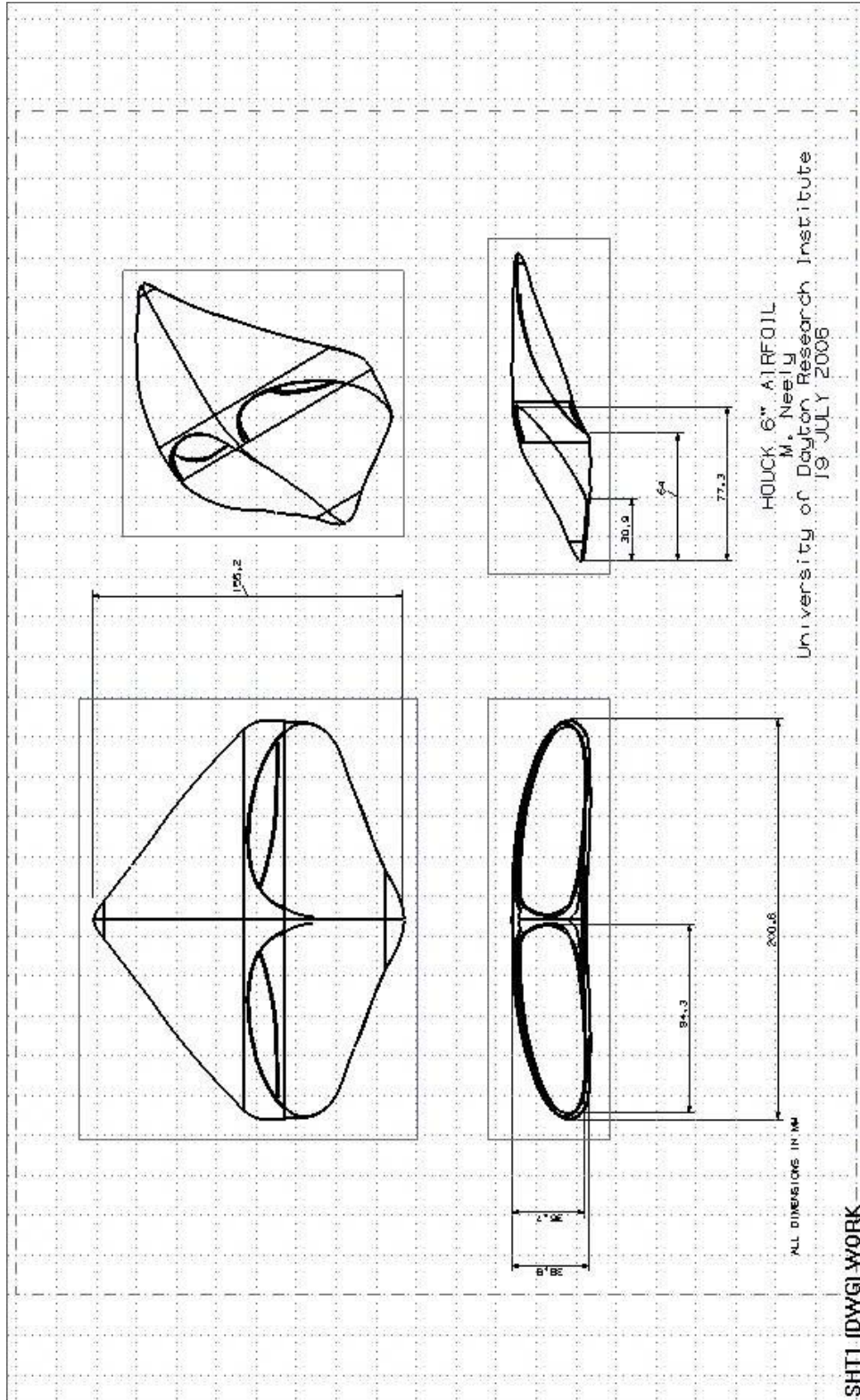


Figure 10: Three-View Drawing of 6" Houck Configuration

The airfoil geometry created in Rhino was not suitable for use in CFD meshing and analysis. The solids-based modeling approach using NX3 resulted in more-accurate CAD geometry that could be exported in a number of commonly used neutral-file formats such as IGES, STEP, and Parasolid. The NX3 program includes many advanced features such as sketcher and parametric solid-modeling operations, allowing model changes to be made more quickly and easily. It is recommended that future airfoil designs be modeled in a solids-based CAD system, such as NX3 or NX4 (a later release of Unigraphics). This will be an even more important consideration as we seek to develop a parametric approach to airfoil design and analysis.

1.4 Aerodynamic Analysis

Three separate aerodynamics analysis effort occurred during Phase I. These analyses include the Wind Tunnel Analysis, the AVUS CFD Analysis, and the FLUENT CFD Analysis.

1.4.1 Wind Tunnel Analysis

The Houck configuration does not neatly conform to any existing theoretical description. It can be considered somewhere between a biplane and a joined wing configuration. This ambiguity leads to difficult questions such as what planform area is the most representative reference area to use when calculating the aerodynamics coefficients. Discussion into how that selection of reference planform area affects the representation of the measured lift and drag characteristics of the configuration did not result in a consensus method for which to apply in the reduction of the experimental and computational data. After much discussion, the decision to evaluate the Houck configuration based on a variety of theoretical models was taken. Table 1 summarizes the differences in the models considered. These included the finite monoplane, the orthogonal biplane, and the equivalent monoplane methods.

The definition of aspect ratio and downwash angle or induced angle of attack for the aft wing is provided for each method. For a more detailed discussion into the origins of these relations, please refer to Stinton⁵. In these equations, S is always reference planform area, b is the wing

span, AR is aspect ratio, e is the span efficiency factor, σ can be considered a constant and G is the gap between the upper and lower wings.

Table 1: Theoretical/Empirical Models Used in Analysis

	AR	e or α_i
Finite Monoplane	$\frac{b^2}{S}$	$\frac{C_L}{\pi A R e}$
Orthogonal Biplane	$\frac{2b^2}{S}$	$\frac{C_L(1+\sigma)}{\pi A R e}$ $0.4 \leq \sigma \leq 0.6$
Equivalent Monoplane	$\frac{(kb)^2}{S}$	$\frac{C_L}{\pi e} \frac{S}{(kb)^2}$ $k^2 = 1.8 \left(\frac{G}{b} + 1 \right)$

Correspondingly, there are several appropriate methods for approximating lift curve slope.

Slender wing theory may be appropriate due to the low aspect ratio of the model using one of the methods and it states

Equation 1 – Lift Curve Slope from Slender Wing Theory

$$a = \frac{1}{2} \pi A R e$$

And Prandtl's lifting line theorem states:

Equation 2 - Lift Curve Slope from Prandtl Lifting Line Theory

$$a = \frac{a_{\infty}}{1 + \left(\frac{a_{\infty}}{\pi A Re} \right)}$$

Where a_{∞} is the ideal two-dimensional lift curve slope. All of these methods will be evaluated in an attempt to determine the best theoretical match for the behavior of the Houck configuration tested. All of the resulting experimental data will be reduced and compared using these methods.

Both force measurement and planar laser flow visualization were performed to better understand the Houck configuration. These experiments were carried out in the University of Dayton/University of Dayton Research Institute Low Speed Wind Tunnel (LSWT) seen in Figure 11. The DART CORPORATION constructed the tunnel in 1992.



Figure 11: University of Dayton Low Speed Wind Tunnel

The LSWT is an Eiffel type with an 11:1 contraction ratio. The fan was designed and constructed by Hartzell and is driven by a 60 HP motor. The test section measures 30" X 30" X 90" (~0.75 X 0.75 X 2.3 m), and is easily exchanged with other test sections used for

demonstration and educational purposes to preserve the quality of the research test section. The LSWT has five anti-turbulence screens at the tunnel inlet.

The highest flow quality operable speed range of the LSWT is from 6.7 m/s (20 ft/s) to 36.7 m/s (120 ft/s). The tunnel has a turbulence intensity in the free stream direction of less than 0.1% throughout the test section (measured by hot wire anemometer), and less than 0.05% throughout the center portion of the test section utilized for testing the Houck configuration.

The force balance used to determine the forces on the Houck configuration was specifically designed for force measurement on Micro UAVs. It is a 6-component platform design with a maximum load of ± 4 lbs. The force balance is based on a Nano Sensor 43 for which an in-house calibration was performed and matrix subsequently created. The balance accuracy was calibrated to be on the order of fractions of a gram.

Data acquisition was performed on a Pentium IV PC running LabVIEW 8.0 and software written in-house driving a PCI 6281 performing simultaneous sampling at 1000 Hz passed through an SCXI Chassis and SCXI 1140 hardware filter. 1000 samples were recorded in each data sweep, and these values were acquired 4 times for any given angle of attack and tunnel speed to provide a total of 4000 samples per data point represented.

The flow visualization was performed using a Spectra-Physics Nd:YAG laser at 300 mJ per pulse. A Megaplex 1.0 model 1 Megapixel camera in combination with a PIXCI D2X frame grabber captured the illuminated flow field. Smoke was added to the flow for visualization of the planar light sheet using a Le Maitre disco fog machine and Roscoe smoke fluid.

Once the model/balance interface was manufactured, the model was installed in the tunnel with a reference zero angle of attack that was maintained for the duration of the Houck testing (see Figure 12). Selection of this experimental reference zero was a non-trivial matter given that there was no apparent flat portion from which to reference. The reference selected for the experiments corresponded to the upper surface of the upper lifting surface at the middle of the

fuselage. This reference is in contrast to the reference selected for the computational results that were based on the upper surface of the upper lifting surface at the back of the fuselage. This difference in reference zero (or “waterline”) was subsequently responsible for a shift in zero degree angle of attack lift of roughly -3.8 degrees in the experimental results.

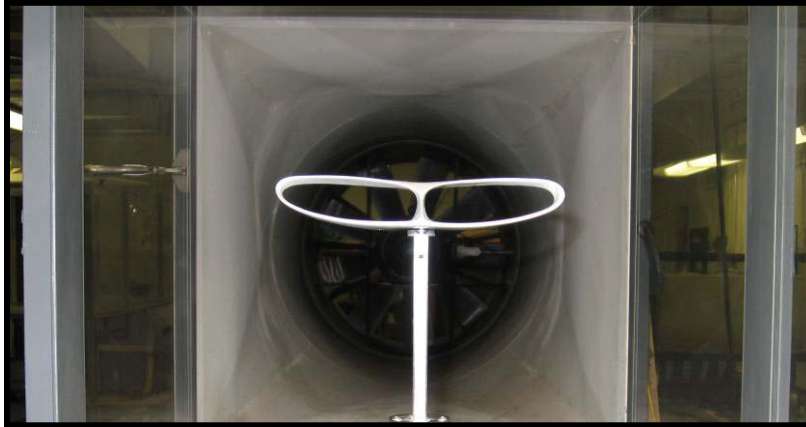


Figure 12: Houck Model Mounted in the UD LSWT

Aerodynamic tests were run on the balance/support structure alone and with flat plate wings to account for the drag of the balance and any potential upwash effects of the balance support. Unfortunately, it was not possible to mount the Houck model upside down on the balance support in its present configuration. Thus, the “mirror support” system for model support correction was not employed; however, the upwash effects on the flat plate wing planform were nominal. Tunnel temperature and atmospheric pressure were measured numerous times during execution of the experiments and were used in the correction of calculated velocity to real tunnel velocity.

The experiments were executed in several different manners beginning with alpha (angle of attack) sweeps, then Q (velocity) sweeps, and finally randomized testing. Solid and wake blockage calculations were performed and these effects were also found to be insignificant due to the small size of the model relative to the test section dimensions.

In general, the matrix of parameters tested was:

Angle of attack: $-14^\circ < \alpha < 24^\circ$
Velocity: 15, 25, 35, 45, 55, 85 MPH
Model: 1* and 2* Scale

The lift curve can be seen in Figure 13 for the 6-inch span model. As previously mentioned, the zero lift angle of attack was offset by roughly 3.8 degrees due to a poor reference zero on the model. Among the notable points in this figure are significantly lower C_{Lmax} for the lowest Reynolds number/speed tested. An apparent slight decrease in C_{Lmax} for the two highest Reynolds number/speeds tested can be observed. The Houck configuration experienced a gradual, benign stall. And there is a decrease in lift curve slope above roughly minus 3 degrees.

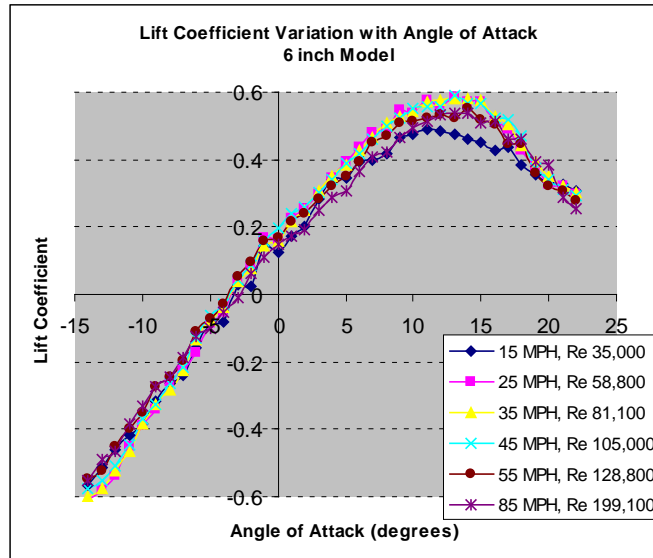


Figure 13: Lift Curves for the 6-inch Houck Model

The variation in drag with angle of attack can be seen in Figure 14. Clearly, the two lowest Reynolds number/speed cases experienced much higher drag than the remaining higher Reynolds number cases. Based on experience in low Reynolds number aerodynamics this increase in drag is not entirely unexpected.

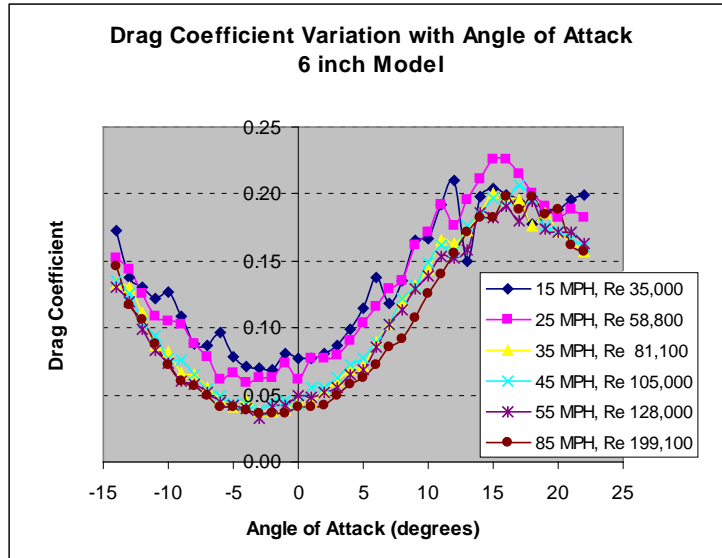


Figure 14: Drag Coefficient Variation with Angle of Attack

There is also a very slight broadening of the drag bucket at the highest Reynolds number/speed case. It is not entirely clear why the drag begins to decrease again above 16 degrees. The drag polar for the Houck configuration 6-inch model can be seen in Figure 15.

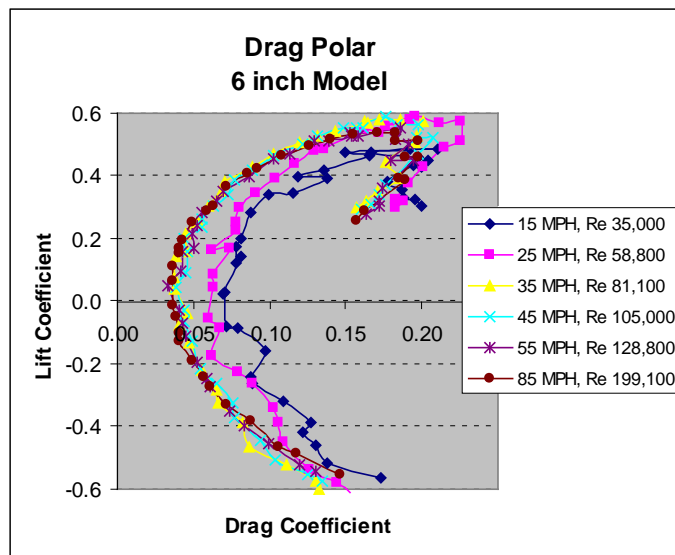


Figure 15: Drag Polar for the Houck Configuration

The two lowest Reynolds number/speed cases have markedly different behavior than the remainder of the Reynolds number/speed cases. The results at these lower Reynolds numbers demonstrate significantly greater scatter. Potential explanations are the presence of flow separation or the shedding of vortices into the flow. Another potential explanation is that the voltage signal for the absolute drag forces is being clipped/filtered or on the lowest side of the sensitivity range of the sensor. Finally, there is the possibility that these Reynolds number cases are more sensitive to noise in the transition to turbulence.

The lift to drag ratio can be seen as a function of angle of attack in Figure 16. Once again, the two lowest Reynolds numbers/speeds tested greatly underperformed the other cases tested. Apart from the behavior at the two lower speeds, the L/D curve looks relatively conventional. Most notable is the reasonably flat peak in maximum L/D ratio. This indicates a reduced sensitivity to off design operation rather common in micro UAV scale vehicles.

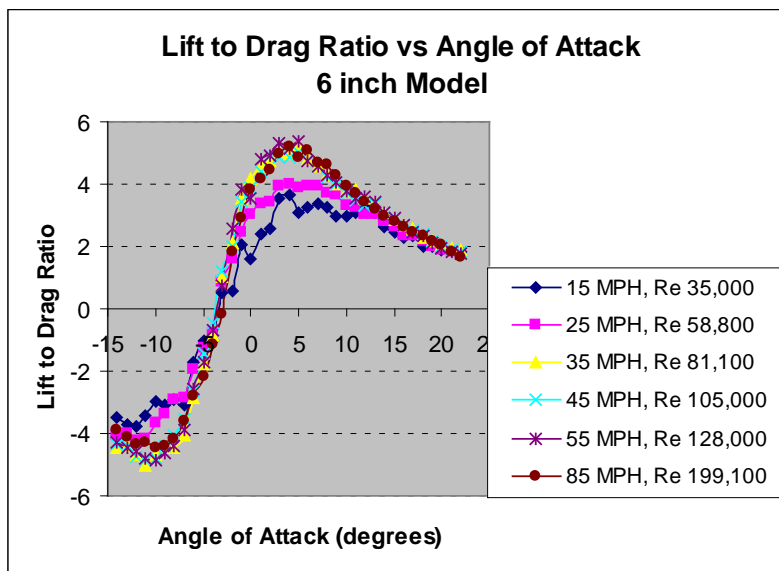


Figure 16: Lift to Drag Ratio for the 6-inch Model Houck Configuration

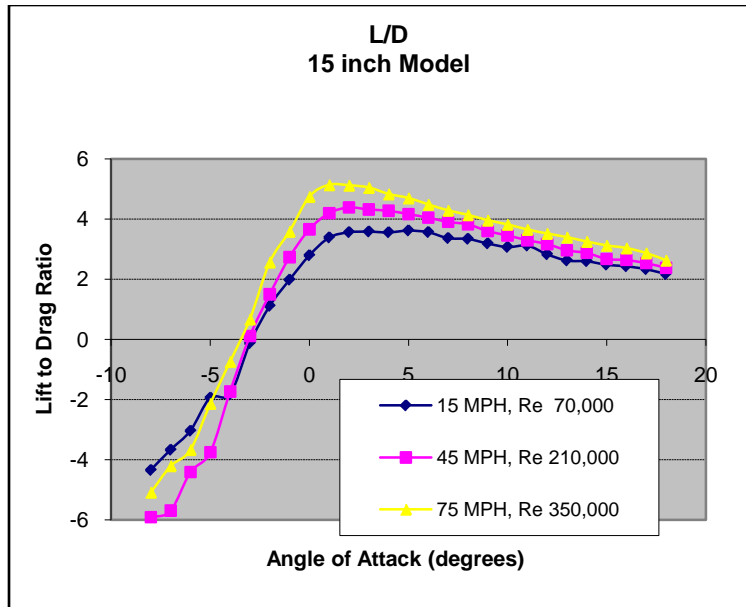


Figure 17: Lift to Drag Ratio for the 15-inch Model Houck Configuration

The lift to drag ratio data can be seen for the 15-inch model in Figure 17. This figure indicates that lift to drag ratio improves with increasing Reynolds number/speed. In addition, the shapes of the lift to drag curves are even less sensitive to off-design conditions. The performance of the Houck configuration is actually quite poor, however, for a model in the 15-inch scale range. A compilation of minimum C_{D0} and L/D_{max} is shown in Table 2 for the 6-inch model. The lowest values of both C_{D0} and L/D_{max} are found at the highest Reynolds number tested.

Table 2: Minimum Base Drag and Maximum Lift to Drag Ratio Values

	C _{do}	L/D _{max}		Re
15 mph	0.06923	3.644	22 ft/s	41950
25 mph	0.05960	4.017	37 ft/s	70552
35 mph	0.03732	5.256	51 ft/s	97247
45 mph	0.03853	5.010	66 ft/s	125849
55 mph	0.03311	5.347	81 ft/s	154451

Initially, several theoretical models were used to obtain a lift curve slope and subsequently, an equivalent span efficiency factor. The first iteration (for the 6-inch model) is shown in Table 3. As explained previously, several theoretical models were used since the Houck configuration was non-trivial to classify within the existing models. Table 3 was created in order to identify the most appropriate method to the Houck configuration.

Table 3: Lift Curve Slope and Span Efficiency Factor Results: 6-inch Model

		Orthogonal Biplane		Equivalent Monoplane	
	a	Slender	Lifting Line	Slender	Lifting Line
15 MPH	0.0385	0.350	0.269	0.331	0.255
25 MPH	0.0413	0.375	0.301	0.355	0.285
35 MPH	0.0426	0.387	0.316	0.366	0.300
45 MPH	0.0401	0.364	0.287	0.345	0.272
55 MPH	0.0373	0.339	0.257	0.321	0.243
Orthogonal Biplane	Slender	1.001			
	Lifting Line		0.999		
Equivalent Monoplane	Slender			1.000	
	Lifting Line				0.999

As shown in the table, the lift curve slope, “a,” was quite poor when compared to the existing multiple lifting surface methods, with the maximum value of 0.0426 for the Houck configuration

and a minimum value of 0.0732 from Lifting Line theory using the Orthogonal Biplane assumption. The span efficiency factors also did not provide very high values (max. 0.387). Although lower values would be expected for span efficiency factor for a model in the 6-inch range at the Reynolds numbers/speeds tested, this efficiency was still rather poor.

As a direct result of this poor performance in lift curve slope and span efficiency, it was determined that the theoretical methods were limited in their description of the Houck model. It was also thought that the Houck configuration was primarily lifting with just one of its lifting surfaces. The experimentally obtained values were subsequently re-evaluated based on the assumption of a low aspect ratio monoplane.

The results of assuming a single monoplane are shown in Table 4. The theoretically predicted maximum lift curve slope is now 0.0551 and the maximum value obtained by the Houck configuration is 0.0426. This is still less than 80% of the theoretical value obtainable for lift curve slope. Span efficiency also experienced a significant gain by treating the Houck configuration as a monoplane, with a maximum span efficiency value of 0.773. This span efficiency is actually quite good for the 6-inch scale vehicle at the Reynolds numbers/speeds tested.

Table 4: Lift Curve Slope and Span Efficiency Factor: Single Monoplane Assumption

			Single Monoplane	
		a	Slender	Lifting Line
	15 MPH	0.0385	0.699	0.538
	25 MPH	0.0413	0.749	0.601
	35 MPH	0.0426	0.773	0.632
	45 MPH	0.0401	0.728	0.574
	55 MPH	0.0373	0.677	0.513
Single Monoplane	Slender	0.0551	1.000	
	Lifting Line	0.0550		1.001

The laser flow visualization results were used to gain a better understanding into the behavior of the wake as a function of Reynolds number, and to identify any significant regions of flow separation and vorticity. All of the experiments in this section were performed on the 6-inch model. The single factor that was common to all of the flow visualization images was the highly three-dimensional nature of the wake. There is a great deal of shear in the flow in the wake and what appears to be significant shed vorticity in the wake as well.

Visualization of two angles of attack at 15 MPH are shown in Figure 18. There is a distinct difference in the scale/magnitude of the disturbances in the wake, which increase in size with increasing angle of attack. At 6-degrees angle of attack, the model is not yet stalled, and at 20-degrees, the model is stalled.

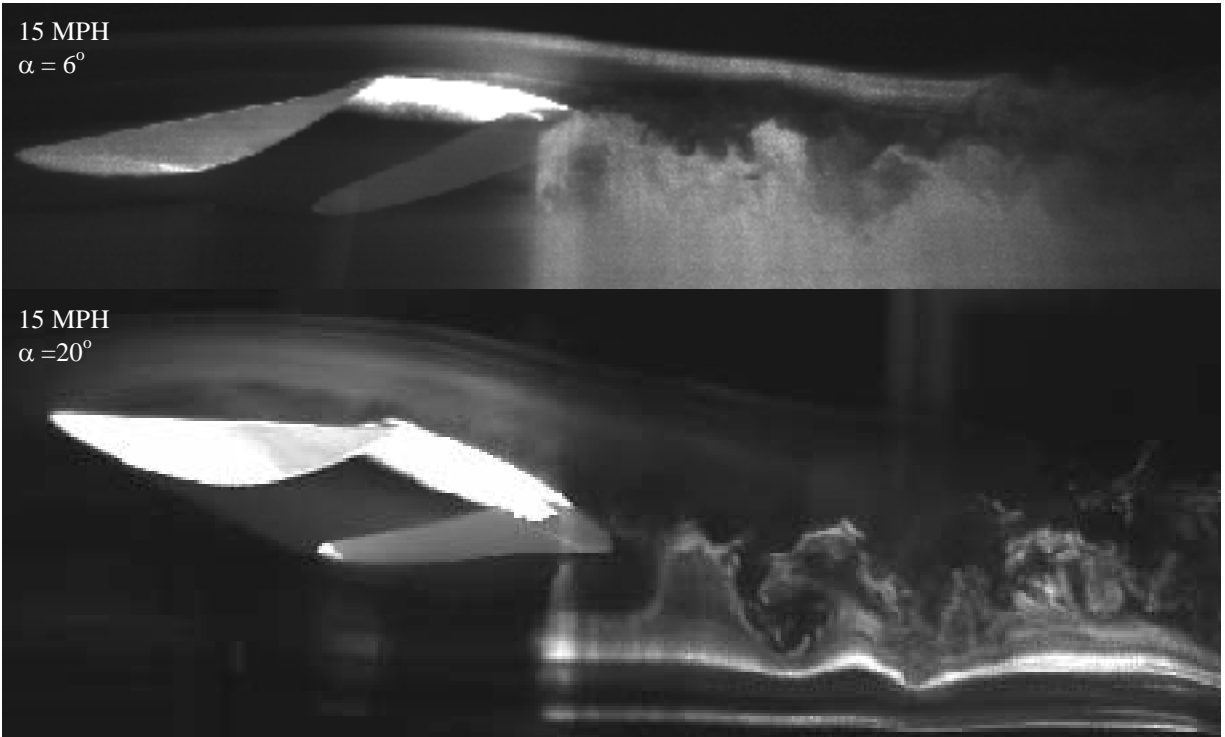


Figure 18: Wake at 15 MPH for AOA = 6, 20 degrees

Figure 19 shows the same two angles of attack, but at 35 MPH (Re 97,247) instead of 15 MPH (Re 41,950). At 6-degrees there appears to be some periodicity in the shedding in the wake, though this shedding could potentially be an artifact of influence from the lower lifting surface. This periodicity is not observed for the 20-degree angle of attack case. In comparing the 15 and 35 MPH cases, the wake for the 35 MPH, 20-degree angle of attack case is much less clearly defined and is more uniformly highly unsteady in the shear layer at the trailing edge.

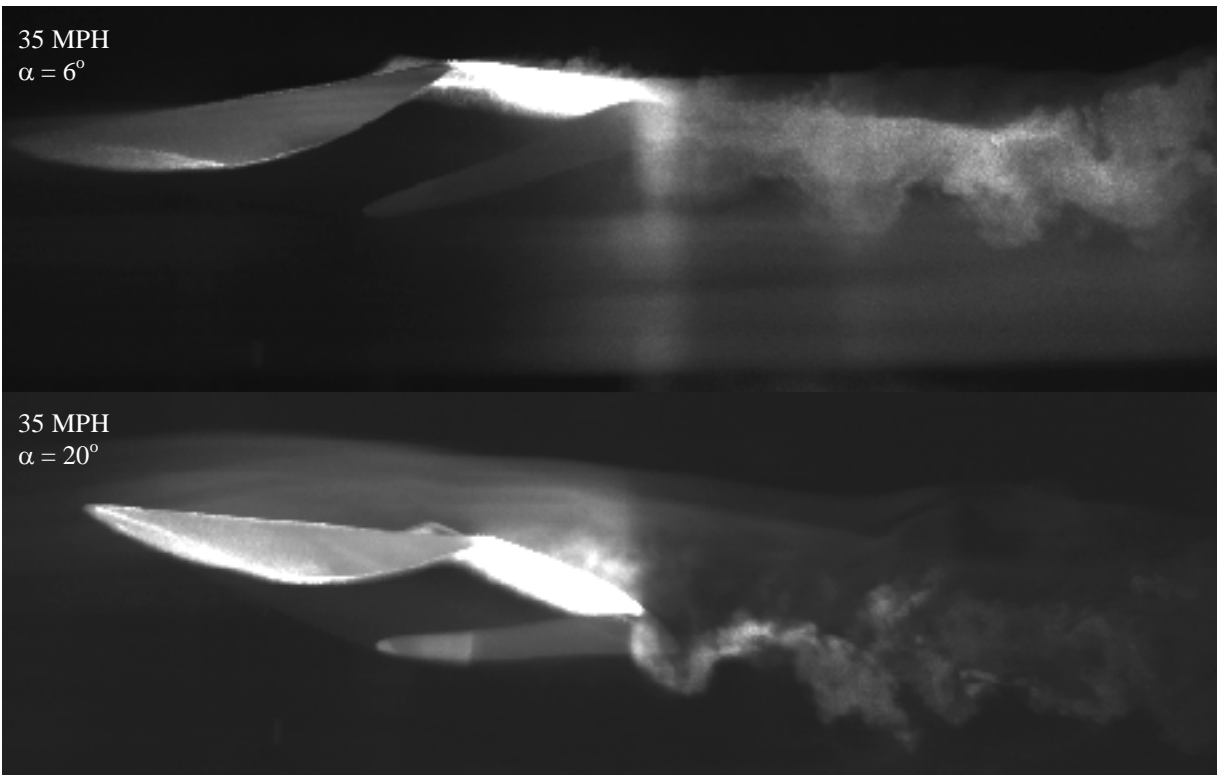


Figure 19: Wake at 35 MPH for AOA = 6, 20 degrees

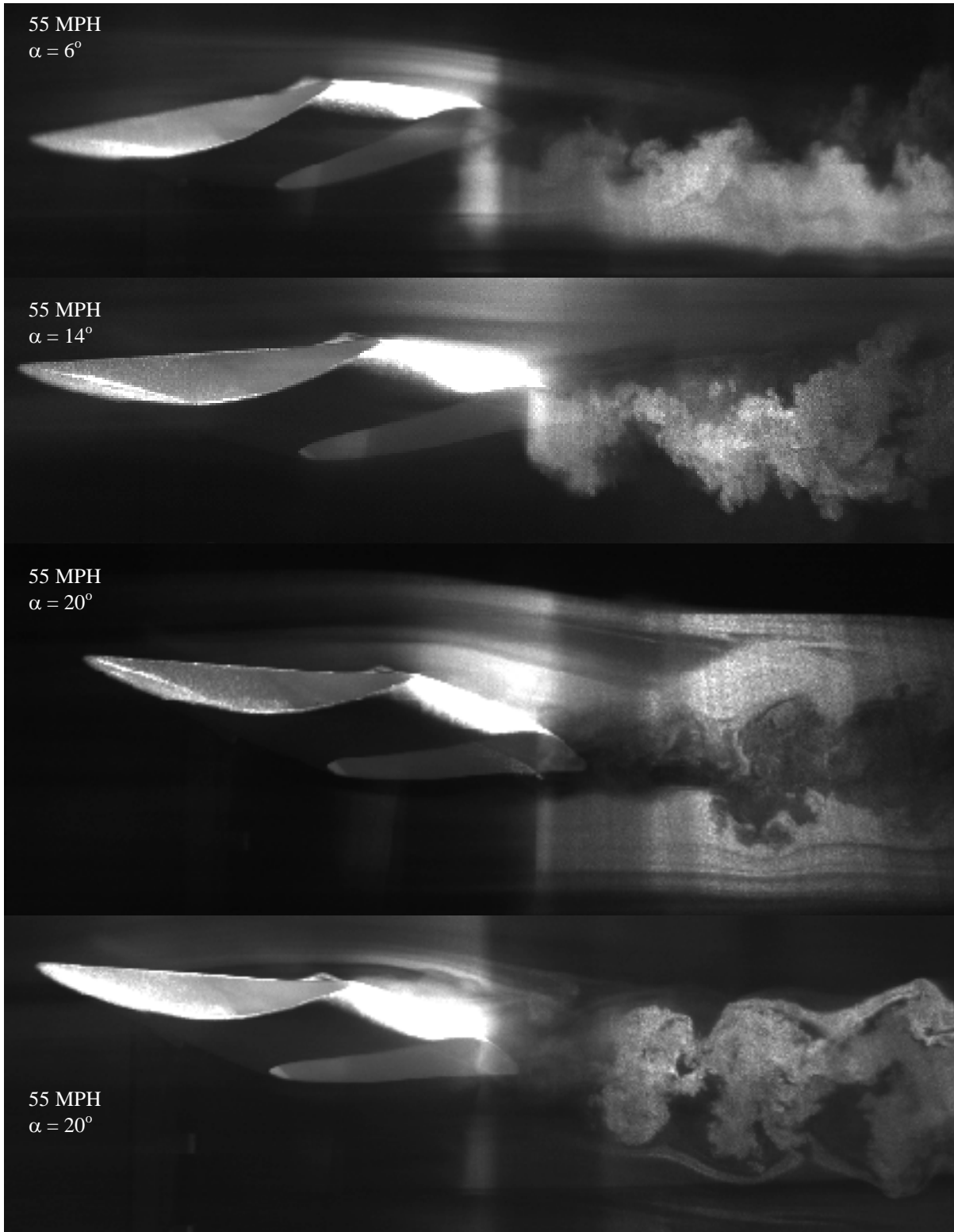


Figure 20: Wake at 55 MPH for AOA = 6, 14, 20, 20 degrees

A wider range of angles of attack are shown in Figure 20. In addition, two different images are shown at the same angle of attack, one with the smoke entrained in the vortex cores and one with smoke entrained from the periphery of the wake providing different perspectives on what should be a similar wake.

The wake at 6-degree angle of attack resembles the wakes observed at other speeds while still at the same angle of attack. It is not clearly defined and highly unsteady, with no discernible periodicity. The wakes at 14- and 20-degree angle of attack are more clearly defined, show some periodicity, and move upwards slightly. This upward movement of the wake is suspected to result from the effects of separation on the upper surface causing a greater pressure deficit behind the model.

Close up views of separation at the leading edge of the upper wing at 20-degrees angle of attack are shown in Figure 21 for two different speeds. For the 35 MPH case there appears to be some periodicity in the shedding of the leading edge vortex.

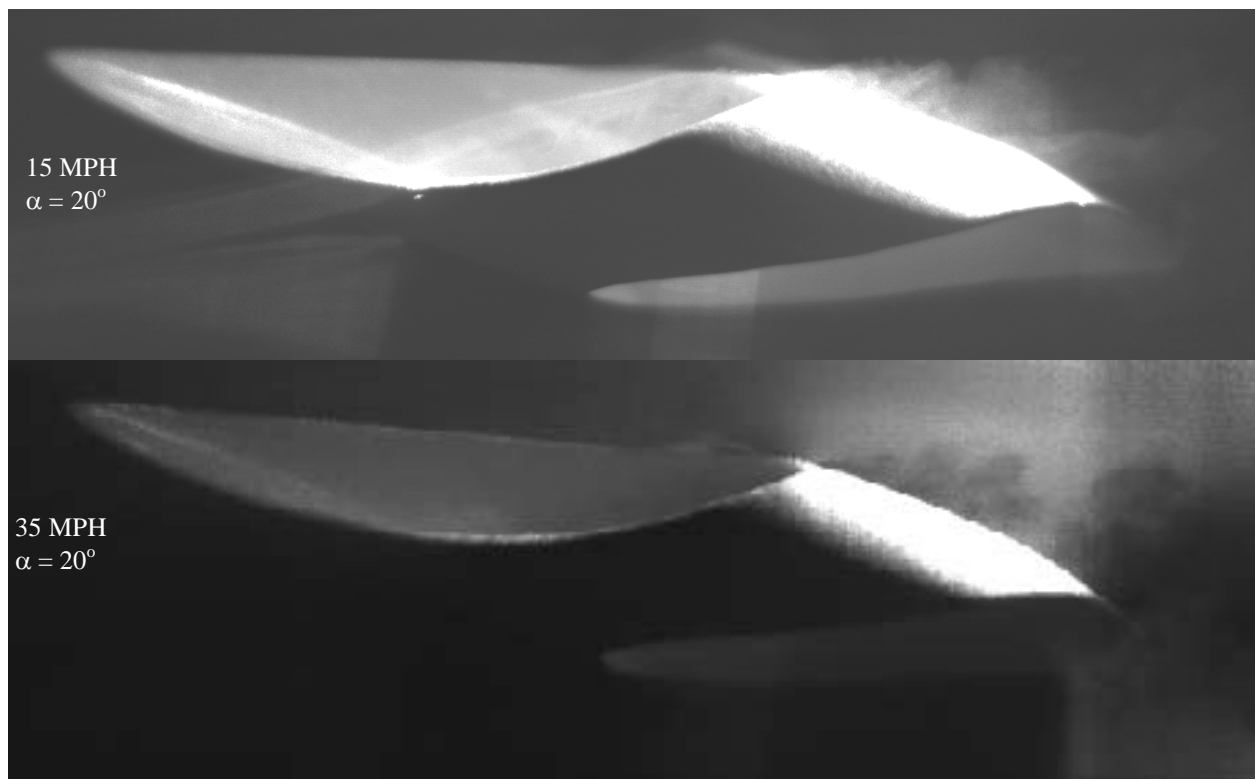


Figure 21: Leading Edge Vortex at 15 and 35 MPH and AOA = 20 degrees

1.4.2 AVUS CFD Analysis

This section documents the study carried out by AFRL/RBAC personnel to validate three-dimensional CFD models of the joined-wing configuration by comparing numerical results with those of experimental study. The three-dimensional solutions were obtained with the Air Vehicles Unstructured Solver (AVUS), an Euler/Navier-Stokes code developed in the Computational Sciences Branch of the Air Vehicles Directorate^{6,7}. AVUS is an unstructured, cell-centered, finite-volume, Godunov-type solver that uses least-squares gradient reconstruction and limiting for second-order spatial accuracy, and second-order, point-implicit time integration. It handles two and three dimensions, arbitrary cell types, and has been efficiently parallelized using Message Passing Interface (MPI). AVUS has been verified on a variety of cases, ranging from the exact Riemann problem to complex, real world problems^{8,9}.

Unstructured grids were used because of the relative ease with which they can be generated on complex or unusual geometries. VGRIDns^{10,11}, a program that has successfully demonstrated its ability to generate grids on very complex, complete aircraft configurations, was used to generate the tetrahedral boundary layer and free stream volume grids on the joined-wing configuration. A grid refinement tool was also used to combine tetrahedral cells near geometric surfaces into prismatic cells. This typically reduces the total number of grid cells by 20-30%, thereby reducing run times. An added benefit of prismatic cells is increased accuracy due to improved grid orthogonality near the boundary surfaces.

The computational geometry of the 6-inch model was generated by the Air Force Institute of Technology (AFIT) through means of laser scanning the Styrofoam model carved to specified shape by Ron Houck II. The geometry was cleaned up, reformatted, and supplied to AFRL/RBAC from UDRI in IGES form, Figure 22. A grid, representative of the configuration, Figure 23, was generated for the computational portion of this study. An initial grid was produced having a volume grid comprised of 926,757 cells. The results from the simulations performed on this grid proved to be too coarse, as they did not capture the viscous boundary layer and friction drag properly. The initial grid was refined to encompass a viscous layer resulting in a grid consisting of 1,177,726 cells with the first layer of grid cells being 0.0005

inches off the surface of the model. The domain boundaries relating to the surrounding airflow field were modeled using the Riemann invariant free stream condition, while the aircraft surface was modeled with an adiabatic, no slip condition.



Figure 22: Houck-Designed Six-inch Joined-Wing Aircraft.

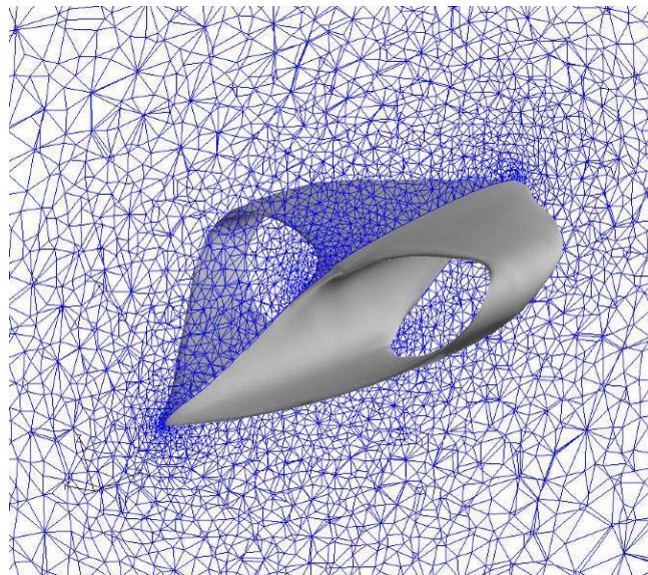


Figure 23: Computational Mesh Generated by AFRL/RBAC

AVUS was run in a steady-state condition and the solutions at 45 mph for an angle of attack sweep of -6 to 24 degrees were carried out until the forces along the streamwise axis of the model reached a steady-state condition. Each solution required about 2,000 iterations.

The surface pressure and Mach number contours for the coarse and subsequent refined grids are compared in Figure 24 and Figure 25. The flow over the bottom surface shows quite a bit of breakdown for the coarse grid, while the flow for the refined grid does not breakdown or dissipate as quickly. The refined grid represents a more accurate solution.

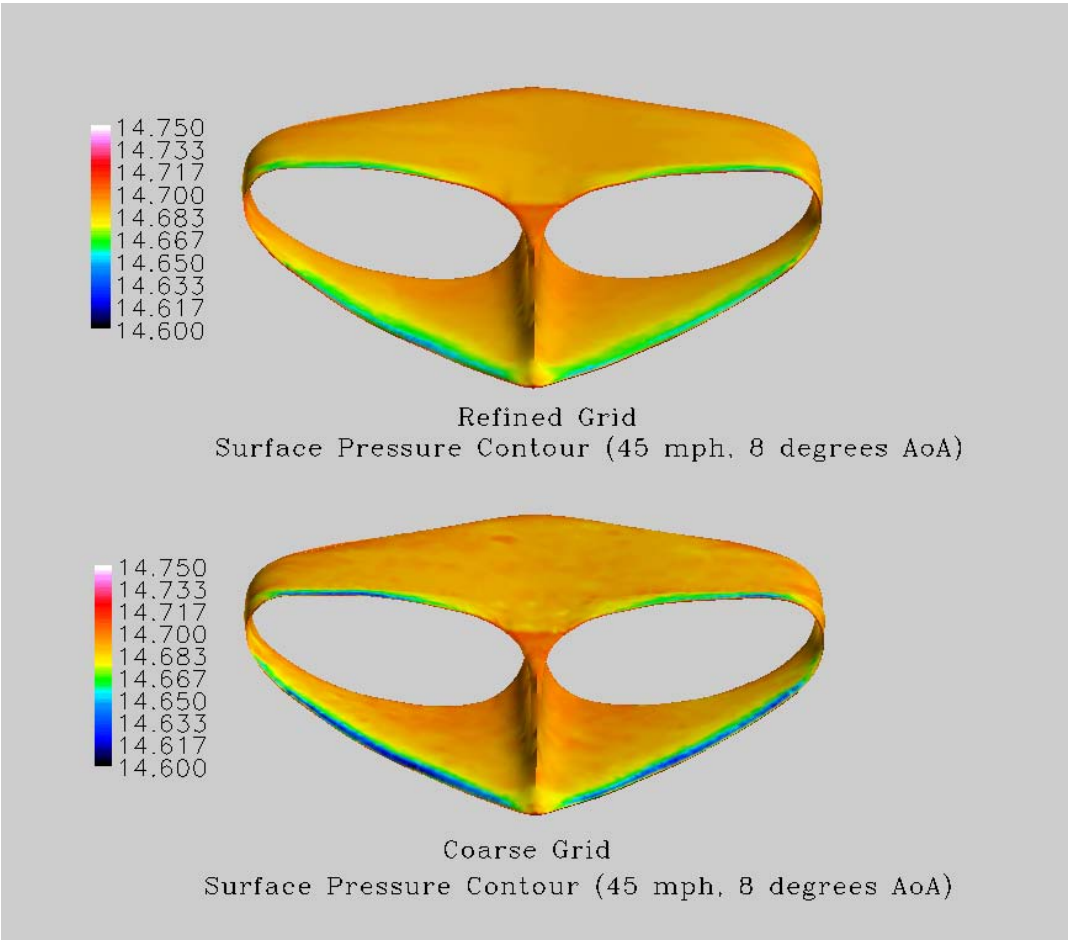


Figure 24: Surface Pressure for the Coarse and Refined Grids

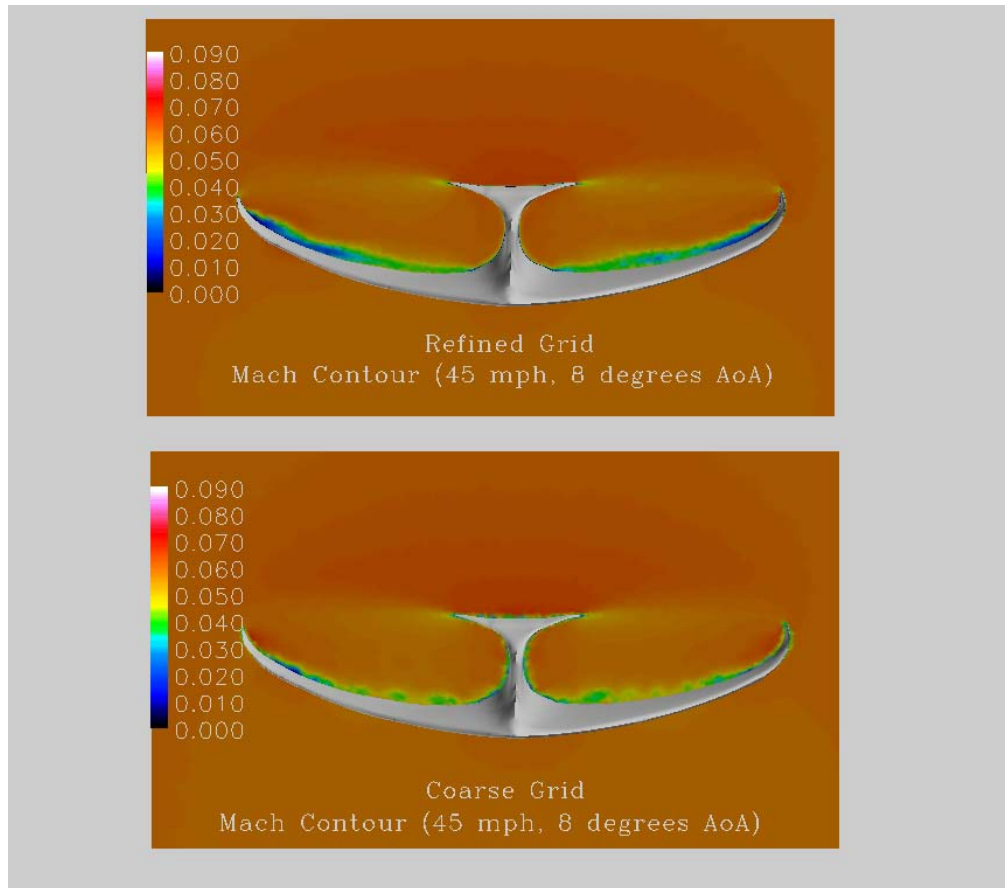


Figure 25: Mach Number Contours for the Coarse and Refined Grids

Upon completion of the initial angle of attack sweep, the aircraft designer mentioned that the aircraft demonstrated better flying qualities if hand launched in an inverted orientation. The computational grid was flipped (rolled 180 degrees) using an in-house conversion program. Simulations were then performed on this inverted grid at 45 mph at 8 degrees angle of attack. Surface pressure and Mach number contours are depicted in Figure 26, Figure 27, and Figure 28, respectively. As noted in Figure 29, Figure 30, and Figure 31, lift appears to increase; however, drag also increases at a higher rate causing a net reduction in the lift/drag ratio; the symbols marked 'flip' in these graphic represent the inverted configuration. These results demonstrate that the vehicle does not exhibit better flight characteristics in the inverted position as suggested. Also presented are characteristics for a scaled version of the model, which was investigated to understand Reynold's number effects; these symbols are marked 'Scaled (15 in)' in the figures below.

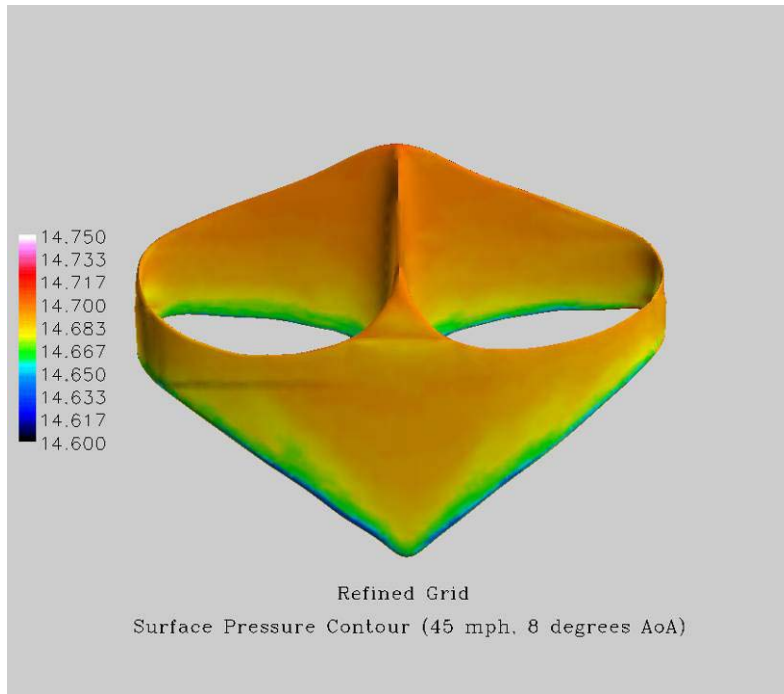


Figure 26: Surface Pressure: Inverted Configuration, Top View

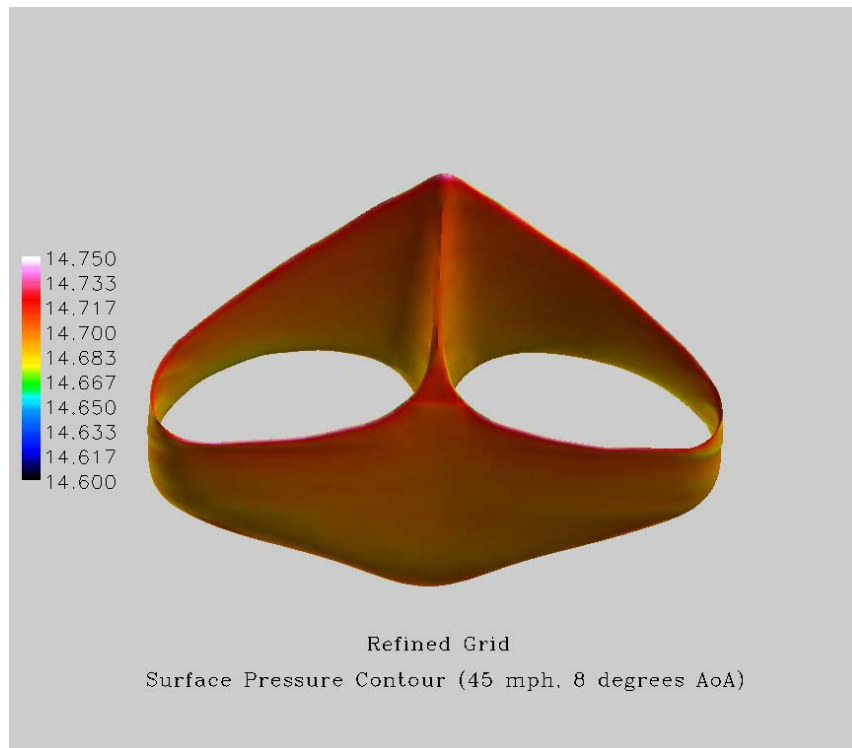


Figure 27: Surface Pressure: Inverted Configuration, Bottom view

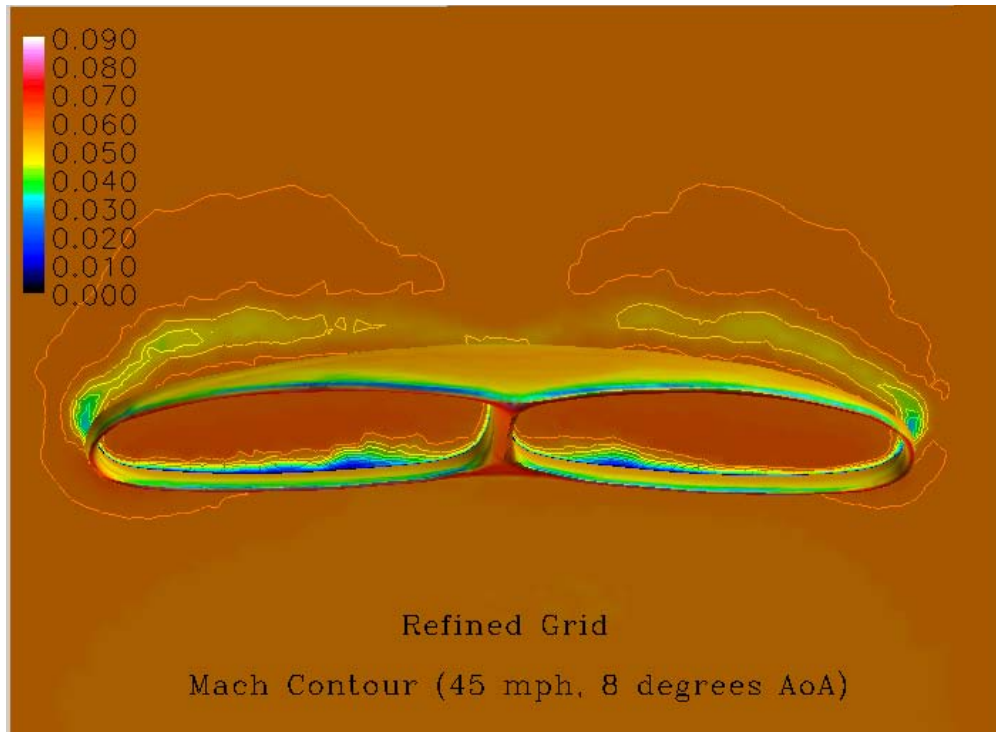


Figure 28: Planar Mach Number: Inverted Configuration, Front View

Results obtained from the computational analysis also were compared to experimental wind tunnel measurements provided by UDRI and are shown in Figure 29, Figure 30, Figure 31, and Figure 32. The offset (or shift) between the experiment and the computation may be accounted as a function of what was taken as the zero-lift reference line. The difference in the reference line is approximately 3 to 4 degrees which would shift the two sets of results into better agreement. Accounting for the offset, the CFD and experimental results are comparable within the allowable percentage set by AFRL/RBAC, <5%. Further investigation may be required to verify this zero-lift reference line issue.

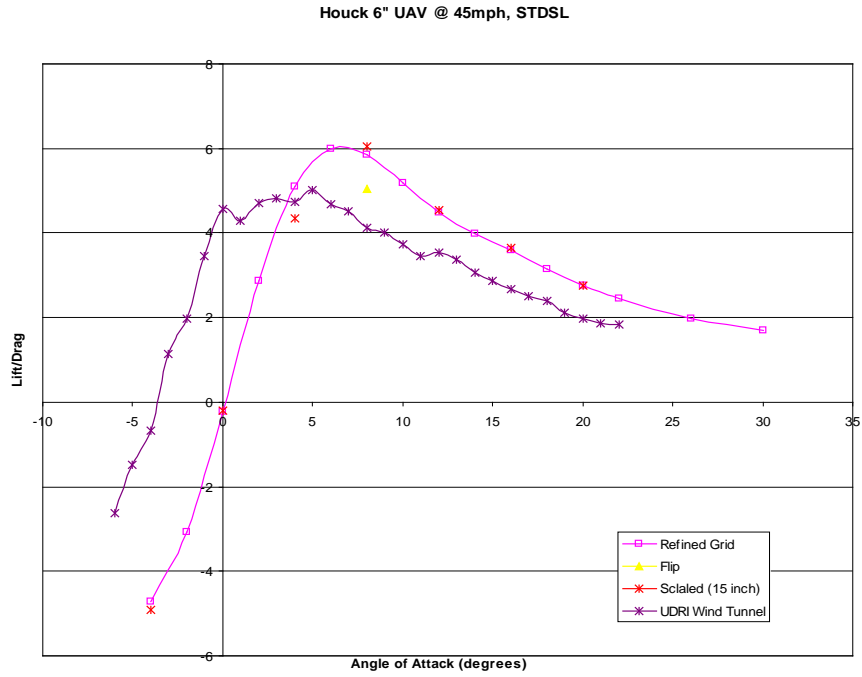


Figure 29: Lift to Drag Ratio versus AOA

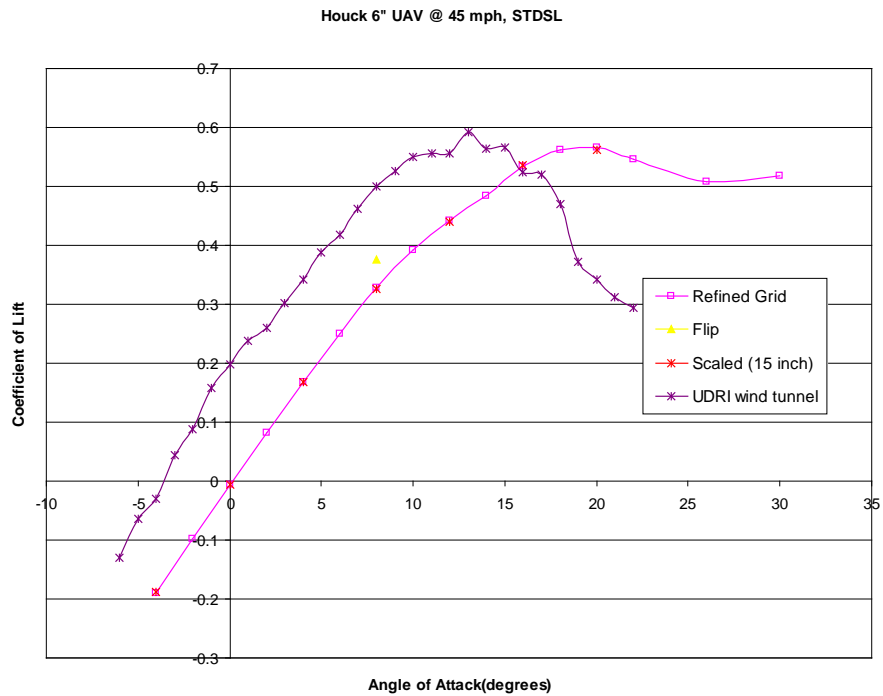


Figure 30: Lift Coefficient versus AOA

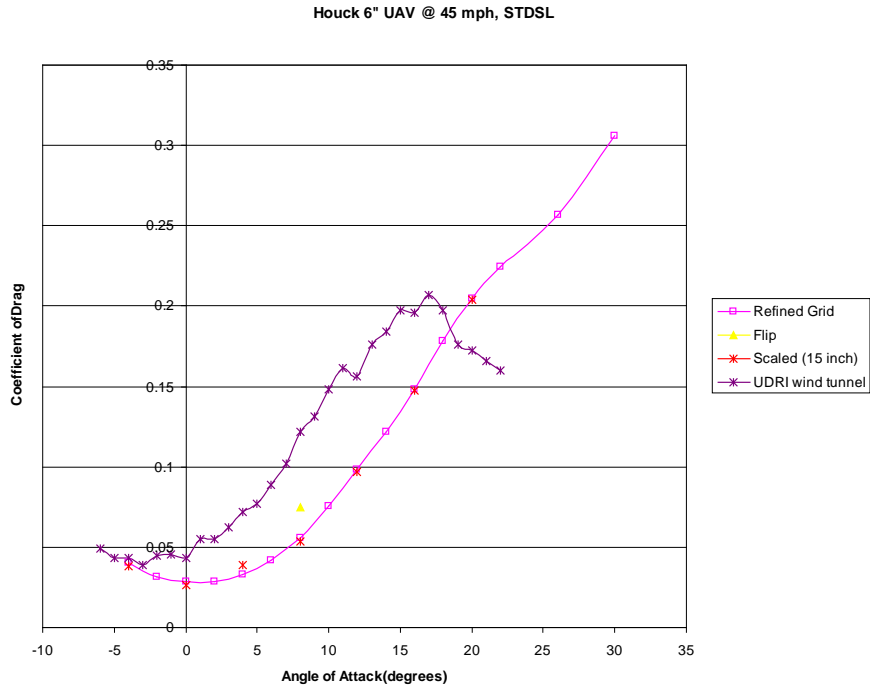


Figure 31: Drag Coefficient versus AOA

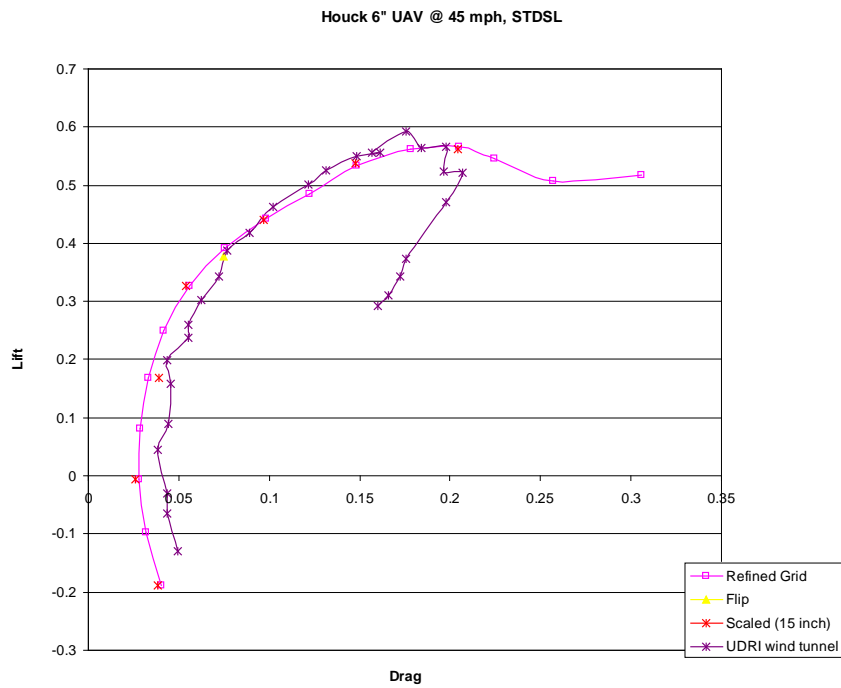


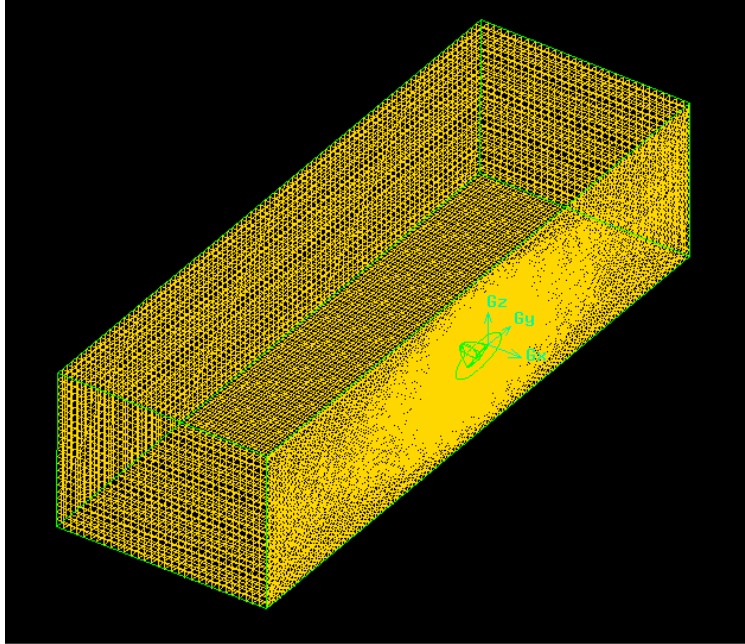
Figure 32: Lift Coefficient versus Drag Coefficient

1.4.3 FLUENT CFD Analysis

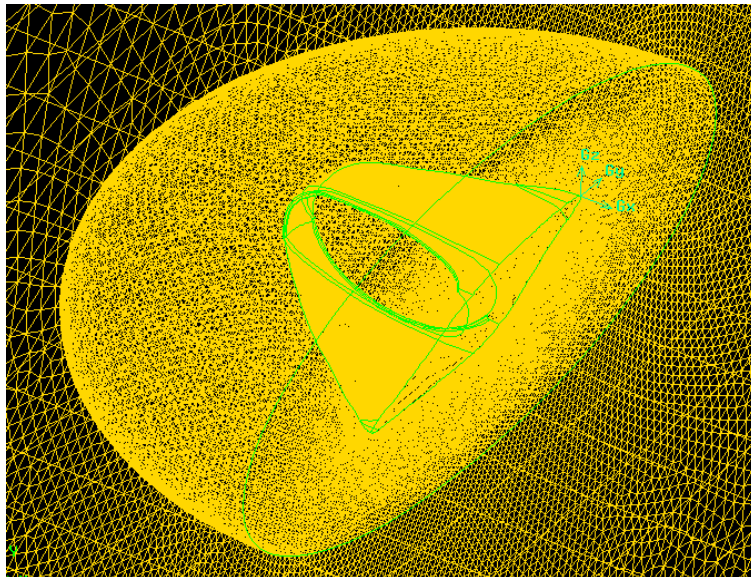
In order to complete the FLUENT CFD analysis, the first task was to convert the AFIT laser scan file into CAD geometry suitable for CFD analysis. After completing the CAD modeling phase described in Section 7.2, the CFD mesh was created in the pre-processor code GAMBIT. The extents of the flow domain were the same as those used in the AVUS CFD study: ten vehicle chordwise lengths in the upstream direction, ten lengths downstream, and ten span lengths to each side.

In GAMBIT, a small ellipsoid-shaped volume was created around the airfoil, inside which a fine tetrahedral mesh was generated. Outside of the ellipsoidal volume, in the outer region of the flow domain, a more coarse mesh was used. The total mesh size was approximately 1.4 million cells. As stated above, the airfoil was split at its mid-span plane and only half of the airfoil was modeled. The symmetry boundary condition was applied at the vehicle mid-span plane. The full domain mesh is shown in Figure 33a; the mesh detail in the vicinity of the airfoil is shown in Figure 33b.

An analysis of the mesh in GAMBIT revealed that the skewness was within allowable limits (approximately 0.84 maximum). The appropriate boundary conditions were defined in GAMBIT. The mesh was exported in the .msh file format, and imported into the FLUENT CFD program.



(a) Full Flow Domain



(b) Airfoil Detail

Figure 33: GAMBIT Mesh of the 6-inch Airfoil

In FLUENT, the CFD case was defined using the far-field-pressure boundary condition, and the gauge pressure, absolute temperature, velocity magnitude and velocity directions were assigned.

The far-field-pressure boundary condition enables the user to quickly make changes to the onset velocity direction without having to generate a separate mesh for each angle of attack.

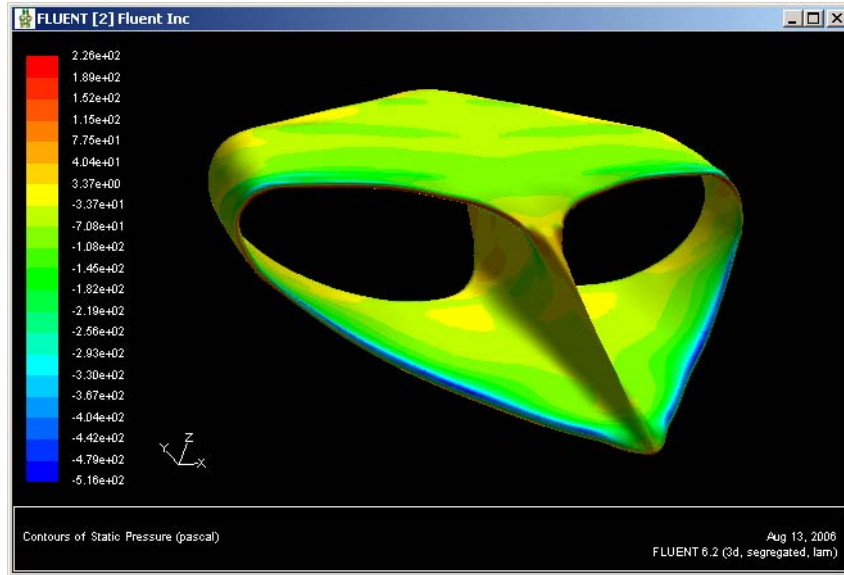
The chord-based Reynolds Number (Re) for the vehicle at 45 mph velocity and standard atmospheric conditions was approximately 195,000; therefore, all FLUENT cases were run using the laminar flow solver. Care should be taken in future analyses to change to a turbulent-flow solver if Re values should fall in the turbulent regime.

The FLUENT code was run at 45 mph velocity and angles of attack ranging from 0° to 22° . Each solution required between 2000 and 5000 iterations to converge, with higher angle-of-attack solutions requiring longer run times. This may be the result of large areas of flow separation downstream of the airfoil at high angles of attack, requiring longer computation time for the steady-state solution to be reached.

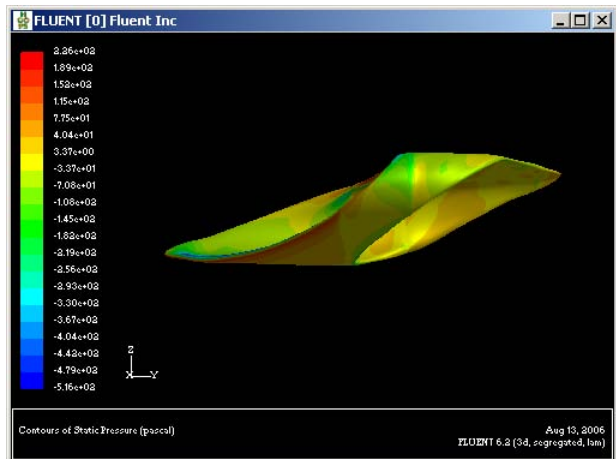
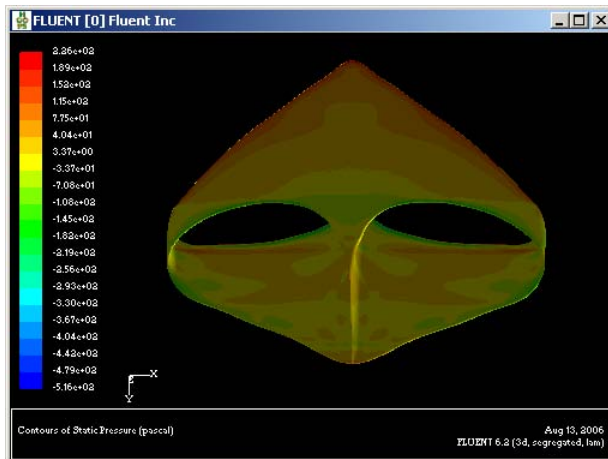
As described in the previous section, there is a discrepancy between the zero-degrees angle-of-attack reference used in the UD wind-tunnel test, and that used in the CFD analyses (AVUS and FLUENT). The difference in the zero-degrees reference angle required a shift of $+3.8^\circ$ in the UD wind tunnel data in order to correlate with the angles of attack used in the CFD models based on the difference in lift coefficient at zero angle of attack.

Contours of static pressure on the vehicle are shown in Figure 34. The case represented in Figure 34 is for a vehicle speed of 45 mph and angle of attack of 8° . Views are shown from the top-front (Figure 34a), bottom (Figure 34b), and side (Figure 34c) of the vehicle.

Figure 35 contains plots of key performance characteristics: (a) Lift Coefficient (C_L) vs. Angle of Attack (original wind tunnel reference angles); (b) C_L vs. Angle of Attack with $+3.8^\circ$ shift in zero-reference angle for the wind-tunnel data; (c) Drag Coefficient C_D vs. Angle of Attack (shifted test AOA); (d) Lift/Drag Ratio vs. Angle of Attack (shifted test AOA); and (e) Lift vs. Drag (shifted test AOA).



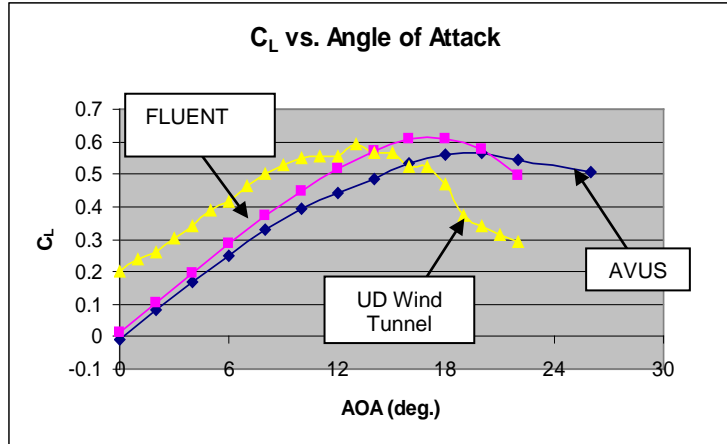
(a) view from front of vehicle, upper surface



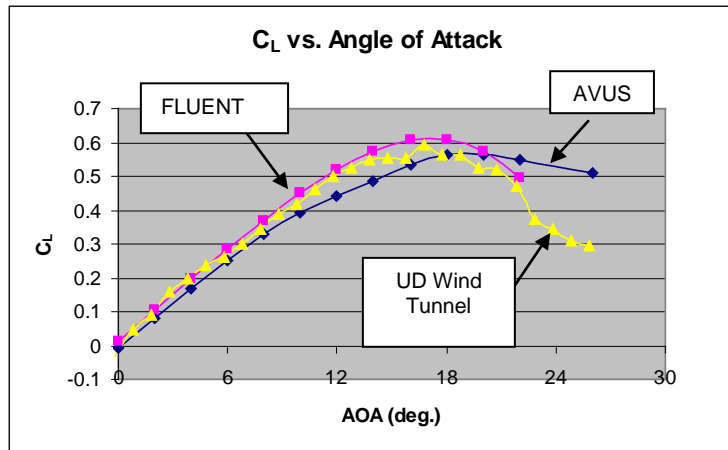
(b) view from bottom of vehicle (flow from top) (c) view from side of vehicle (flow from left)

Figure 34: Static Pressure Contours for 45 mph, AOA = 8°

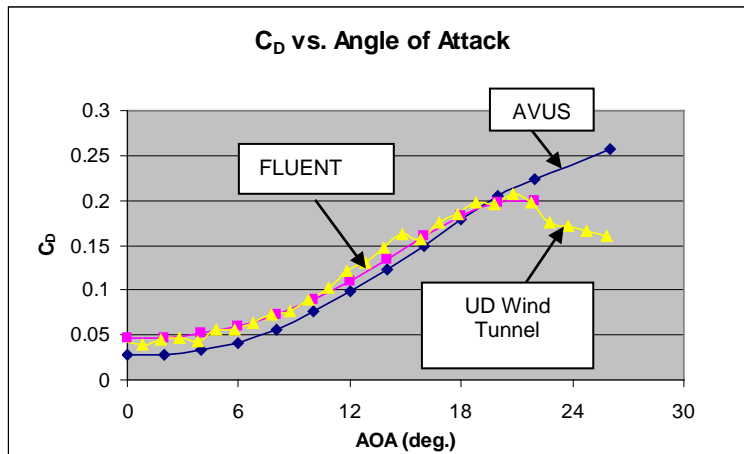
The plots of Figure 35 show that both FLUENT and AVUS results provide reasonable agreement with the UD wind tunnel test data. Results vary little in the range of 0° to 10° angle of attack; at higher angles of attack, FLUENT more accurately predicts the lift and drag behavior, but these angles lie outside the intended operating range of the vehicle. The difference in drag at low angles of attack is not well understood, but may be a function of run conditions and other computational settings used.



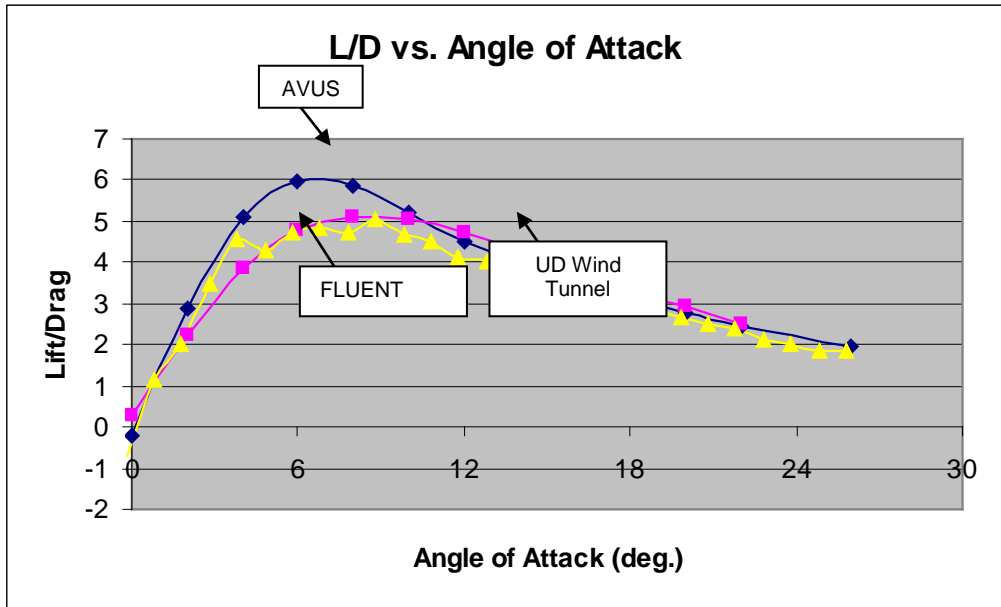
(a) without the shift in zero-degree reference for wind tunnel angle of attack



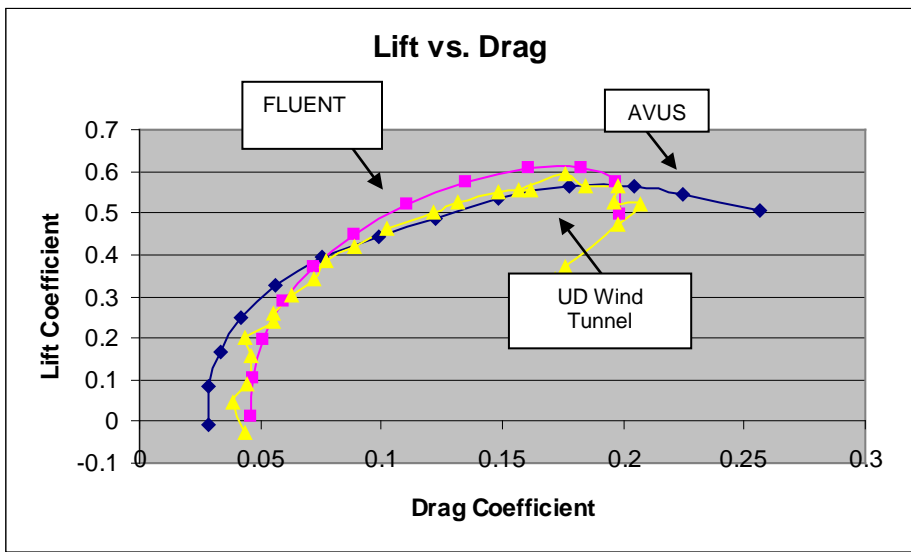
(b) with $+3.8^\circ$ shift in angle of attack for wind-tunnel test data



(c) C_D vs. AOA



(d) L/D vs. AOA



(e) CL vs. CD; all w/shifted wind tunnel reference AOA

Figure 35: CFD and Test Results for Lift and Drag Characteristics

A means of increasing the vehicle's aerodynamic lift is to add camber to the airfoil cross sections. Spanwise cuts through the vehicle indicate that the wings possess very little camber. Figure 36 shows three spanwise sections. The airfoil sections are faint, and are indicated by arrows in the following figures.

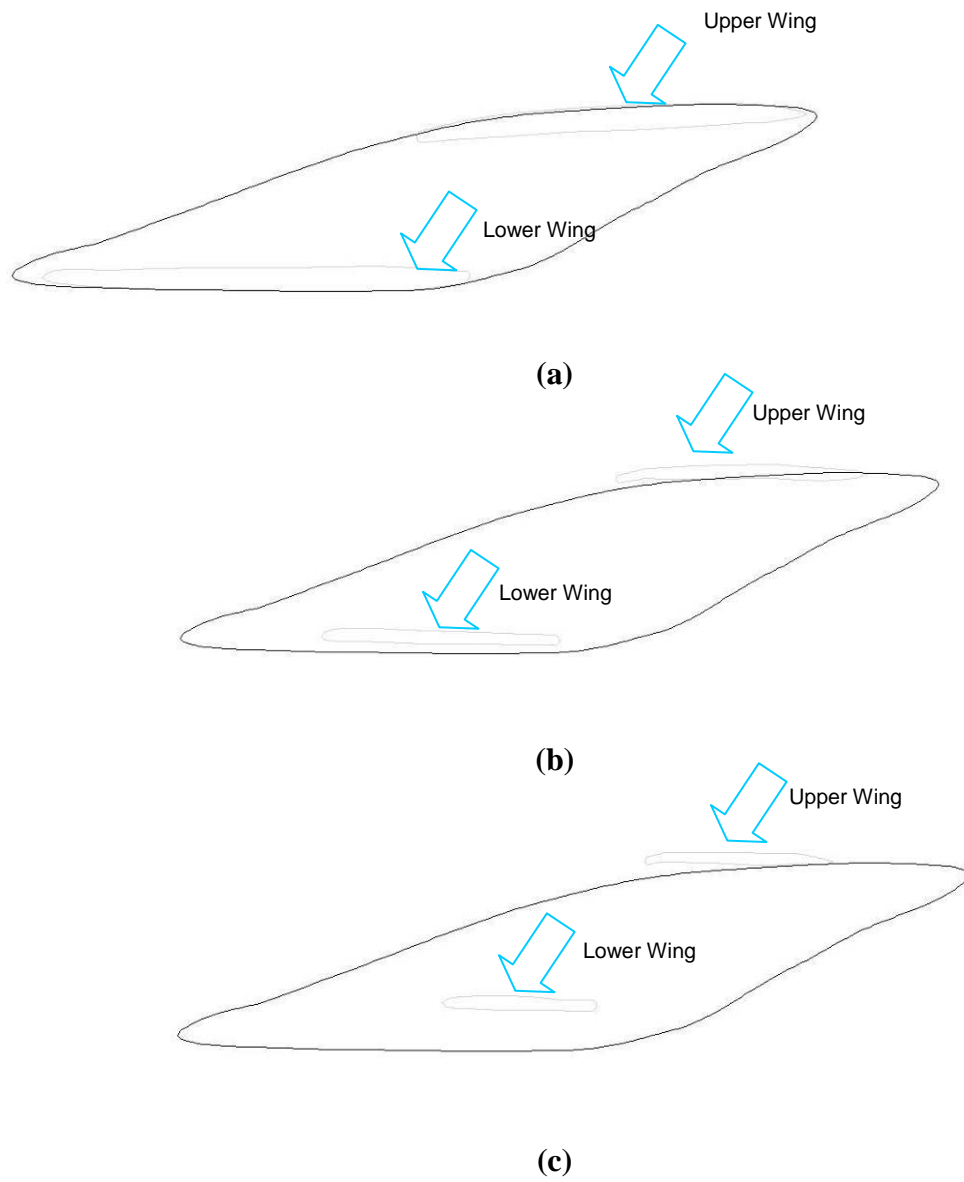


Figure 36: Spanwise Section Cuts Illustrating Lack of Airfoil Camber

The results of the FLUENT runs compare well with those of the AVUS CFD code and the experimental wind tunnel results. The 6" geometry shows no indication of classical, cambered airfoil sections along the lifting surfaces. This fact should be viewed in an optimistic perspective because it leads to the assumption that including high lift-to-drag airfoil sections will improve the aerodynamic performance of the configuration and might explain why the 6" prototype does not meet all of the threshold targets for performance.

1.5 Results

This section provides a summary of the three most significant Phase I results. For detailed results, see the individual sections of the report which detail the various types of analysis.

- The CFD (both AVUS and Fluent) lift and drag coefficient results track very closely with the experimental data. The Fluent results track the experimental post-stall behaviour more closely than does AVUS.
- Results from the NX3 model of the laser-scan data of the six-inch Houck configuration show that the prototype model is not constructed with airfoil sections, the shape is essentially that of a flat plate.
- The Houck configuration had mixed results with respect to the program measures of merit. Table 5 shows how the 6” Houck configuration compares to the target performance values. The drag coefficient at zero-lift target has been satisfied, the lift curve slope is lower than required and the Oswald’s efficiency factor is near (but below) the target value. The 6” Houck prototype configuration fell short of two of three performance targets. However, it was also determined that the prototype did not actually use any airfoil section along its lifting sections. Therefore, it can be supposed that a subsequent prototype which incorporates appropriate airfoil sections will show much improved performance.

Table 5: Performance of the Houck Configuration

Category	Target	Wind Tunnel	AVUS	Fluent
Drag Coefficient @ Zero-Lift:	$C_{D0} \leq 0.045$	0.04	0.028	0.046
Aircraft Lift Curve Slope:	$C_{L\alpha} \geq 0.09 / \text{deg}$	0.043	0.036	0.042
Oswald's Efficiency Factor:	$e \geq 0.8$	0.55 to 0.78	n/a	n/a

1.6 Conclusions

Conclusions based on the results of the experimental aerodynamic testing of the Houck configuration are that it compares well, however doesn't necessarily offer a performance *gain* over existing aircraft of the scale tested. The sole exception is a demonstrated strong potential for increased gust stability due to the absence of a sensitive laminar separation bubble at pre-stall angles of attack. In fact, using flow visualization, the flow was found to be largely detached throughout the range of operable angles of attack. This is a detriment to aerodynamic performance, although it has the potential to provide a more stable MAV platform in gusty real-world conditions.

Referring to Torres and Mueller¹², in the range of Reynolds numbers for the aspect ratio tested (depending on definition used for the Houck configuration), the maximum obtainable value of lift curve slope, $C_{L\alpha}$, is between ~0.05 (AR2) and ~0.06 (AR4). Maximum lift to drag ratio (L/D) values of simple planforms tested (again in this range of Re and AR), the best of which is considered to be the inverse Zimmerman planform, are ~6. Though sometimes peaking to values of close to 9.0, these are not practical flyable L/D values and should not be considered in the context of the performance of an air vehicle.

Reasonable values for Oswald Efficiency Factor are suggested¹³ in the range from 0.6 to 0.7 with historical values for flat plates being even smaller at approximately 0.5. No mention of base

drag (C_{D0}) values is made as this criterion was considered reasonable and was met without difficulty regardless of the suggested definitions used for S_{ref} .

It is believed that the combination of criteria originally set forth is in fact unobtainable under the conditions tested by any present MAV with a similar Aspect Ratio. The performance of the Houck configuration is comparable with the aforementioned values cited in the literature. Whilst the max L/D value is 5.3, it is quite clearly in a usable range devoid of sensitivity to laminar separation bubbles/burst as is commonly found in this flow regime.

Assuming a monoplane Aspect Ratio of 2.0, e is in the range from 0.55 to 0.78, and lift curve slope is in the range just below 0.055. These values again compare well to the cited data. Thus, based on the scale and geometry tested, the Houck configuration compares reasonably well though offers no clear advantage with the exception of potential gust tolerance for the 6-inch scale model.

The performance of the 15-inch model was similar to that of the 6-inch model. In this instance, the lift to drag ratio of the 15-inch Houck configuration shows none of the improvement expected with the consequent increase in scale.

2 Phase II: Aerodynamic Evaluation of the 24-inch Model

2.1 Introduction

The Phase II work concentrated on the detailed performance evaluation of a twenty-four inch wingspan model. The primary result of the modeling and analysis was the determination that the experimental and CFD methods provided good agreement. The primary conclusion of Phase II is that based on analysis to date, the Houck configuration offers no significant advantage over a more conventional vehicle.

This section details the effort during Phase II of the program. The purpose of this phase was to employ theoretical and experimental techniques to better understand the aerodynamics of the Houck airfoil concept using a twenty-four inch wingspan prototype. This report discusses the configuration data, CAD modeling, aerodynamic modeling, results and conclusions of Phase II.

Phase II efforts utilized an improved Houck prototype with airfoil wing sections and a twenty-four inch wing span (versus the six-inch wing span prototype used in Phase I). Principal Phase II participants of the collaborative team were IHE, UDRI, AFRL/RBAC, and AFIT.

Deliverables for Phase II Detailed Performance Evaluation were:

1. Complete CAD documentation of the refined Phase II configuration
2. Estimates of mass properties
3. Wind tunnel data
4. CFD computations
5. Written report

2.2 Configuration Data

The Houck Aircraft consists of an upper and lower set of wings joined at the two wingtips by curved flow guides. These flow guides are claimed to reduce wingtip vortices associated with lift production of finite span aircraft wings. This reduction is accomplished by the gradual decrease of camber from the top of the lower wing as it transitions to the bottom of the upper wing where the camber is zero.

The model (depicted in Figure 37) is approximately twenty-four inches in both length and wingspan. The volume is 380 cubic inches. Using foam with a density of 2 lb / cu ft gives a mass of 0.44 pounds. Figure 38 contains all the inertial information for the Phase II evaluation model.

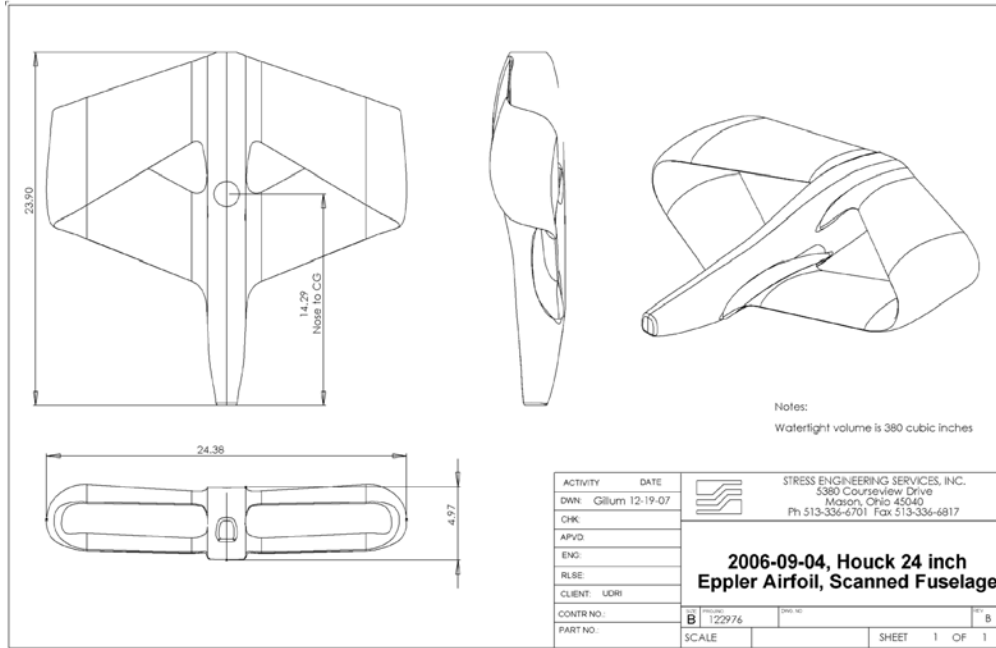


Figure 37: Houck Evaluation Model for Phase II

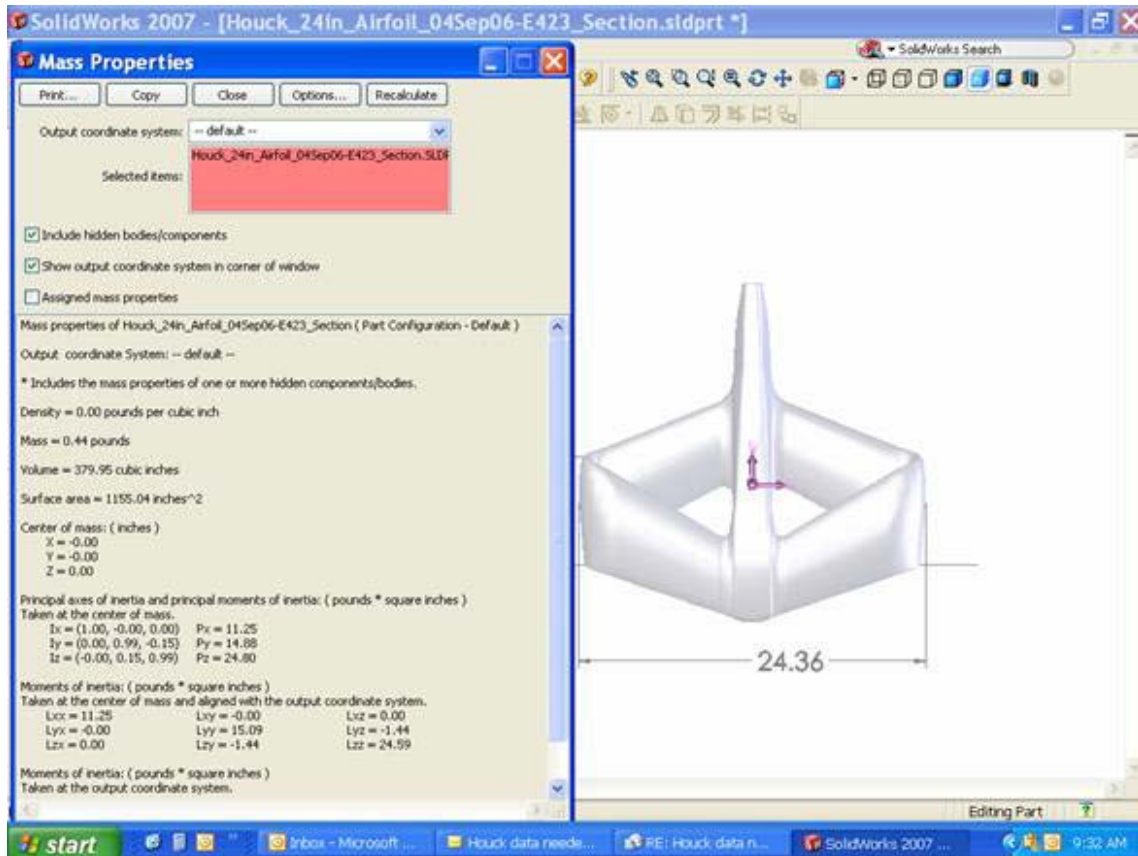


Figure 38: Inertial Data for Phase II Evaluation Model

2.3 CAD Modeling

Phase II analysis included aerodynamic analysis using AVUS CFD to determine performance characteristics. To perform the CFD meshing and analysis, an accurate 3D solid model of the airfoil was needed. A CAD Modeling effort was undertaken in order to provide a suitable model for CFD analysis. The specific efforts required included: rebuilding to eliminate coarse edges, improving the definition of the trailing edge of the fuselage, rebuilding the section curves through the fuselage, building wing surfaces from lofted curves, and uniting the wing and fuselage. Based on lessons learned during Phase I of the program, Unigraphics NX3 was used for all CAD modeling tasks.

The CAD geometry provided was a triangulated mesh derived from a laser-scan of the prototype airfoil. The geometry was very coarse, which made it unsuitable for meshing. Figure 39 illustrates the coarseness of the scanned model. The airfoil geometry was rebuilt in the 3D CAD program Unigraphics NX3.

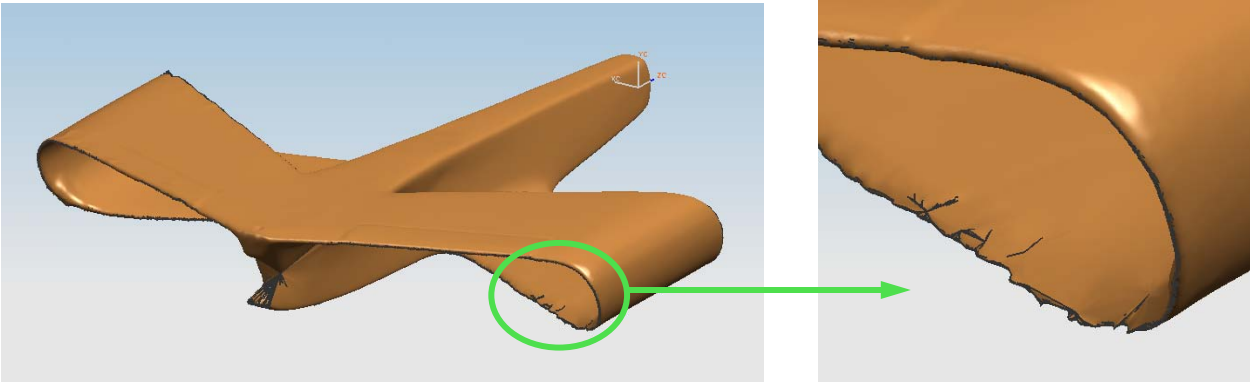


Figure 39: Illustration of Coarse Edges in Scanned Model

In addition, the trailing edge of the fuselage was poorly defined as shown in Figure 40.

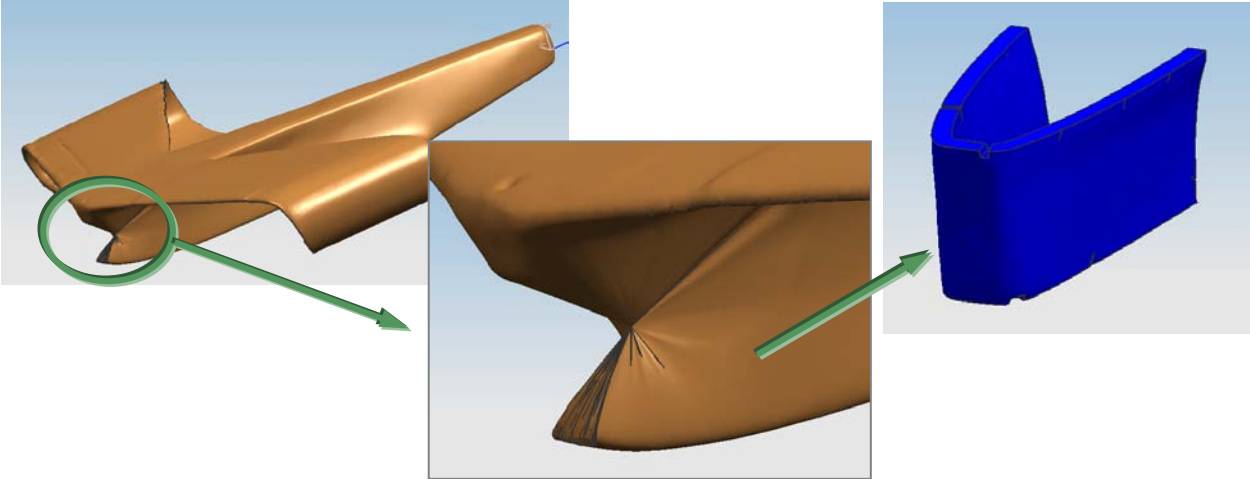


Figure 40: Illustration of Initial Trailing Edge Definition

The fuselage body was generated using section curves. These curves were then lofted to create an improved fuselage body as shown in Figure 41.

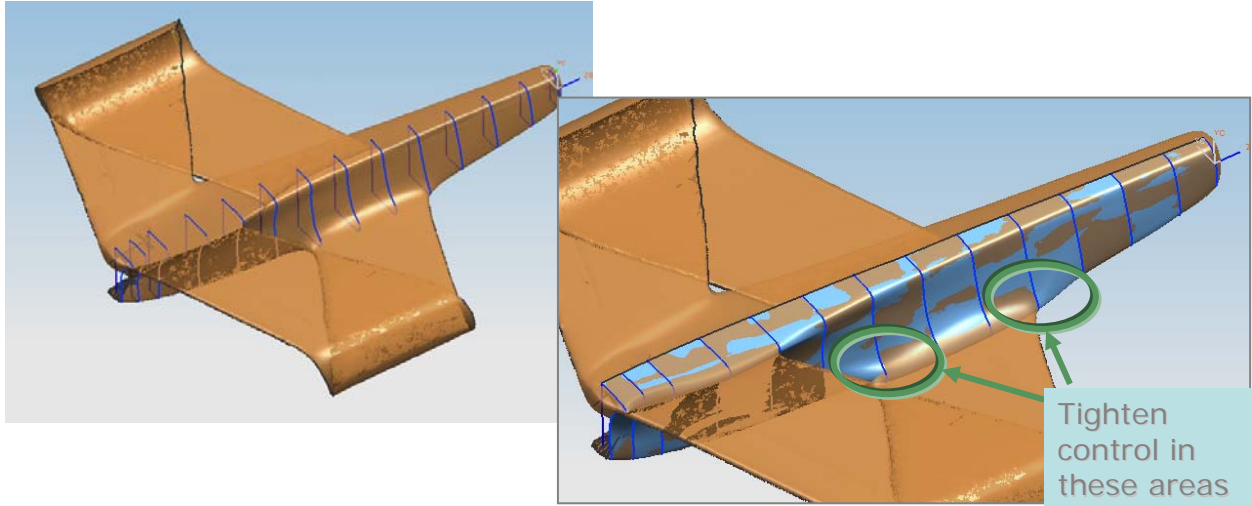


Figure 41: Rebuilding of the Fuselage Body

Figure 42 illustrates the lofted curves used to rebuild the wing surfaces.

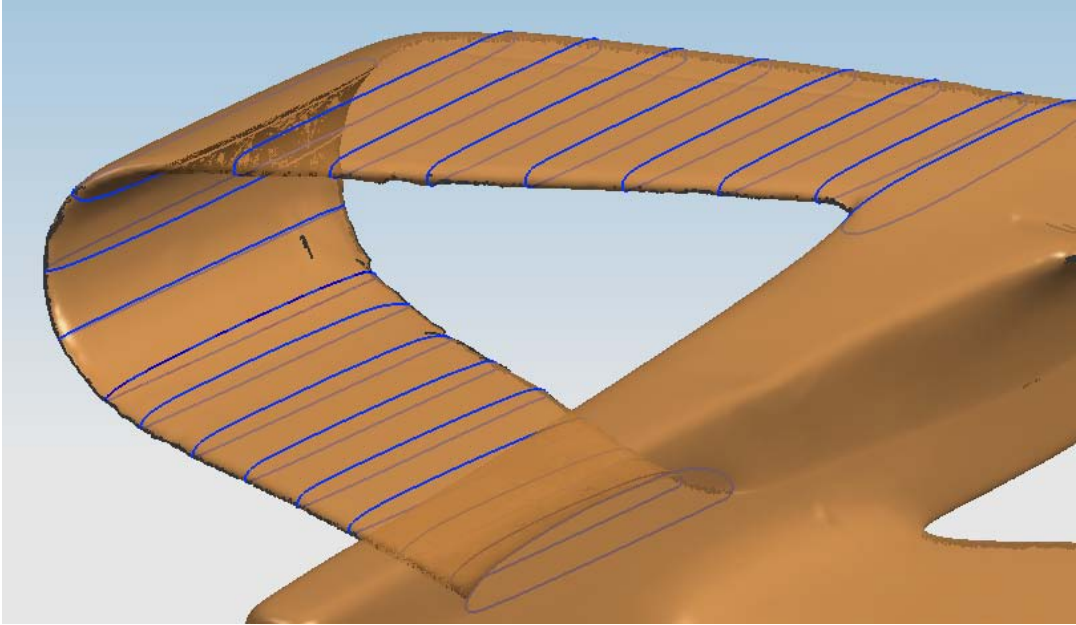


Figure 42: Lofted Curves Used to Rebuild Wing Surfaces

At the completion of the CAD Modeling effort, the rebuilt model was available for CFD analysis.

2.4 Aerodynamic Analysis

Three aerodynamics analysis efforts completed during Phase II are documented below. These analyses include the Wind Tunnel Analysis, the Hot Wire Analysis, and the AVUS CFD Analysis.

Additional wind tunnel investigations for this program not discussed in this report were completed by Lt. Michael Walker and ENS Dermot Killian. These efforts are documented in AFIT theses AFIT/GAE/ENY/07-M30² and AFIT/GAE/ENY/07-709³, respectively.

2.4.1 Wind Tunnel Analysis

Wind Tunnel testing was performed with a twenty-four inch wingspan prototype Houck model. The primary independent variable tested was aileron setting. Three aileron settings used in the testing: no aileron deflection, 20° trailing edge up aileron deflection, and 20° trailing edge down aileron deflection. Three speeds were also used for wind tunnel testing: 20 mph, 30 mph, and 40 mph. During testing the Angle of Attack (AOA) was varied from -5° to 15° as shown in Figure 43.

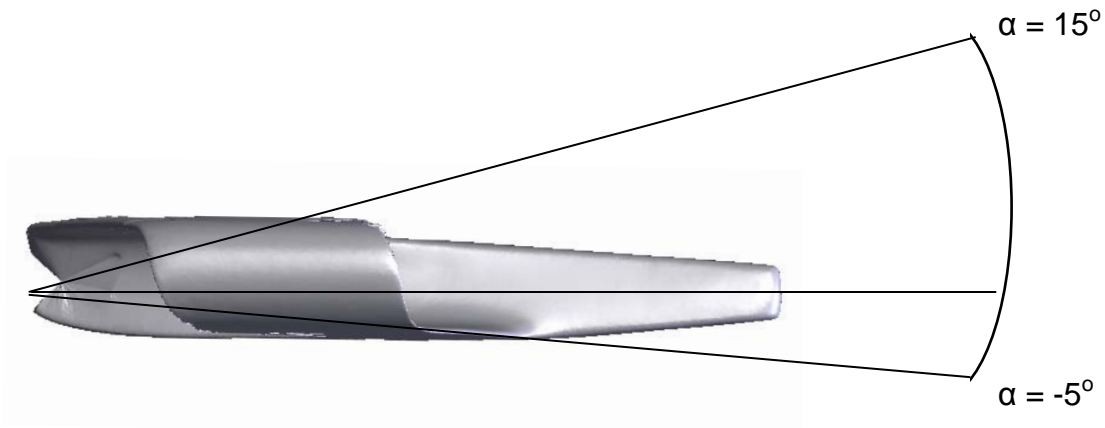


Figure 43: Angle of Attack Range Used in Wind Tunnel Testing

Table 6 records the testing conditions and geometric parameters.

Table 6: Wind Tunnel Testing Conditions and Geometric Parameters

Testing Conditions

Mass = 0.89824897 kg
 T_{room} = 74.6° F
 P_{barro} = 28.8058 inches

Geometric

Body_Volume = 248.37 cubic inches
 Wing_Area = 289.3 square inches
 c_{bar} = 12.265 inches
 span = 23.58 inches
 root_chord = 16.64 inches
 CG located at ¼ chord of planform

Figure 44 is a graph of the wind tunnel results for lift over drag versus AOA for various aileron settings and speeds. Additional wind tunnel test results can be found in Appendix A.

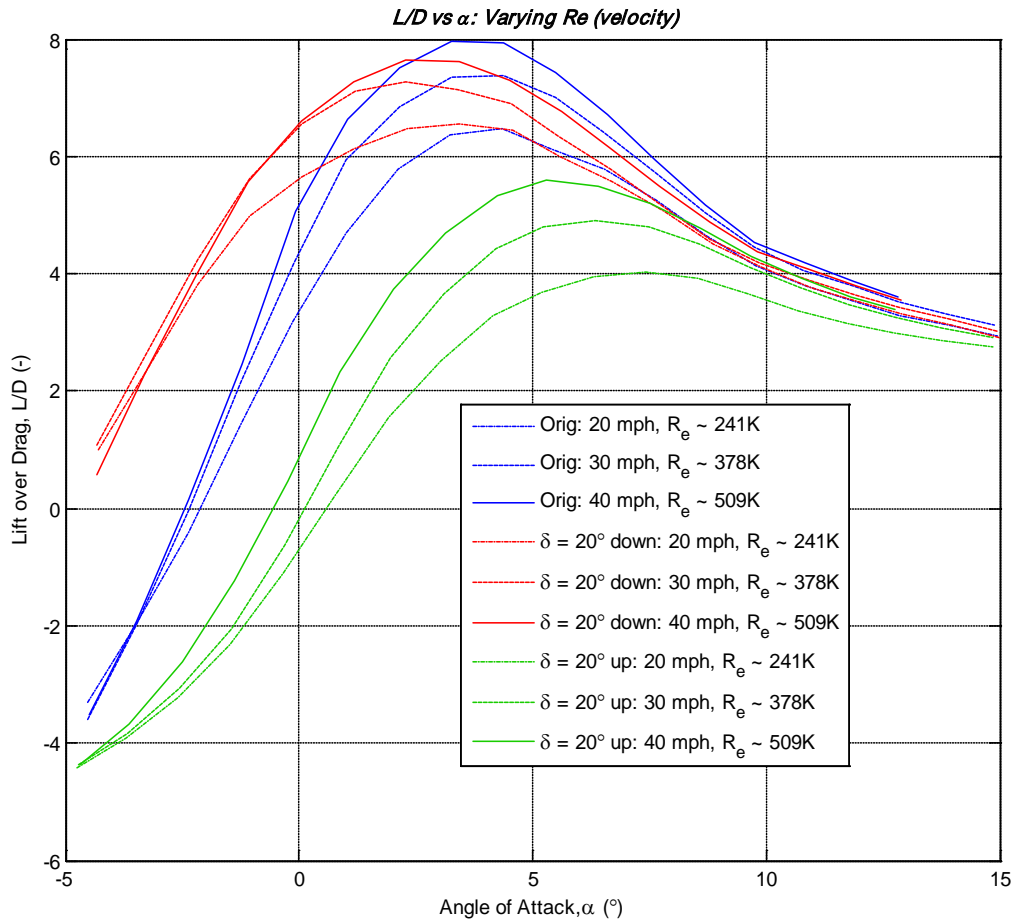


Figure 44: Lift Over Drag vs. AOA Wind Tunnel Results

2.4.2 Hot Wire Analysis

Hot Wire Analysis was used to record the velocity behind the wing of the Houck model in three dimensions. This testing was performed in the wind tunnel using the three aileron settings given in the previous section and AOA values of -2° , 4° , and 8° . The testing grid was 150 mm by 200 mm. The path of the hot wire probe is shown in Figure 45.

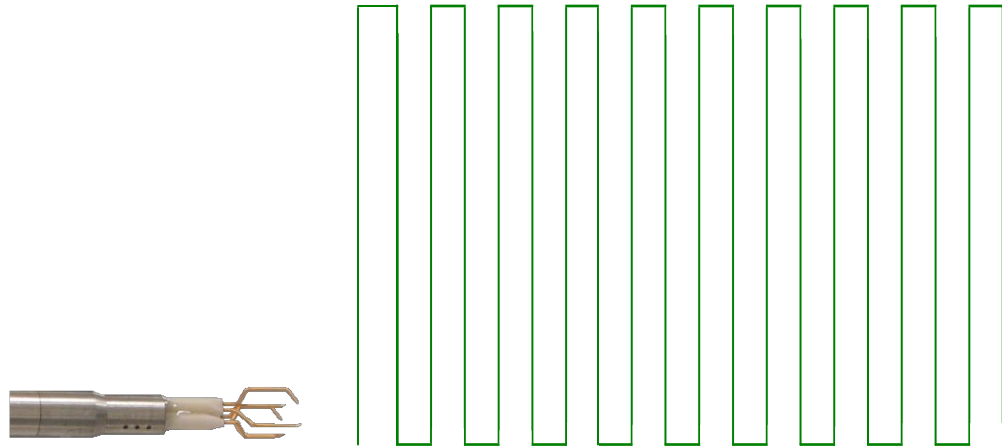


Figure 45: Path of the Hot Wire Probe

A total of 1271 grid points were measured for each run. Figure 46 is a graphical illustration of the hot wire data collection zone from the back, top and side views.

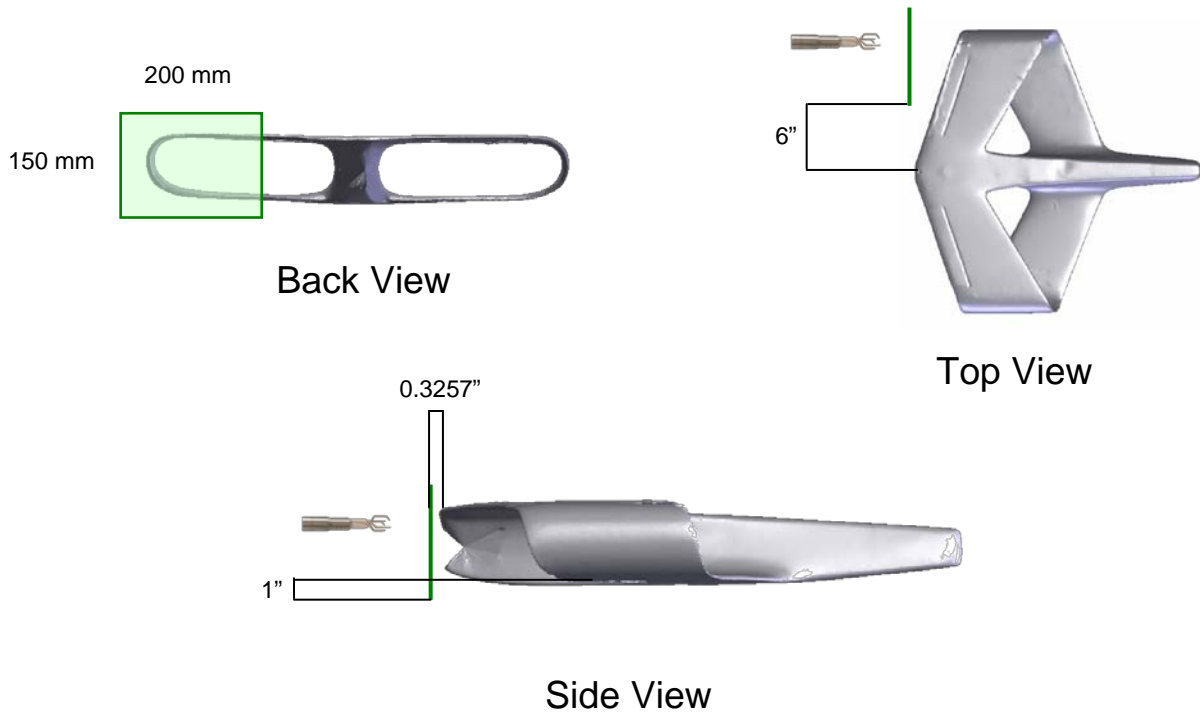
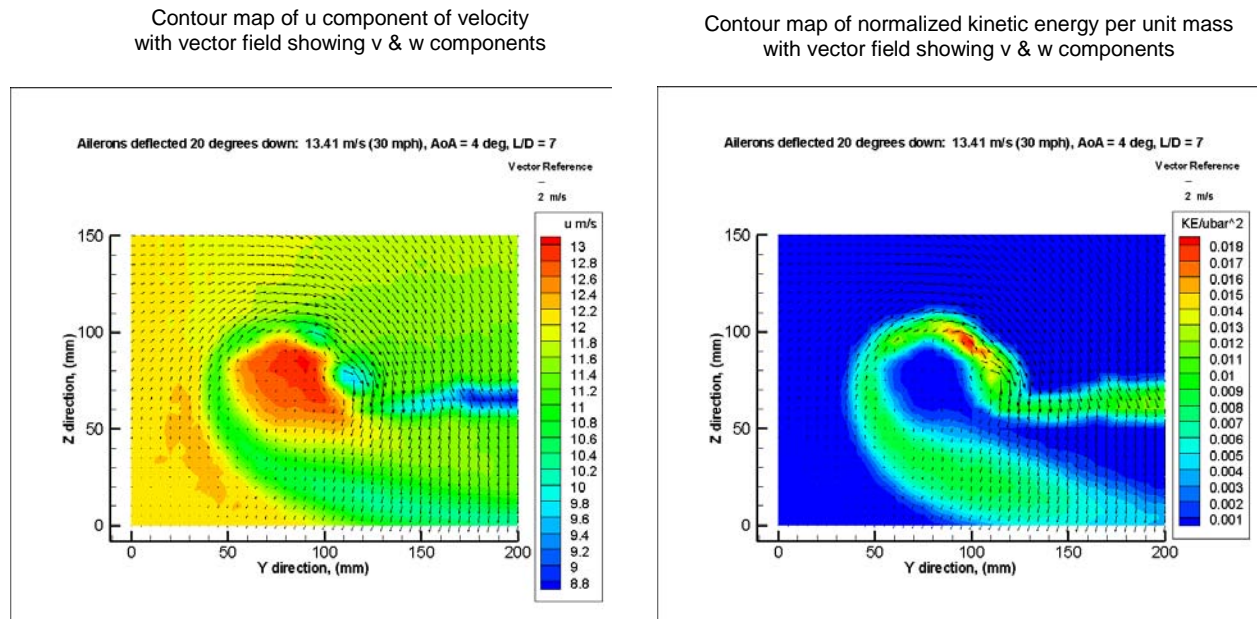


Figure 46: Three Views of the Hot Wire Data Collection Zone

Contour maps can be made from the grid point data. Vector plotting can also be performed. Because the velocity measurements are in three dimensions, vector fields can be placed over the contour maps. Figure 13 illustrates the results for an aileron setting of 20° down, and $AOA = 4^\circ$. The complete results of the hot wire analysis can be found in Appendix A.



2.4.3 AVUS CFD Analysis

The computational geometry for this study was generated from a CAD file created from coordinates obtained by the Air Force Institute of Technology (AFIT) by means of laser scanning the Styrofoam/epoxy resin model carved to shape by Mr. Houck. The geometry was rebuilt by UDRI and supplied to AFRL/RBAC as a parasolid model.

The three-dimensional Computational Fluid Dynamic (CFD), solutions were obtained with the Air Vehicles Unstructured Solver (AVUS), an Euler/Navier-Stokes code developed in the Computational Sciences Branch of the Air Vehicles Directorate^{6,7}. AVUS is an unstructured, cell-centered, finite-volume, Godunov-type solver. AVUS uses least-squares gradient

reconstruction and limiting for second-order spatial accuracy, and second-order point-implicit time integration. It handles two and three dimensions, arbitrary cell types, and has been efficiently parallelized using Message Passing Interface (MPI). AVUS has been verified on a variety of cases, ranging from the exact Riemann problem to complex, real world problems^{8,9}.

An unstructured grid was used because of the relative ease in which a grid can be generated on complex or unusual geometry. ICEMCFD was the software chosen to generate the unstructured volume mesh used by the AVUS CFD solver. The initial process is to generate a volume mesh composed of tetrahedra for the freestream surrounding the model out to the farfield, generating a surface triangulation of the model in the process. The model grid is then checked for errors, volume and surface mesh smoothed, and checked to ensure cell quality is within an acceptable range. Prisms are then extruded orthogonal to each surface triangle on the model with specified initial distance and exponentially grown from the surface for a specified number of layers. Ten prism layers were created with an initial spacing of 0.001” which would produce an average y^+ value of approximately 1 or better for most of the model. The resulting grid was comprised of 904,290 tetrahedra and 557,450 prisms for a total of 1,461,740 cells.

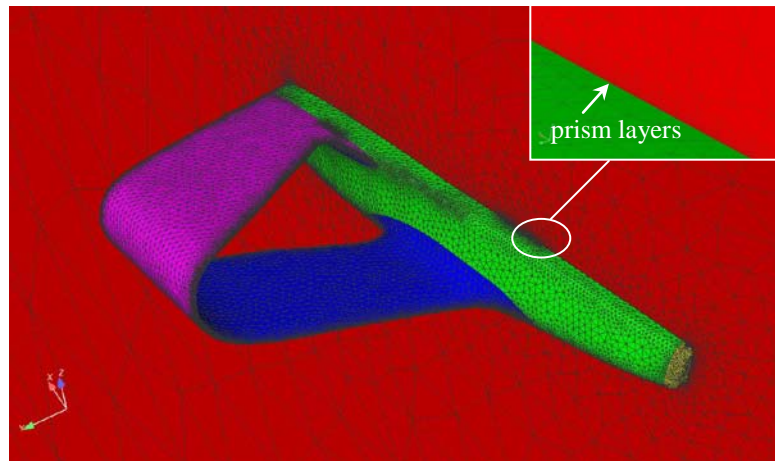


Figure 48: Computational Mesh Used by AFRL/RBAC

Computational resources were greatly reduced by modeling only half the model, taking advantage of the symmetrical nature of the vehicle. A natural size function was employed which permits the software to choose the surface triangle size based on regions of high curvature such as along the leading edges. Care was taken however to limit the natural sizing in certain regions

such as along the wing root, where it was necessary to create larger surface triangles to smooth over geometry imperfections such as bumps or dents that would cause problems while extruding the prism layer. Tight concave regions will cause prisms to grow into each other, limiting the number of layers possible or even producing a corrupt grid. Figure 49 illustrates this problem, showing why it was necessary to use larger surface triangulation on the wings. Ideally it would have been desirable to use a somewhat smaller surface triangulation on the wings, as ultimately the density of cells clustered around the model and especially the space between the wings is tied to the size of the surface triangles.

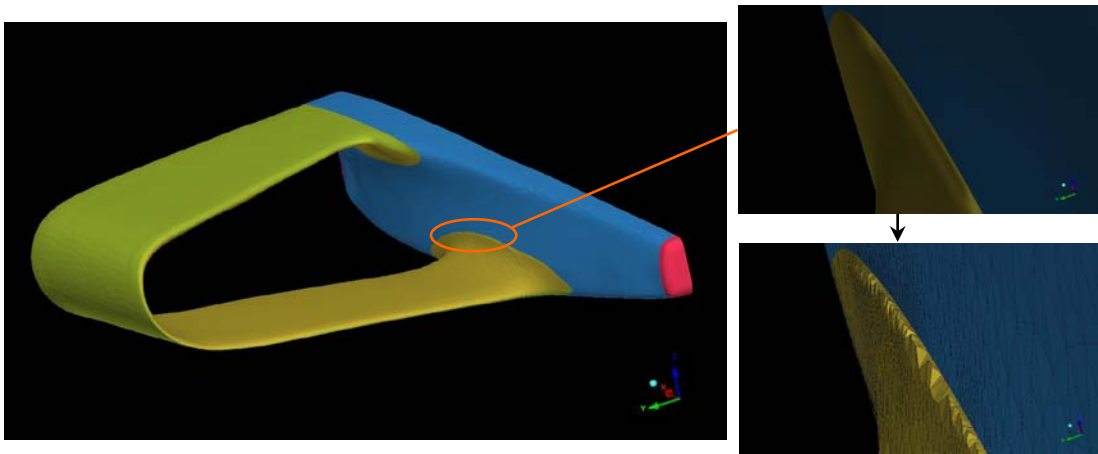


Figure 49: Example of Surface Imperfection

AVUS solutions were run in a steady state condition at 40 mph over an angle of attack sweep of -2.8 to 13.2 degrees. Boundary conditions were set to match the wind tunnel conditions as precisely as possible, with freestream pressure set 14.249 PSI and temperature set to 533.7 degrees Rankine. Spalart-Almaras was the turbulence model used for these calculations. Each solution was run until it could be determined that the forces and moments along the streamwise axis had reached a steady-state condition. Low angle of attack solutions were converged in approximately 5000 iterations, while higher angles of attack, especially where flow separation was noted, required 10,000 – 15,000 iterations.

Initial comparison of computational results with wind tunnel data provided by AFIT¹, Figure 50, shows reasonable correlation, but the data appears to be shifted. Since the lift curve slope of both wind tunnel data and computational data are nearly parallel it is reasonable to assume there

is a discrepancy with respect to the zero degree angle of attack reference line. It was mutually agreed that the flat planar surface at the aft end of the model where the sting enters would be used as a plane of reference. Differences between the actual CAD model received, the actual wind tunnel model and physically measuring the angle relative to vertical on the aft surface of the model may account for this.

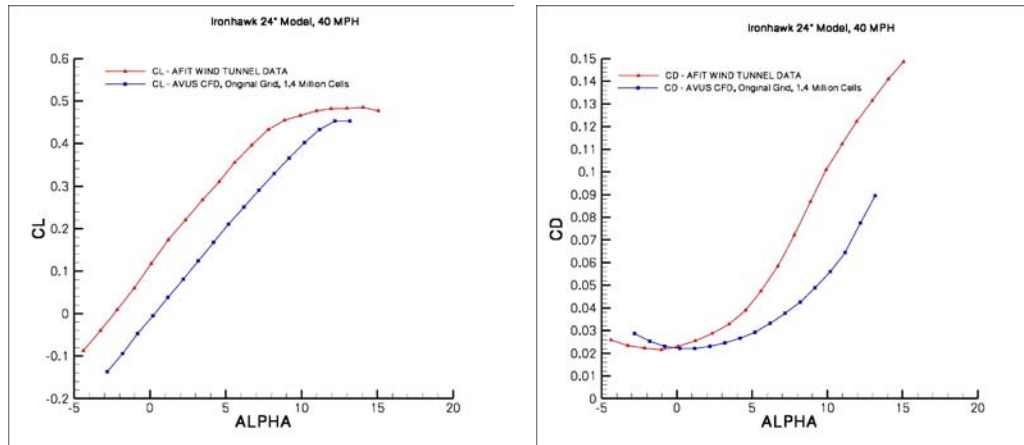


Figure 50: Initial Comparison of CL and CD Results

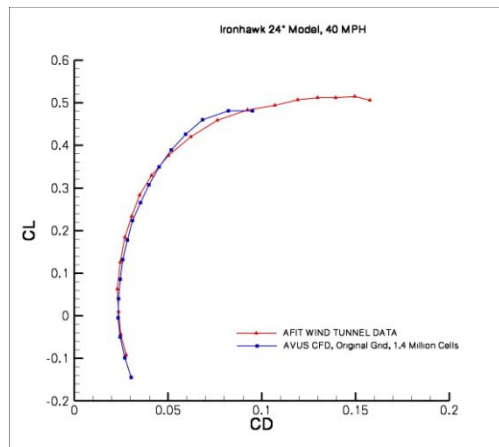


Figure 51: Comparison of CL vs. CD Results

AFIT and UDRI agreed that the wind tunnel data should be shifted by positive 2.6 degrees. This decision is also supported by the plot of lift coefficient plotted against drag coefficient in Figure 51, which is independent of angle of attack and shows good agreement. The corrected data plots of lift and drag are shown in Figure 52. Good agreement is shown for lift coefficient in Figure 52, but it is noted the wind tunnel data has a slight increase in C_L around 3 degrees and stays at a

slightly higher level than the computational data. Drag coefficient figures compare very well up to about 7 degrees where the experimental values start to depart from the computational predictions.

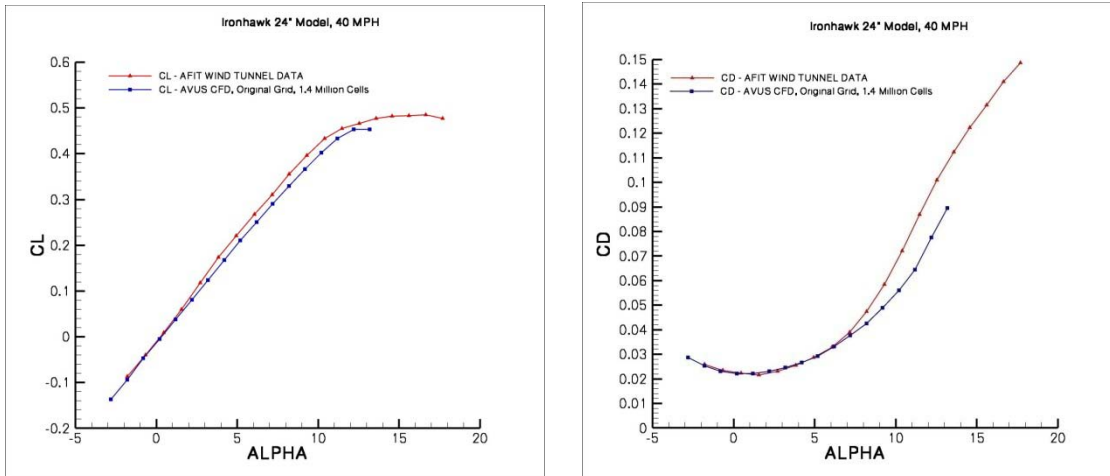


Figure 52: Updated Test Data with Angle of Attack Correction

AFRL/RBAC experimented with an unproven grid adaptation code called CRISP to try and improve the predictions. While grid adaption partially helped close the gap between drag predictions for experiment and computation at high angles of attack, results were not consistent across the entire angle of attack range and successive refinements tended to worsen grid quality resulting in unstable solutions. Grid adaption also significantly degraded max L/D prediction primarily due to no predicted increase in lift. While there is indication that a finer grid may be in order, it also leads us to suspect there is may be something else happening that is not being accounted for with the experimental model. Considering the material the model is made from, perhaps the model is deforming under load or maybe the wings are twisting to a slightly higher angle of attack than the rest of the model. If this is the case, the CFD model no longer accurately represents the model tested in the wind tunnel over the entire angle of attack range. Lift to drag ratio comparisons for experimental versus computational data, shown in Figure 53, show that the computations provided a reasonable prediction for maximum L/D, but did not follow the experimental curve precisely. Figure 54 shows both experimental and computational data for the pitching moment of the vehicle is stable, but there is a difference in the predicted trim angle (the point where the data crosses the x-axis).

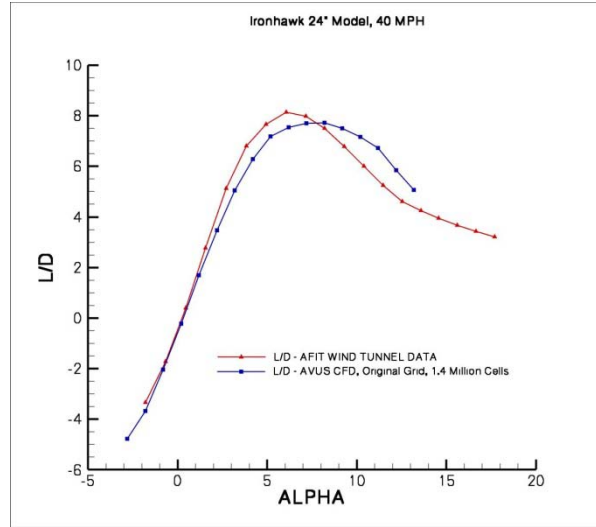


Figure 53: Comparison of L/D vs. AOA Results

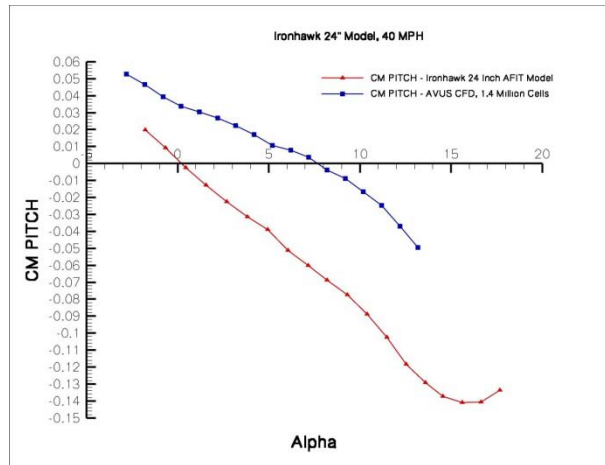


Figure 54: Comparison of Pitching Moment vs. AOA

Below, velocity vectors are displayed on a cutting plane midway through the span of the model with pressure coefficient displayed on the model surfaces. Although multiple cutting planes are not shown, these mid-span cutting planes are representative of the flow across most of the span of the model. Figure 55 represents a fairly typical flow field representative for angles of attack up to about 8.2 degrees with nothing remarkable to note. Streamline traces are depicted in Figure 56 and Figure 57 for 5.2 and 13.2 degrees angle of attack, respectively, in attempt to capture the wingtip vortex. Detecting the presence of any vortex on this configuration was

difficult; however, the streamline traces indicate that the vortices from the upper and lower wing have rolled up into just one vortex.

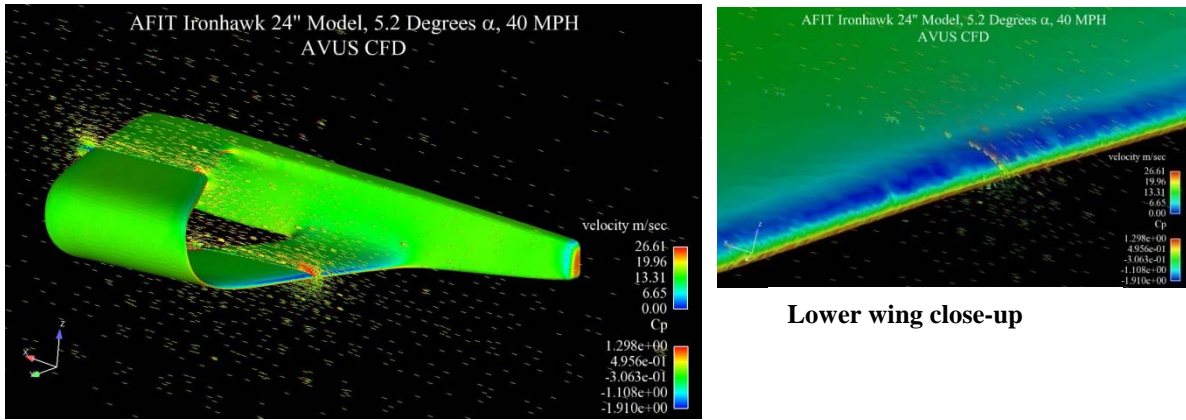


Figure 55: Velocity Vectors at Mid-span for 5.2° AOA

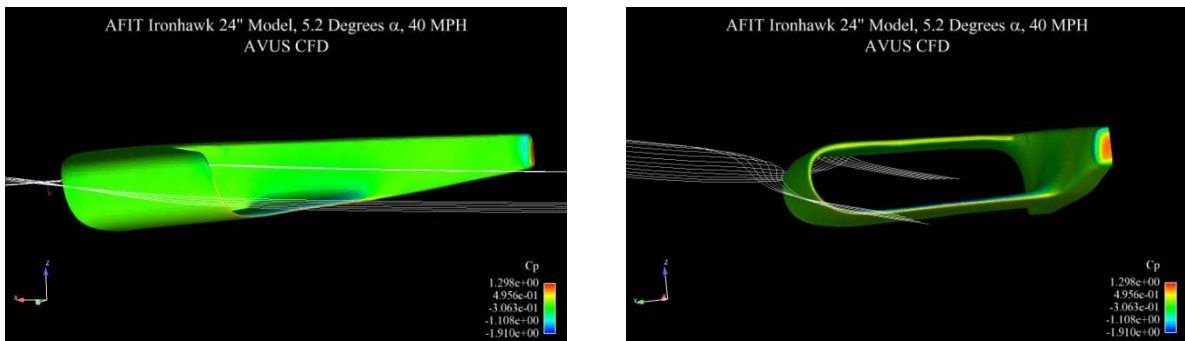


Figure 56: Streamline Traces at 5.2° AOA

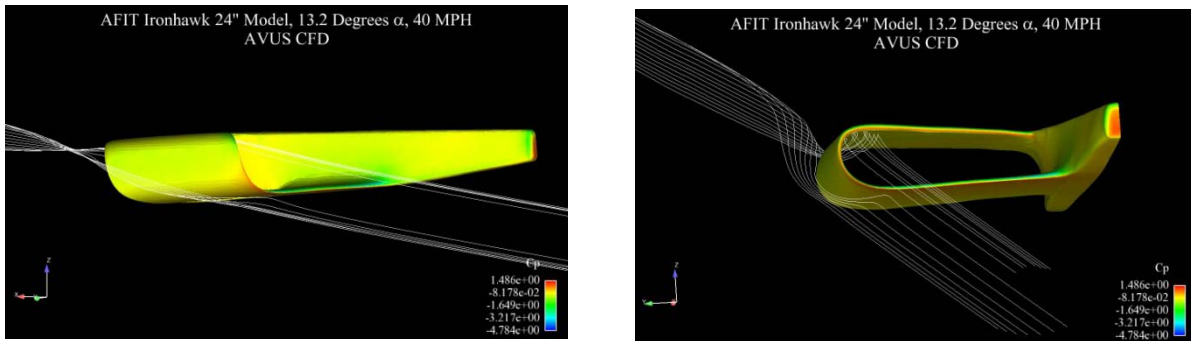


Figure 57: Streamline Traces at 13.2° AOA

Starting at 10.2 degrees flow separation is noted to start on the lower wing. Figure 58 - Figure 61 depict an ever increasing separation bubble on the lower wing as angle of attack increases. In all the angle of attack cases run, no separation was seen on upper wing. A possible explanation for this is that the separation bubble on the lower wing has altered the flow field so that the local angle of attack experienced by the upper wing is at a lower angle of attack than the original freestream.

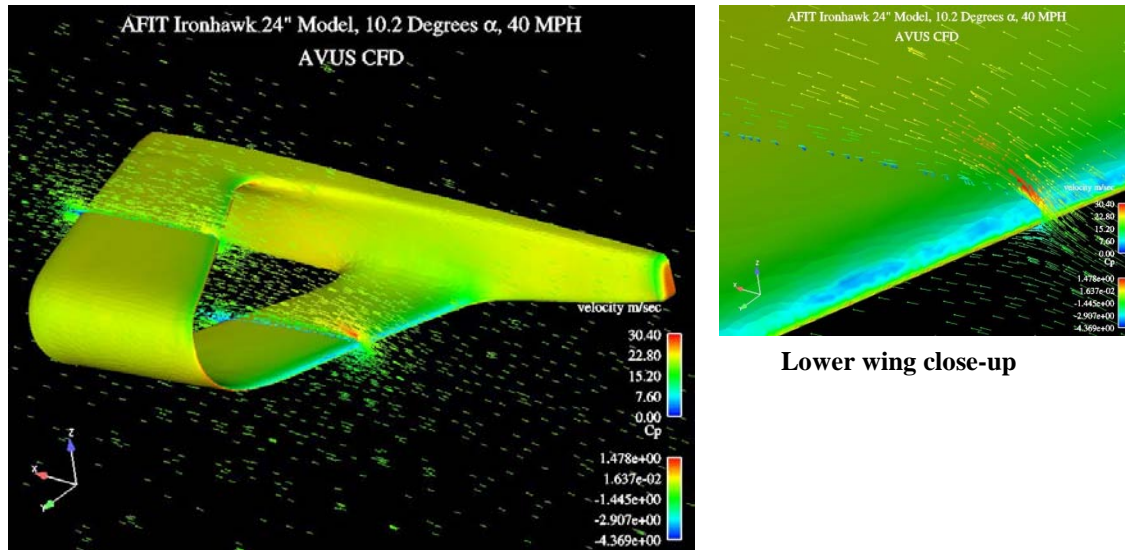


Figure 58: Velocity Vectors at Mid-span for 10.2° AOA

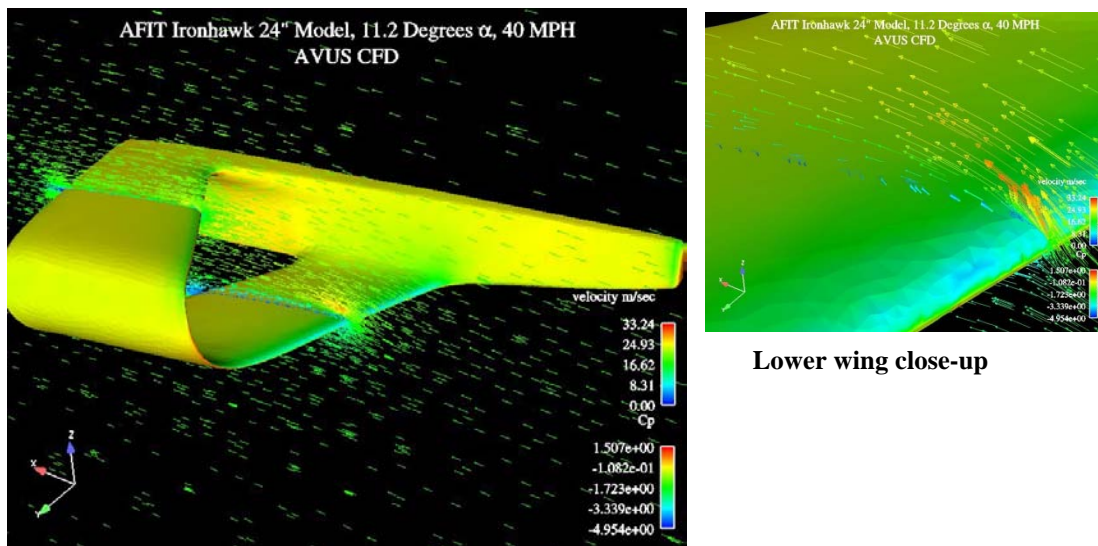
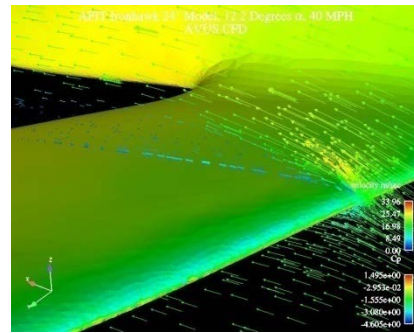
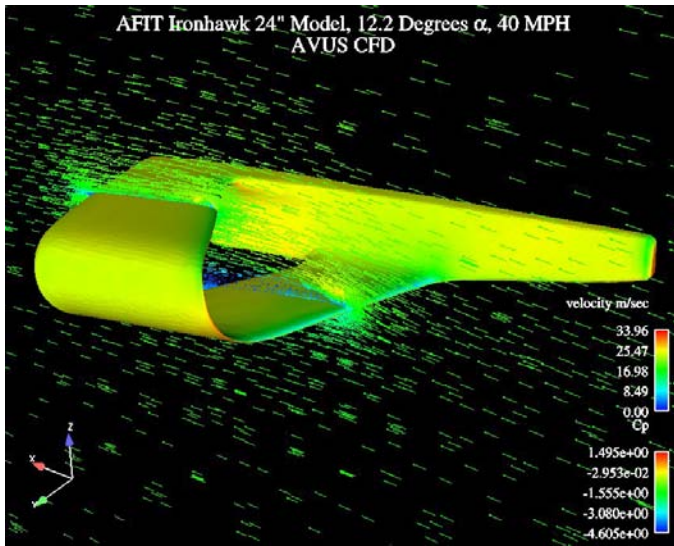
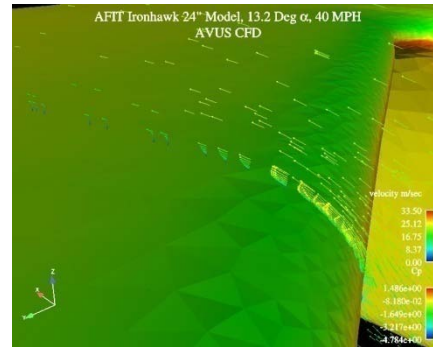
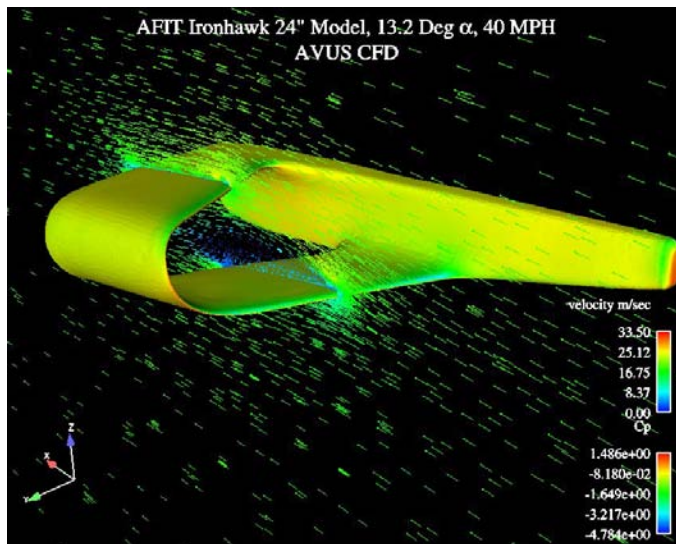


Figure 59: Velocity Vectors at Mid-span for 11.2° AOA

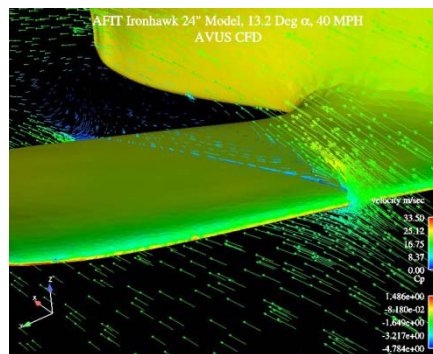


Lower wing close-up

Figure 60: Velocity Vectors at Mid-span for 12.2° AOA



Upper wing close-up



Lower wing close-up

Figure 61: Velocity Vectors at Mid-span for 13.2° AOA

2.5 Results

There are two primary results from Phase II of the Houck Design Program.

1. The CAD modeling rebuild process used in Phase II resulted in a suitable model for CFD analysis. This approach has been proven to be an effective precursor to the aerodynamic analysis and will continue to be employed in all future phases of the Houck program.
2. The CFD results match the experimental data very well for the expected AOA range. The differences between CFD results and experimental data at high AOA values may be due to model deformation under load during testing or insufficient grid resolution on portions of the CFD model (or both).

2.6

Conclusions

There are three conclusions from Phase II of the Houck Design Program.

1. Based on experimental results obtained to date alone and backed up with CFD analysis, there appears to be no significant advantage to using this type of configuration as opposed to a more conventional shape.
2. While it would have been desirable to see a better correlation of experiment and CFD results throughout the angle of attack range it was not possible to produce a finer mesh without creating more complications. CFD grid resolution is closely tied to surface grid resolution, but CAD model imperfections hampered further refinement. Increasing surface resolution would have modeled undesirable geometry details compounded with grid quality issues affecting solution stability and accuracy.
3. It is not clear if model deformation in the wind tunnel may account for some of the discrepancies between CFD and computational results observed at higher angles of attack.

3 Phase III & IV: Design Activities for the Preferred System Concept

Phases III and IV of the Unique Stealth Unmanned Aerial Vehicle (UAV) Houck Aircraft Design Program focused on continued aerodynamic controls research, design iteration to determine a Preferred System Concept (PSC) and a mission profile investigation. Specifically, Phase III efforts concentrated on understanding the flow physics of the Houck UAV configuration, while Phase IV efforts concentrated on applying those physics to create a vehicle useful to a feasible United States Air Force (USAF) mission.

Based on an iterative process including mission analysis, aerodynamic analysis, and structural analysis a PSC has been determined. This design will become the basis for future prototype and flight testing efforts. This section documents the work performed during both Phases III and IV, the results obtained from the work, and the recommendations for the final phase of the program.

The Phase III work concentrated on continued research and analysis of the Houck concept, in particular the aerodynamics of vehicle stability and the wingtip flow guides. The Phase IV work concentrated on determining a Primary System Concept (PSC) and identifying one or more missions for evaluation.

Beginning with five possible mission scenarios, some basic aircraft design principles were used to create a mission-focused design. Initial aerodynamic analysis indicated potential control issues prompting several design iterations. Structural analysis tools were also used to drive the design to a PSC. The primary result of Phases III and IV is a documented PSC. This PSC includes the airfoil, fuselage, and powerplant. The primary conclusion of Phases III and IV is that it is possible to create a vehicle based on the Houck UAV concept that is theoretically capable of flight.

3.1 Introduction

This report details the effort during Phases III and IV of the Unique Stealth UAV Houck Aircraft Design Program. The purpose of these phases of the program was to employ theoretical analysis to better understand the aerodynamics of the Houck airfoil concept and to iterate the concept in

order to produce a mission-capable Preferred System Concept. This report discusses the program history, mission analysis, configuration data, aerodynamic modeling, structural analysis, results and conclusions of Phases III and IV. It closes with recommended next steps for work in Phase V.

Phases III and IV are less conceptual than the earlier phases and focus on the analysis of a Preferred System Concept which has been designed based on identified potential USAF missions. This concept also includes a propulsion system and a payload.

Principal Phase III and IV participants of the collaborative team were IHE (model development), UDRI (mission analysis, documentation), and SES (structural analysis, aerodynamic controls analysis, mission analysis, vehicle design iterations).

Deliverables for Phases III and IV are:

1. Written documentation
2. List of potential missions
3. CAD, FEA, CFD models

3.2 Mission Analysis

The mission analysis effort was initiated as a brainstorming activity among a group of Houck team members with a variety of engineering experiences. After much discussion and consolidation of ideas, the following five potential mission profiles were identified: local surveillance, targeted surveillance, widespread surveillance, stealth observation, and local surveillance with larger payload. Table 7 provides additional information regarding each of the mission profiles.

Table 7: Potential Mission Profile Descriptions

Mission #	Mission Description	Example Mission	Vehicle Requirements
1	Local Surveillance	Defensive perimeter survey of forward operating base	Short range, medium loiter time
2	Targeted Surveillance	Intelligence update of known enemy location	Accurate navigation, maximum range, short-term telemetry
3	Widespread Surveillance	On-going survey of enemy movements and construction	Maximum loiter time, continuous telemetry
4	Stealth Observation	Monitor suspected enemy gatherings	Quiet operation, high altitude, medium range, high loiter time
5	Local Surveillance with Larger Payload	Defensive perimeter survey of forward operating base with advanced sensors	High payload, short distance, medium loiter time

Subsequent to this mission identification, initial aircraft sizing calculations were performed. These calculations were performed using airplane design methods for commercial and military aircraft¹⁴. These design methods are based on historical data for existing airplanes and use correlations between mission requirements and airframe sizing. It is believed that the extrapolation of these methods to small UAV design leads to an over-prediction of the empty airplane weight estimates. Once the initial values were determined, first principle calculations were used to further evolve the design. A summary of the results of the initial sizing per mission is found in Table 8. For complete data tables see

Appendix B.

Table 8: Summary of Mission and Airplane Sizes

	Mission 1	Mission 2	Mission 3	Mission 4	Mission 5
Payload (lbs)	4	4	4	4	10
Range (mi)	2	10	10	20	2
Loiter (hrs)	3	0.166 (10 mins)	3	0.33 (20 mins)	3
Altitude (ft)	1000	1000	2000	2000	1000
Cruise or loiter speed (mph)	60	60	60	60	60
Stall speed (mph)	32	32	32	32	32
Weight at take off (lbs)	9	8.5	9	8.5	23.6
Wt of fuel (lbs)	0.53	0.22	0.54	0.25	1.4
Wing area (ft²)	3	2.8	3.1	2.9	7.9
Wing loading (lb/ft²)	3	3	2.9	2.9	3
Power at takeoff (hp)	0.4 (300W)	0.38 (285W)	0.39 (293W)	0.37 (278W)	1.06 (795W)
Power at cruise (hp)	0.13 (98W)	0.12 (90W)	0.13 (98W)	0.12 (90W)	0.34 (255W)
Power loading (W/P)	22	22	23	23	22

3.3 Configuration Data

The initial aircraft sizing performed as part of the mission analysis effort resulted in an interesting result. It was determined that four of the five missions could simultaneously be satisfied with one aircraft configuration. The other mission (Stealth Observation) presents some unique requirements resulting in unique required aircraft features. Based on this determination,

it was decided to pursue a robust configuration which would be capable of simultaneously meeting the following missions: local surveillance, targeted surveillance, widespread surveillance, and local surveillance with larger payload.

The determination of a final configuration for the Preferred System Concept (PSC) and prototype build was an iterative process. Both aerodynamic and structural analyses were used to evaluate the interim designs and provide direction for improvements. Appendix C is a collection of some of the interim designs that were considered and evaluated during the course of Phases III and IV of the Houck program. Design elements and characteristics that impacted the final configuration include: pitch trim, location of lifting surfaces, area of control surfaces, angle of incidence of both the front and back wings, and Center of Gravity (CG) location. Early in the analysis it became clear that the original concept had a strong nose-down moment which could not be counteracted simply by moving the CG. Several options for trimming the aircraft were suggested. Figure 62 illustrates four options that were considered by the design team. It was determined that Option III was the best overall fit for the program and work proceeded down this path.

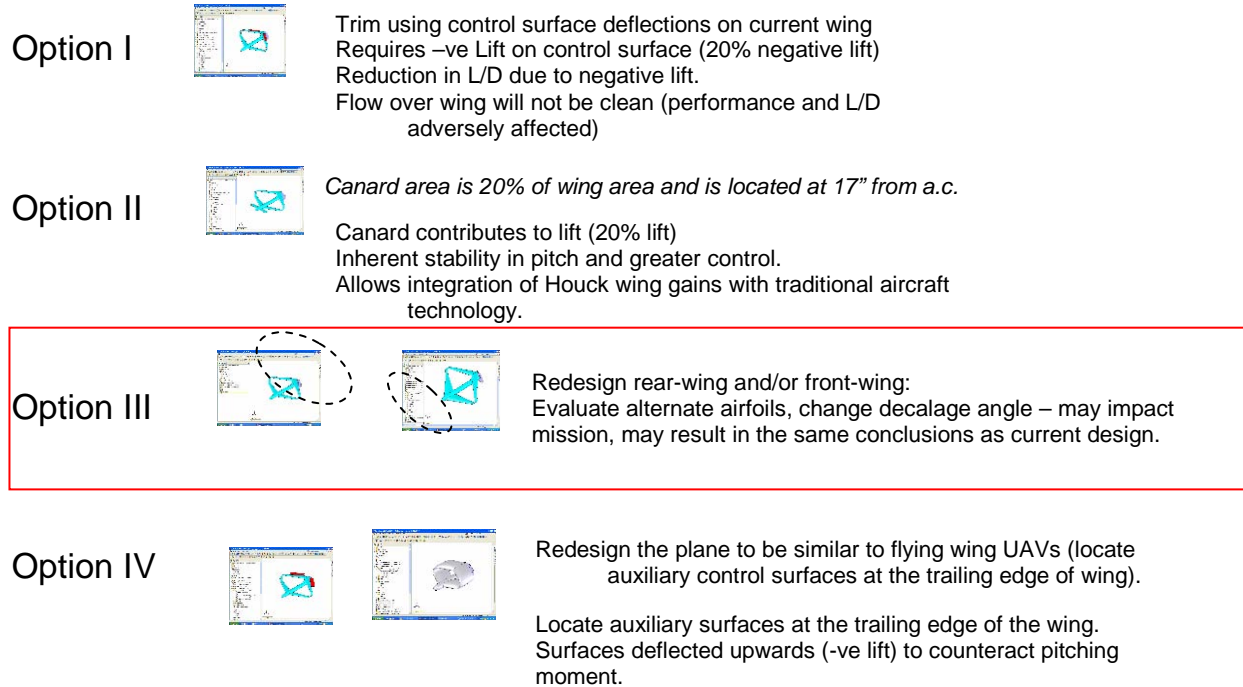


Figure 62: Four Options for Trimming the Aircraft

Figure 63 illustrates the resulting PSC configuration. This configuration includes the upper and lower set of wings joined at the two wingtips by curved flow guides per the Houck concept.

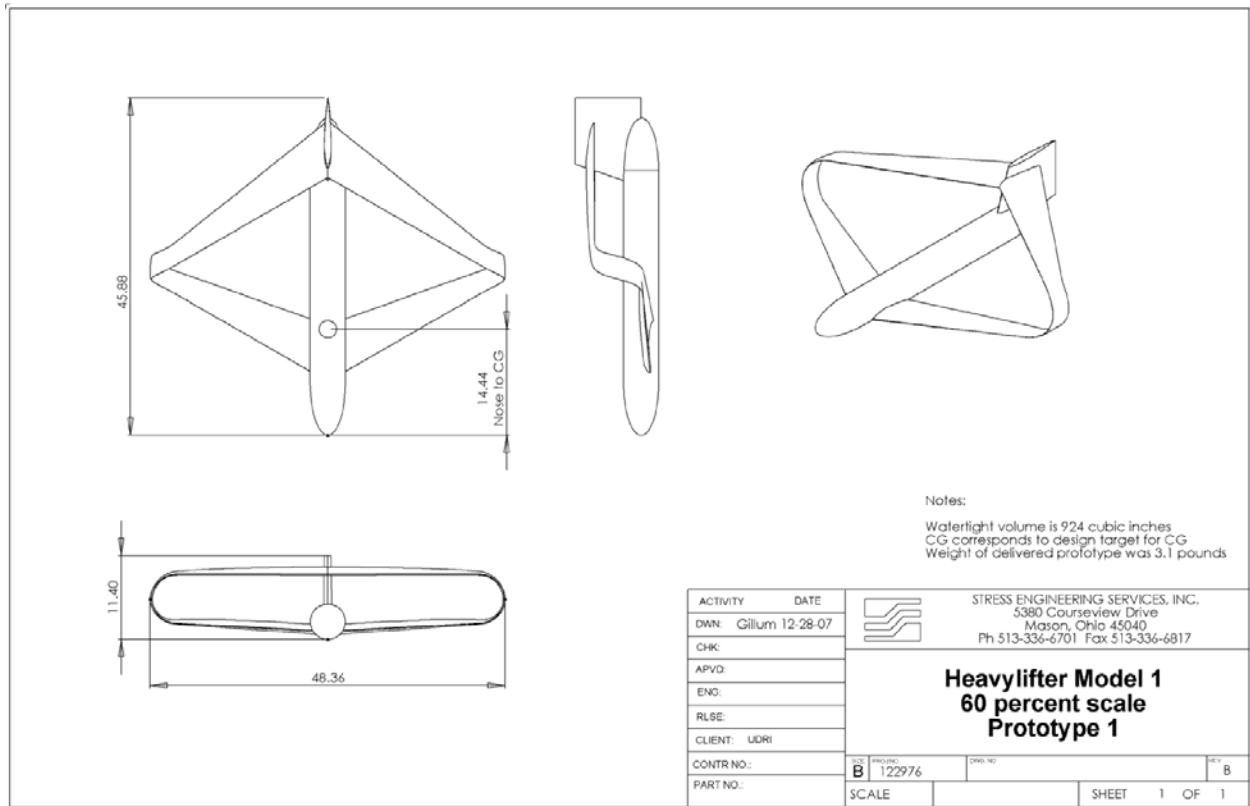


Figure 63: Preferred System Concept Configuration

The PSC includes an electric propulsion system. The assessment of a gas powered versus an electric powered aircraft is shown in Figure 64.

Propulsion	
<i>Gas Powered</i>	<i>Electric</i>
Engine (1 hp engine, 1 lb weight)	Electric motor (2" dia, 2.4"length, .8 lb)
Propeller 10"	Propeller 11"
Fuel: 0.4 lb (3 hrs duration)	Battery (2.5 lb, 2 hr, 2.4"x1.8"x7.5")
Weight of propulsion system ~ 1.5 lbs	Weight of propulsion system ~ 3.3 lbs
Noisy	Quieter
Battery needed for controller	Additional battery not required

Figure 64: Gas vs. Electric Propulsion System

3.4 Aerodynamic Analysis

Aerodynamic analysis played a large role in the configuration iterations discussed in the previous sections. It was via aerodynamic analysis that the pitch control issues were identified and the trim options were assessed. The full aircraft aerodynamic analysis performed using FLUENT CFD software on an interim configuration provided the final adjustments in the determination of the PSC.

The design team also considered the use of VSAERO software for aerodynamic analysis. VSAERO uses a panel method algorithm (versus the Navier-Stokes approach employed by FLUENT). The main advantage to using VSAERO would be its superior solution speed which would allow the team to rapidly assess a wide variety of geometries and flow scenarios. As shown in Figure 65, comparative analysis revealed that VSAERO and FLUENT produced very similar results for drag analysis and somewhat similar results for lift analysis.

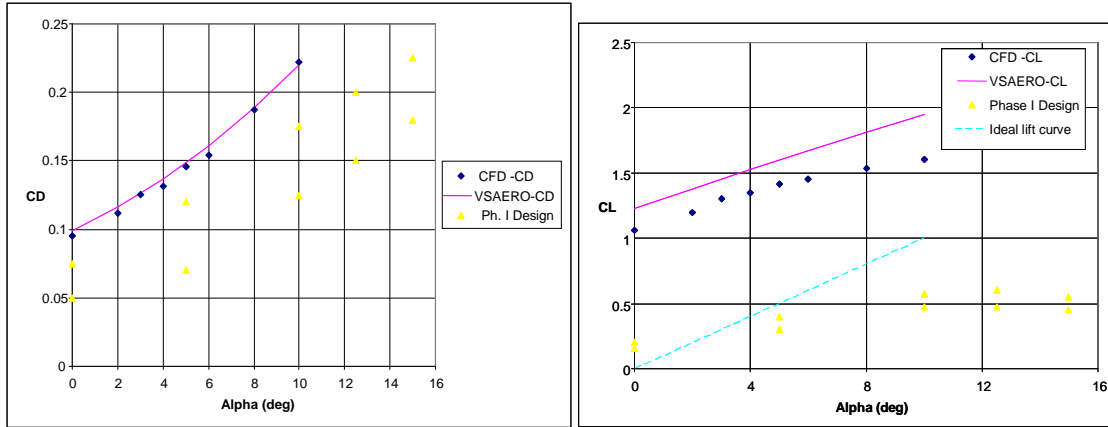


Figure 65: Comparative Analysis of VSAERO vs. FLUENT Analysis

A deficiency for VSAERO in this particular application is its inability to analyze conditions of separated flow. The Houck configuration produces a condition of separated flow. In addition, although VSAERO does possess superior speed capabilities, the Houck design team infrastructure includes IGES geometry inputs for FLUENT and parallel processing which negates the speed advantage. For these reasons, FLUENT CFD analysis became the primary mode of aerodynamic analysis. Appendix D contains an internal team document which outlines the comparative analysis of the two software programs.

FLUENT CFD analysis was completed to predict overall performance (lift and drag) and three measures of stability. Figure 66 and Figure 67 illustrate the lift and drag performance, respectively of the PSC. For this analysis, cruise power was 210 W (0.28 Hp). The L/D value was determined to be 9.8. For a theoretical discussion of L/D_{\max} for the Houck concept, see Appendix E.

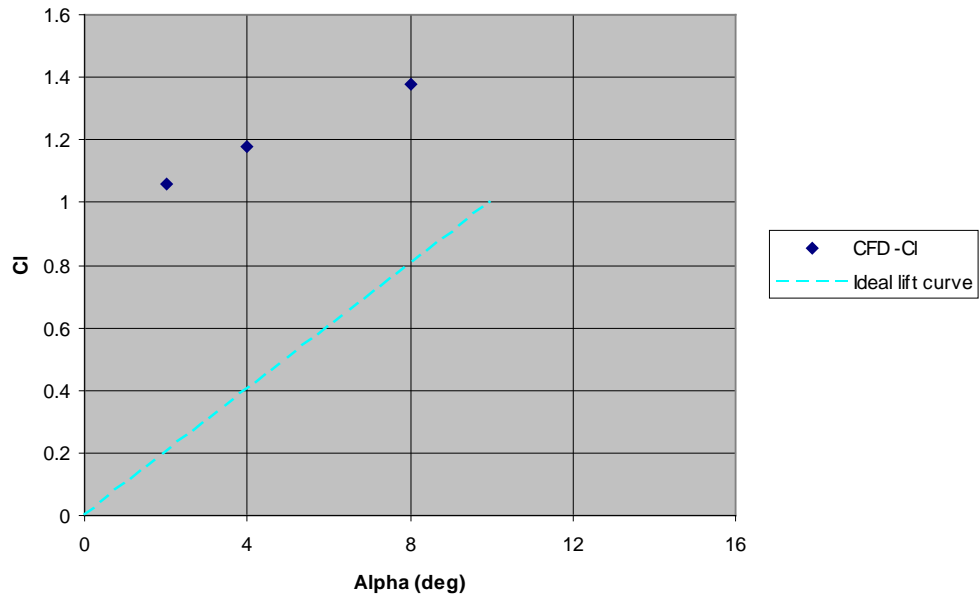


Figure 66: Predicted Lift Performance of the Preferred System Concept

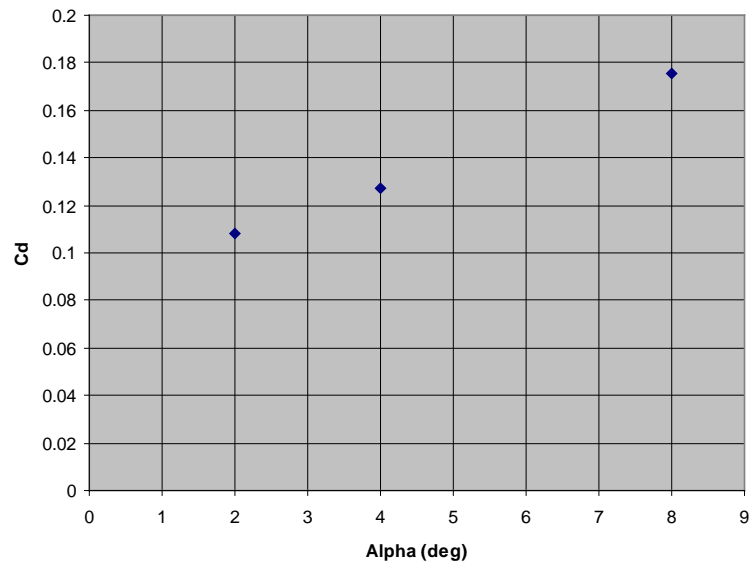


Figure 67: Predicted Drag Performance of the Preferred System Concept

The three types of stability tested include longitudinal stability, directional stability, and roll stability. The longitudinal stability analysis included an Angle of Attack (AOA) that ranged from zero to ten degrees. Figure 68 and Figure 69 illustrate the results.

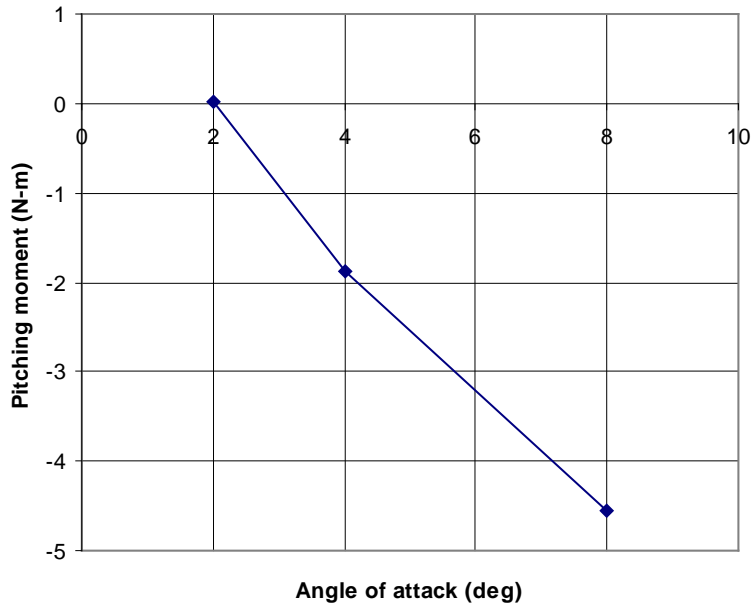


Figure 68: Pitching Moment vs. AOA

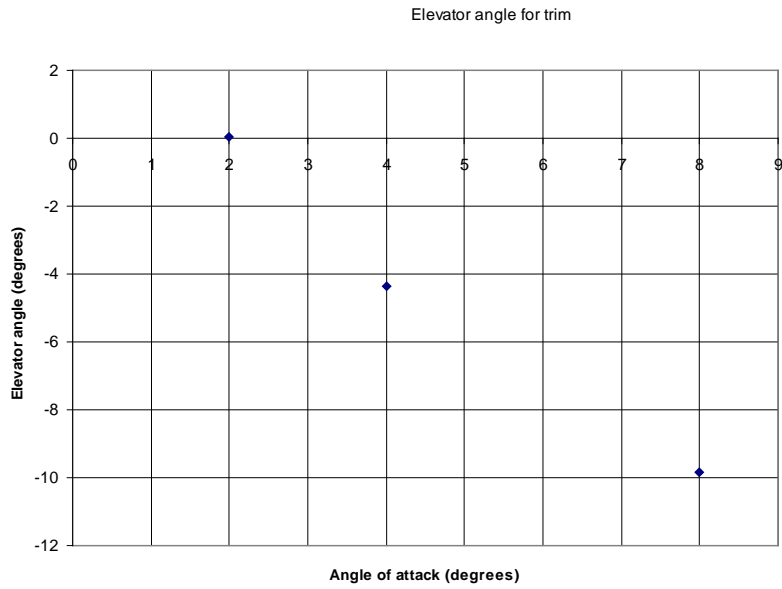


Figure 69: Elevator Angle for Trim

As discussed in the previous section, pitch control is a concern. In order to improve longitudinal stability, the aircraft Center of Gravity (CG) can be modified. Figure 70 depicts the most forward, most aft, and suggested CG locations.

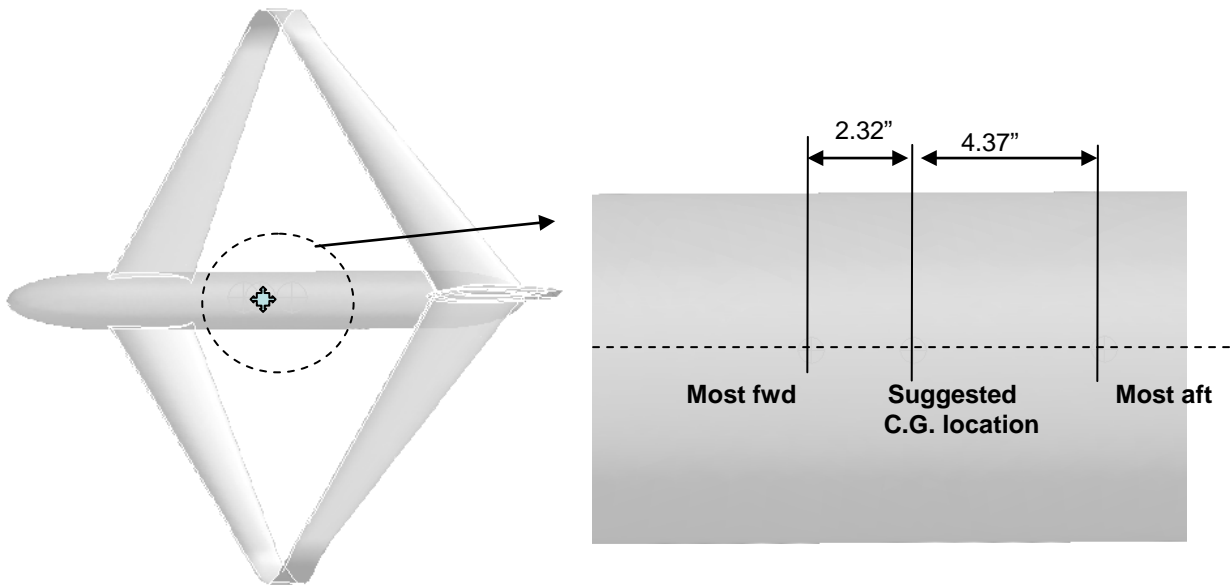


Figure 70: Various Center of Gravity Locations

At the most aft CG the airplane is neutrally stable. Placing the CG at a location aft of this point will result in an unstable airplane. The most forward CG location is determined based on the available elevator power to trim the airplane. Placing the CG forward of this location will result in a configuration that will be untrimmable using the designed elevators. The suggested CG location is the location that provides stability in pitch and allows the plane to maintain level flight at two degrees angle of attack (note: L/D is maximum at two degrees angle of attack).

The allowable CG travel is 6.7", however, deviations in CG location from the suggested position will result in a level flight angle other than two degrees and/or nonzero elevator deflections at level flight conditions. The static margin of this configuration is -0.45. The recommended margin for *conventional* aircraft is -0.1. The increased static margin will likely result in a slightly sluggish response in pitch but should produce a stable configuration for this unconventional aircraft. The static margin may be changed (reduced) depending on the feel from the initial flight testing. A high degree of maneuverability is not required for the defined

missions so an increased margin of stability is acceptable. It is therefore recommended that the PSC be designed to allow for twenty degrees of elevator deflection.

Figure 71 illustrates the results of the directional stability analysis.

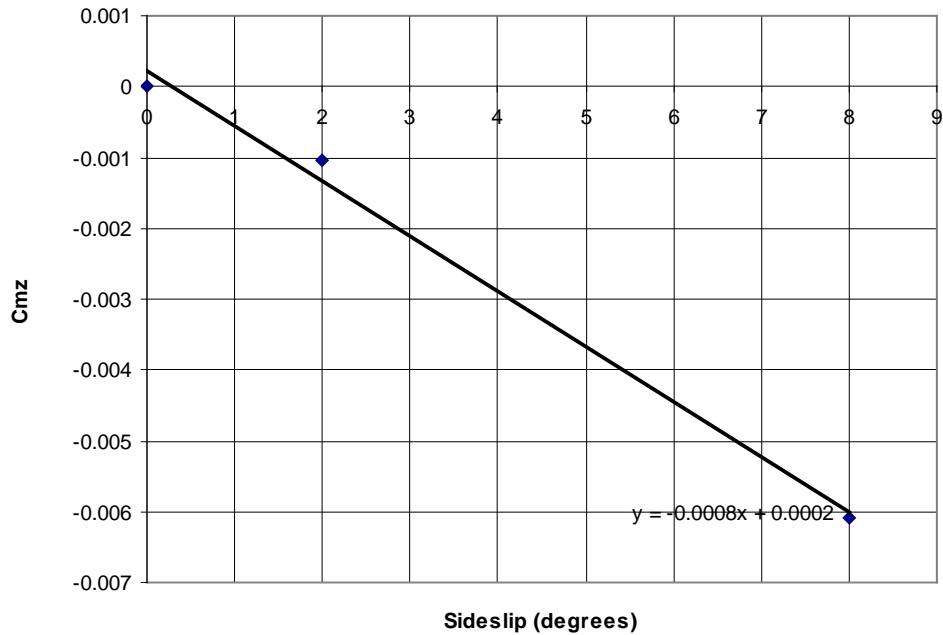


Figure 71: Directional Stability Analysis

The net stability margin is 0.00047 (versus a recommended minimum of 0.0005). To improve directional stability, it is recommended that the vertical tail wetted area be increased by 20%. This recommendation was incorporated into the PSC.

Figure 72 illustrates the results of the roll stability analysis.

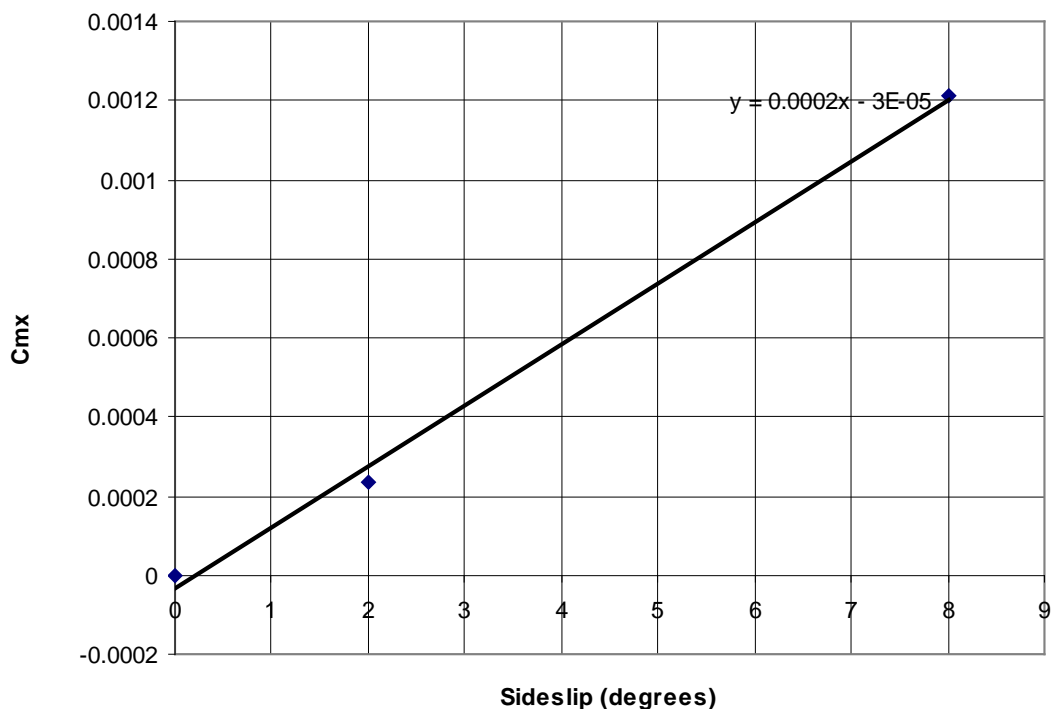


Figure 72: Roll Stability Analysis

The stability margin is 0.0002 (versus a recommended minimum of 0.00025). To improve roll stability it is recommended that the dihedral be increased to three degrees on the front wing and that the dihedral be set to zero degrees on the rear wing. These recommendations were incorporated into the PSC.

3.5 Structural Analysis

Although a final material and configuration have not been determined, a preliminary structural analysis was performed in order to establish the feasibility of the structure. It is assumed that an injection-molded fiber reinforced plastic will serve the USAF needs if the Houck concept reaches a mass production stage. For the structural analysis, the assumed material was glass filled Vectra. Table 9 contains the material properties that were assumed in the analysis.

Table 9: Properties of Glass filled Vectra

	Glass filled Vectra
Cost/lb	\$15 to \$20
Flex Modulus (mpa)	12000
Flex Modulus (Msi)	1,740
Flex Yield (mpa)	240
Flex Yield (psi)	34,800
Elongation at break	3.3%
Density (g/cc)	1.5
Density (lb/cuin)	0.0542
Min wall thickness (in)	0.01

The assumed cruise conditions for the structural analysis are a steady pressure applied normal to the direction of travel. Figure 73 is a stress plot created using ABAQUS Finite Element Analysis (FEA) software.

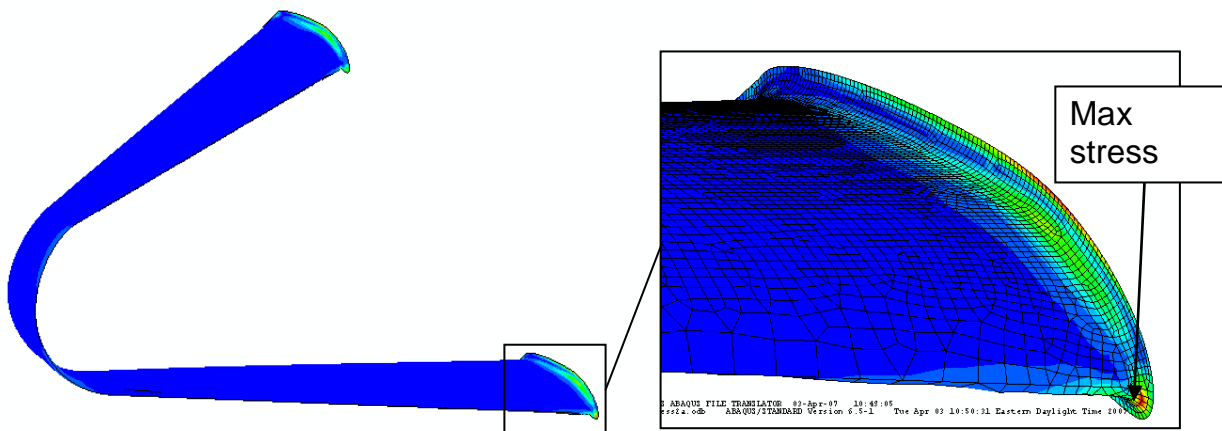


Figure 73: Stress Plot of Houck Wing Using ABAQUS

The wing is very strong due to the joined-wing effect at the tip. The bending moment at the root is only 2/3 that of a traditional cantilever wing. Using a hollow wing section made from fiber reinforced plastic with a wall section of 0.015” allows a factor of safety of 3 on cruising wing load at the root. Wingtip Factor of Safety (FOS) is greater than 20, center span greater than 100. Figure 74 is a deflection plot created using ABAQUS FEA software.

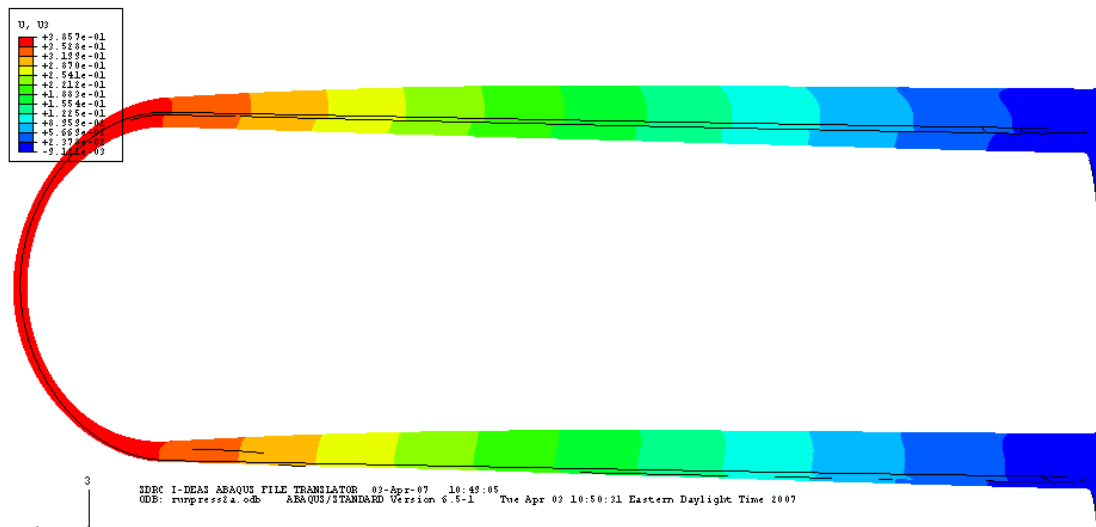


Figure 74: Deflection Plot of Houck Wing Using ABAQUS

The wing is very stiff due to the joined wing effect at the tip. The tip deflection is only 1/3 that of a traditional cantilever wing. Using a hollow wing section made from fiber reinforced plastic with a wall section of 0.015” allows a tip deflection of 3/8” on cruising wing loads.

The preliminary structural analysis provided results within initial estimates. Specifically, the analysis resulted in the following findings.

- The airframe can be made extremely light due to a combination of its small size and the joined wing.
- The material chosen can be molded to a wall thickness of less than 0.015” with detailed features available at a resolution of approximately 0.001”

- Using a completely hollow body, 0.015” thick will produce an airframe that weighs 17 ounces. Adding in control surfaces and structures, mounts for the payload, etc. will increase this weight.
- Assuming the controls surfaces and structures can be added in at an additional 8 ounces, the total weight of the empty plane including the propulsion system will be 4.9 pounds.

3.6 Results

This section provides a summary of the four most significant results from Phase III and Phase IV.

- A single PSC can be developed which simultaneously meets the mission objective for four of the five mission profiles developed for the program.
- While both VSAERO and FLUENT software provide accurate data for aerodynamic analysis, FLUENT software is a better option for Houck analysis due to the flow separation inherent in the design and the well-established CAD infrastructure of the design team.
- The earlier Houck concepts experienced a significant nose-down pitching moment which can be overcome by design adaptations.
- Structural analysis demonstrates that injection-moulded fiber reinforced plastic is a feasible choice for large production of Houck UAV aircraft.

3.7 Conclusions

The primary conclusion is that a flight-capable aircraft is possible using a Houck configuration. A 9 pound gross weight aircraft has been sized to accomplish several different reconnaissance missions carrying a 4 pound payload. It is estimated that the aircraft can have an endurance of 3 hours at low altitudes over low mission radii. The PSC aircraft has a length and wingspan of around 80 inches and incorporates the characteristic Houck flow guide wing tips. The aircraft has been designed to be stable in all three axes to offer good flying qualities.

4 Phase V: Fabrication of Flying Prototype Aircraft

4.1 Summary

This section provides documentation of the University of Dayton Research Institute efforts during Phase V of the program. During this phase, the preferred design from Phase IV was produced as a 60% scale radio-controlled prototype aircraft. The physical prototype was delivered to the Air Force Research Laboratory on September 5, 2007. This report documents the build notes, aircraft components, and recommendations from this effort. It also includes appendices consisting of presentations given at a Houck Airfoil Design Team meeting. Appendix F is focused on the design of the prototype aircraft and early construction phase. Appendix G is focused on the prototype construction methodology.

Phase V resulted in the delivery of the first functional prototype aircraft using the Houck wingtip configuration. The prototype UAV produced in Phase V consisted of airframe, radio control actuators, control surfaces, and a propulsion system. These systems distinguish this prototype from hardware produced in previous phases of the program. In the earlier phases, the vehicles did not include controls or propulsion. The prototype design is commonly known on the Houck Design Team as “Heavyliifter design Rev 1.” This design was developed through extensive CFD work performed during Phase IV of the program.

Details and drawings of this design are included in Appendix F. The full size Heavyliifter was designed to fly with a gross takeoff weight of 25 pounds and a cruising speed of 25 miles per hour. At 60% scale the gross weight is nine pounds. As delivered, the prototype empty weight was 3.1 pounds. This difference in weight is due to absence of payload, small battery, and undersized motor, all of which are appropriate for initial flight testing. Figure 75 and Figure 76 are photographs of the completed prototype aircraft.

The Build Notes provided serve to assist future prototype efforts. Also included in this report is a list of UAV Components. Experience from the build has been captured in a Recommendations section for future builds. Appendix G provides an overview of the prototype construction

methodology. Although the prototype has been designed and built as an airworthy product, logistical issues prevented any test flight activity as part of this phase of the program. The physical prototype delivered includes all required elements for future flight testing.

4.2 Build Notes

The following build notes serve as documentation for the Houck UAV prototype production. Figure 75 and Figure 76 are photographs of the Houck UAV prototype.



Figure 75: Houck UAV Prototype



Figure 76: Alternate View of Houck UAV Prototype

1. The foam parts were cut on a 4-axis CNC machine. The wing core profiles are over corrected for kerf and under corrected for surface sheeting, resulting in a slightly larger trailing edge length and thickness than desired.
2. The wing tip SLA's are made to the correct dimensions which highlights the kerf error previously mentioned.
3. Final weight and balancing has NOT been performed. The vehicle is slightly tail heavy and will require weights in the nose. The recommended weight placement is on the inside curve of the nose cone under the motor. There is a hook on the dorsal surface of the fuselage. This hook is located at the target CG for the vehicle and should be used to aid in final balance.
4. There are control surfaces on the front and rear wing as well as a traditional rudder for yaw control. The primary flight controls surfaces are set up on the rear wing like a delta wing using elevons. Additional control surfaces on the front wing act as ailerons, flaps or flaperons depending on switch selection of the transmitter. Additional control authority can be added by using mixing switches on the transmitter. The bottom right switch adds additional roll control using the front wing surfaces as ailerons; the bottom left switch adds additional pitch control using the front wing surfaces as flaps mixed to the elevator control. If maximum control authority is needed, then both switches are activated and the front surfaces are used as flaperons and mixed to the rear wing accordingly. The test pilot should familiarize himself with these switch settings before the first flight.
5. Round wing tips are replaceable with the flat end connection. The vehicle was delivered in this configuration. This strategy is suggested to protect the rounded tips from damage during the first flight tests. Consideration should be given to making urethane moulds from the wingtips to make inexpensive replacement wingtips, depending on flight testing planned.
6. Gross weight flights with self propelled climbs will need a motor of least 175-200W. The climb rate will be about 100-150fpm. The aircraft will be very heavily loaded so hand launching is not recommended as it will not reach the required flight speed by hand.

7. The RC control servos are permanently attached. Removal or replacement of the servos will require repair to the foam core of the wing. Servo leads were placed after wing attachment and should be clipped at the servo if replacement is required.
8. Based on experience with a different fully aerobatic model with a slightly larger motor and similar weight and speed to the Houck UAV, the battery life of the Houck UAV prototype is expected to be approximately 20 minutes. The UAV will be flying at a relatively low speed and mostly loitering, so the power setting will be about 40% or somewhat less to maintain constant altitude at the current weight.
9. Based purely on calculations and assuming the battery is only subjected to the maximum recommended discharge of 80% of full capacity (i.e. 2100 milliAmp-hours * 0.8 = 1680 milliAmp-hours) the following run times can be estimated for average power setting:
 - i. Full power 9 Amps > 187 seconds (3 minutes)
 - ii. 75% power 6.75 Amps > 249 seconds (4.2 minutes)
 - iii. 60% power 5.4 Amps > 311 seconds (5.2 minutes)
 - iv. 40% power 4.5 Amps > 373 seconds (6.2 minutes)
 - v. 30% Power 3 Amps > 560 seconds (9.3 minutes)
10. Fully discharging the battery will result in fewer recharge cycles of the battery, but will add 20% to all of the above times.

4.3 UAV Components

The Houck UAV prototype was produced using the following components.

Electrical and Controls:

- Motor: E-Flite Park 450 Outrunner
- Electronic Speed Controller: E-Flite 20A Speed Controller
- Main Battery: Thunder Power Pro-Lite Series 2100mAh
- RC Transmitter & Rcvr: Spektrum DX7 7 channels (2.4GHz Spread Spektrum Band)
- Servos: Hitec HS-55 (quantity 5)
- Servo lead extensions: Front wing 24" - Rear wing 48"

Propeller:

- 9" diameter, 7" lead, 2 blade

Wings:

- Wing skin 1/64 Birch Plywood 12" x 48"
- Spars made from 1/64 Birch Plywood
- Custom cut foam cores from 2# / cu.ft. Expanded Polystyrene

Wingtips:

- SLA's (laser sintered epoxy) from CAD file.

Main Structure:

- Balsa laminated with 1/64 Birch Plywood

Fuselage:

- Custom cut foam glued to the main structure.

Tail:

- Custom cut foam glued to the main structure.

4.4 Recommendations

The following recommendations are provided to assist in future prototype production efforts.

1. The spars in the wings can probably be left out. This change would reduce the construction effort.
2. The wing cores are cut from 2 lb/ft³ EPS foam. Given the resulting structural rigidity of the first build, SES believes that 1.5 lb/ft³ is more than enough and 1

lb/ft³ foam may be possible. This change would reduce the overall weight of the vehicle.

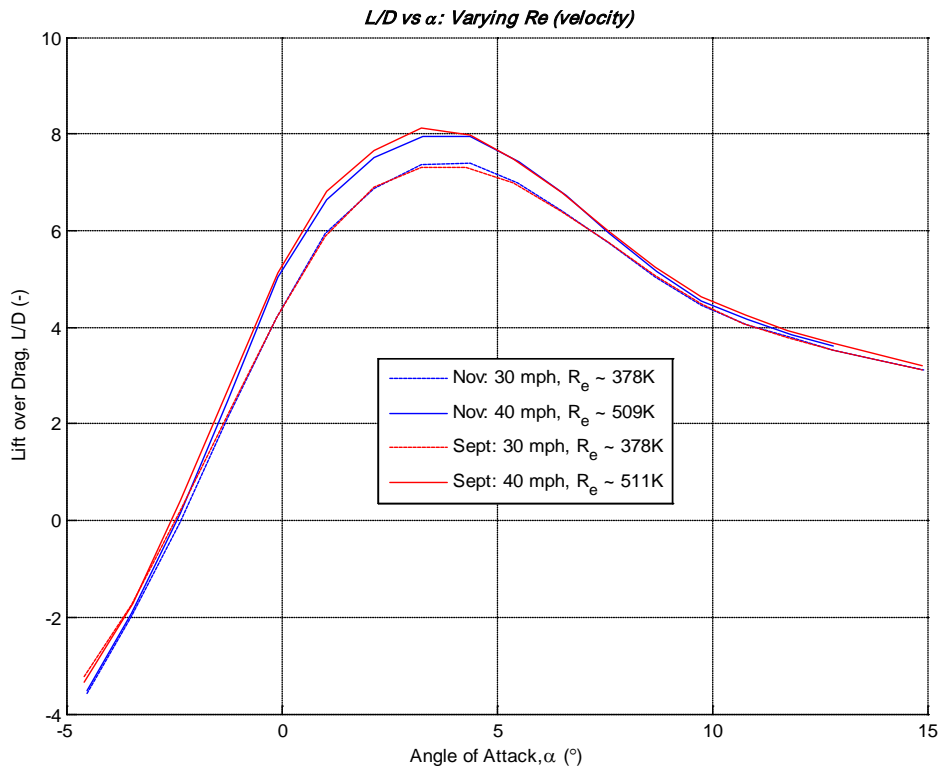
3. Alternate fuselage and motor locations should be considered for weight and durability purposes. For instance, a teardrop camera pod could be placed at the leading edge of the front wing on the vehicle centerline. The motor and prop could be placed on the leading edge of the rear wing on the centerline. The fuselage could consist of only a very small “stick” section connecting the two. This modification would reduce drag, open up visibility to the camera, and protect the propeller from damage.
4. The intent of the first power configuration was not to fly long durations, but to enable the exploration of the airspeed flight envelope. Once the flight envelope is established and the gross weight is increased to the design maximum, the batteries and motor can be added to give longer durations. Final long duration missions with a full size model cannot likely be achieved from a battery powered vehicle.
5. Consideration should be given to changing the wing profile from the Selig1223 to a different wing profile. A less tapered profile would be easier to build than the Selig1223. A profile with a lower moment coefficient might give a larger speed range and be easier to trim than the Selig1223. This design change would require repeating much of the initial CFD analysis to develop a stable wing design.

References

- ¹ Altman, A., “Unique Stealth UAV Houck Aircraft Design Program, Vol. I: Final Report”
- ² Walker, Michael M., 1st Lt., “The Aerodynamic Performance of the 24 Inch Houck Configuration.” MS Thesis. Air Force Institute of Technology. AFIT/GAE/ENY/07-M30, March 2007.
- ³ Killian, Dermot, ENS, “The Aerodynamic Performance of the Houck Configuration Flow Guides.” M.S. Thesis. Air Force Institute of Technology. AFIT /GAE/ENY/07-709, June 2007.
- ⁴ Oligney, B., Frash, M., Yechout, T. “Aerodynamic Evaluation and Optimization of the Houck Joined Wing Aircraft,” AIAA 2008-1422, Jan. 2008.
- ⁵ Stinton, Darrol, The Design of the Aeroplane, Blackwell Science Ltd., 1983.
- ⁶ Grismer, M. J., Strang, W. Z., Tomaro, R. F., and Witzeman, F. C., “Cobalt: A Parallel, Implicit, Unstructured Euler/Navier-Stokes Solver,” Advances in Engineering Software, Vol. 29, No. 3-6, 1998, pp. 365-373.
- ⁷ Strang, W. Z., Tomaro, R. F., and Grismer, M. J., “The Defining Methods of Cobalt60: A Parallel, Implicit, Unstructured Euler/Navier-Stokes Flow Solver,” AIAA Paper 99-0786, Jan. 1999.
- ⁸ Tomaro, R. F., Witzeman, F. C., and Strang, W. Z., “A Solution on the F-18C for Store Separation Simulation Using Cobalt60,” AIAA Paper 99-0122, Jan. 1999.
- ⁹ Wurtzler, K., “An Effectiveness Study of F-15 Forebody Flow Analysis Using Cobalt,” AIAA Paper 99-0536, Jan. 1999.
- ¹⁰ Pirzadeh, S., “Progress Toward a User-Oriented Unstructured Viscous Grid Generator,” AIAA Paper 96-0031, Jan. 1996.
- ¹¹ Pirzadeh, S., “Three-Dimensional Unstructured Viscous Grids by the Advancing-Layers Method,” AIAA Journal, Vol. 34, No. 1, Jan. 1996, pp. 43-49.
- ¹² Torres, Gabriel E., and Mueller, Thomas J., “Aerodynamic Characteristics of Low Aspect Ratio Wings at Low Reynolds Numbers”, Fixed And Flapping Wing Aerodynamics For Micro Air Vehicles Applications. T.J. Mueller, ed., Progress in Aeronautics and Astronautics, Volume 195, AIAA, Chapter 7, pp.115-139, 2001.
- ¹³ Hoerner, S.F., Fluid Dynamic Drag, Hoerner Fluid Dynamics, Brick Town, NJ, pp. 7-16 – 7-21, 1965.
- ¹⁴ Roskam, Jan, Airplane Design, DARcorporation, 1997

Appendix A: AFIT 24" Houck Model Data (Wind Tunnel & Hot Wire Results)

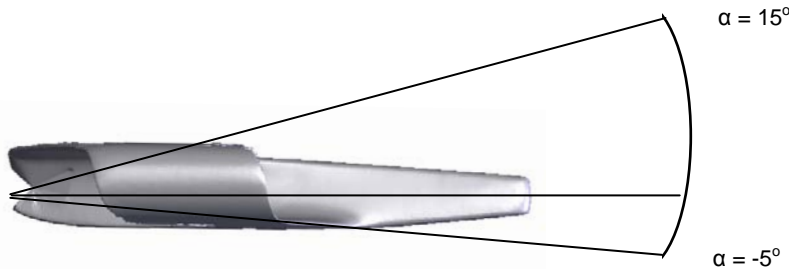
This appendix contains the entire content of a presentation given by Lt. Michael Walker on 22 November 2006. The following pages contain the detailed results of Wind Tunnel and Hot Wire Empirical Testing performed on the Phase II 24" Houck Model.



The lift over drag curve can be seen above. As you can see, the November and September data are very comparable.

Wind Tunnel Comparisons: Houck Configuration – Sept. & Nov. Data

Wind Tunnel data was taken in September of 2006 and November of 2006 on the original 24" Houck configuration. A comparison between test sessions is shown in the next 4 slides. Comparisons were done because the wind tunnel was updated with new software. Two similar speeds were tested during each month's testing: 30 mph and 40 mph. The angle of attack was varied from -5° to 15°. Test conditions for each day can be seen below.



Geometric Parameters

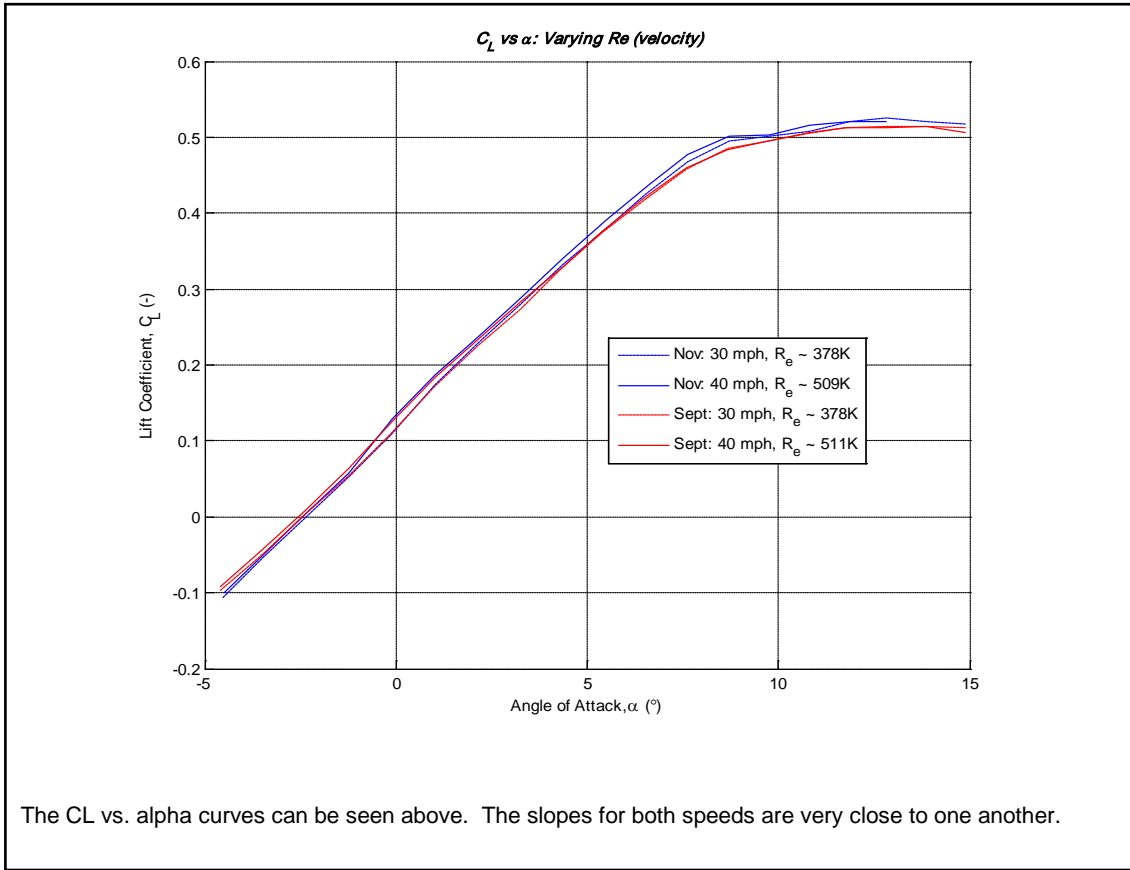
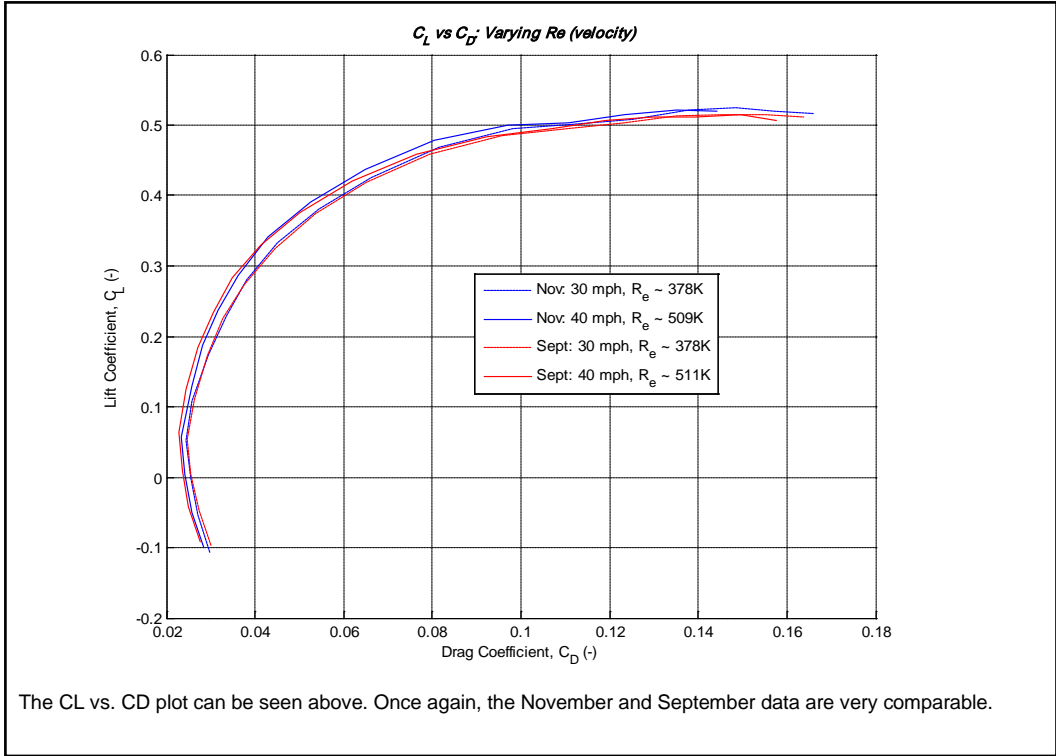
Body_Volume = 248.37 cubic inches
 Wing_Area = 289.3 square inches
 c_bar = 12.265 inches
 span = 23.58 inches
 root_chord = 16.64 inches
 CG located at 1/4 chord of planform area

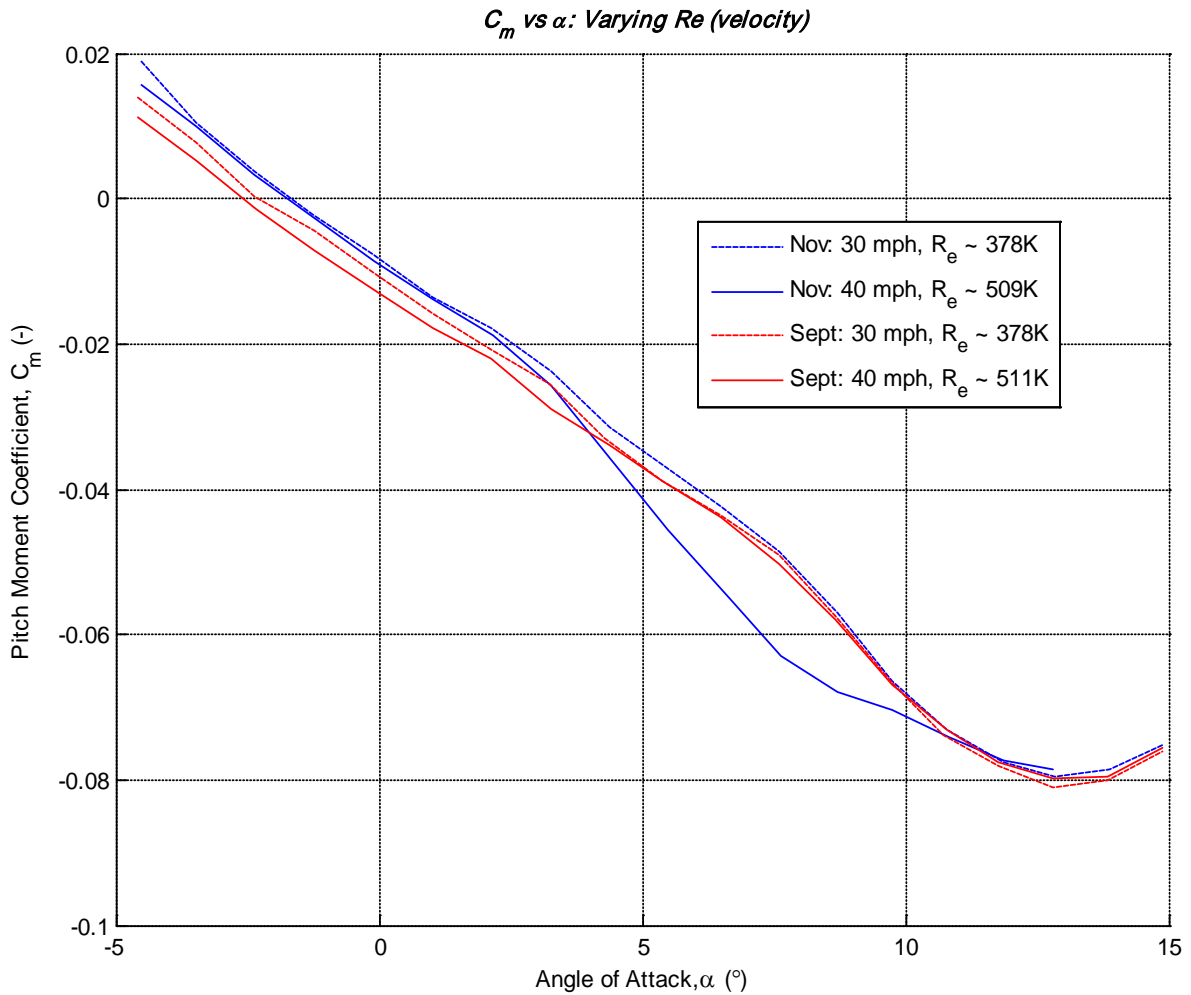
September Data

Mass = 0.89824897 kg
 T_room = 74.1° F
 P_barro = 29.0115 inches Hg

November Data

Mass = 0.89824897 kg
 T_room = 74.6° F
 P_barro = 28.8058 inches Hg





The C_m vs α plot can be seen above. These numbers are not as similar to one another as the other plots have been. This is probably due to an “old” tare file being used for the September runs. The tare file collected before an additional back piece was fitted onto the Houck model. This was a small weight difference (had little effect on lift variations) but was located far from the moment center and could account for differences in a pitching moment.

Wind Tunnel Results: Houck Configuration w/ 3 Different Aileron Settings

The next 4 slides show the wind tunnel data taken in November of 2006. This data compares three different aileron settings on the Houck model. Three speeds were tested for each aileron setting: 20 mph, 30 mph, and 40 mph. The angle of attack was varied from -5° to 15° .



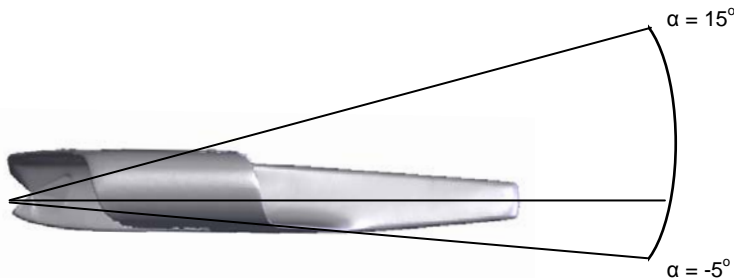
Original Configuration



Ailerons: 20° down



Ailerons: 20° up

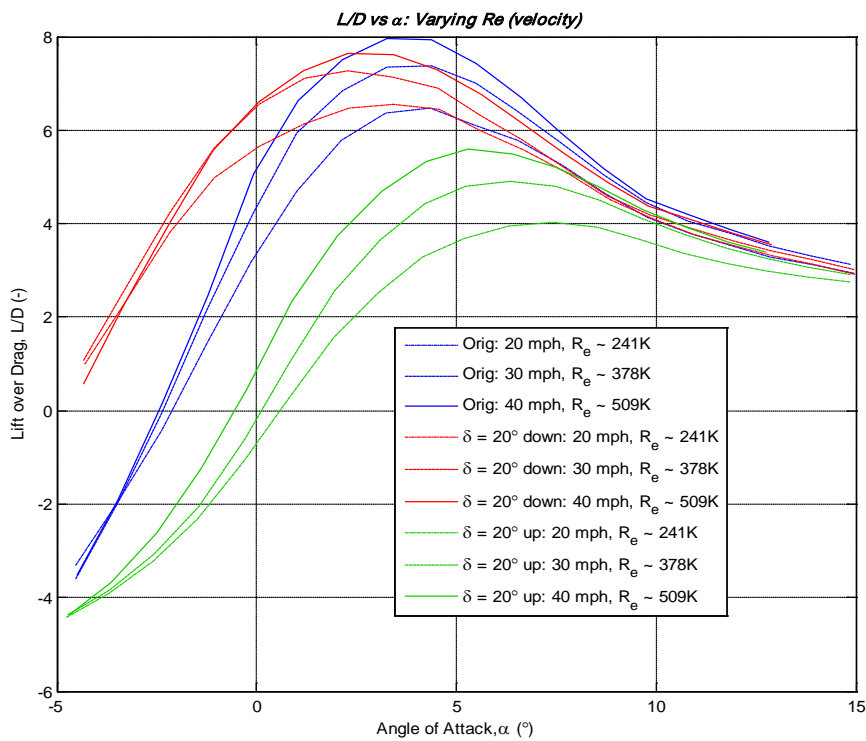


November Data

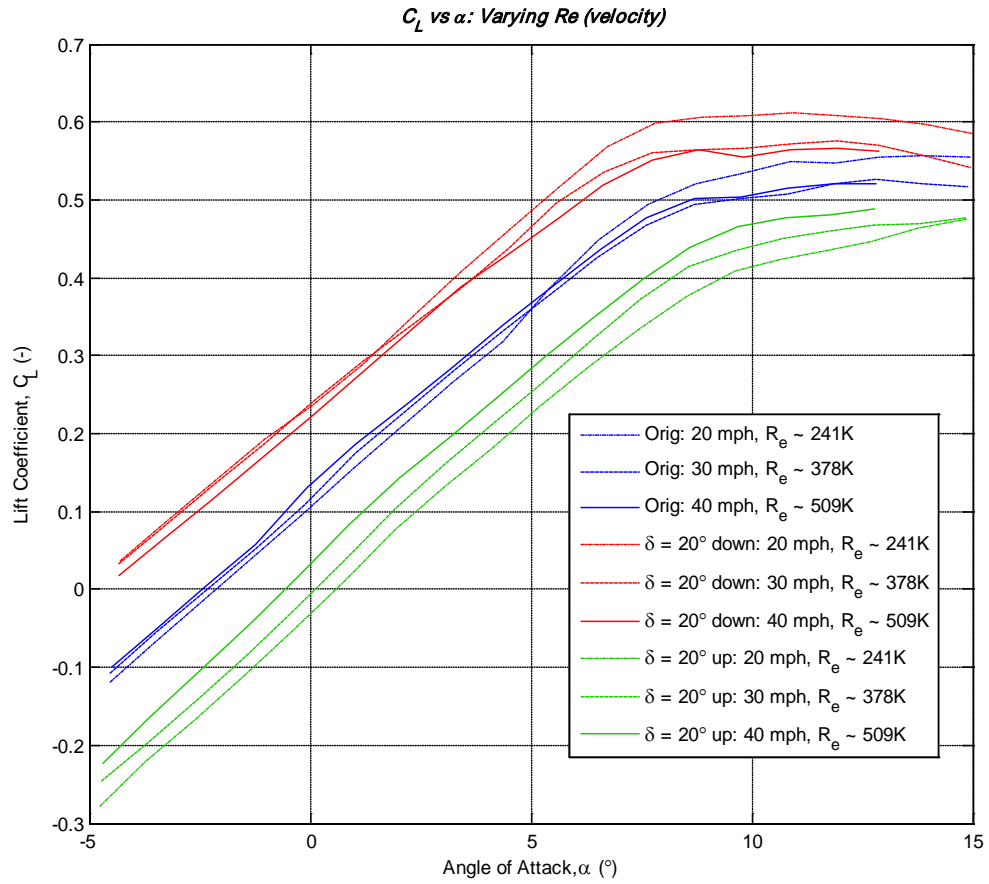
Mass = 0.89824897 kg
 T_{room} = 74.6° F
 P_{barro} = 28.8058 inches Hg

Geometric Parameters

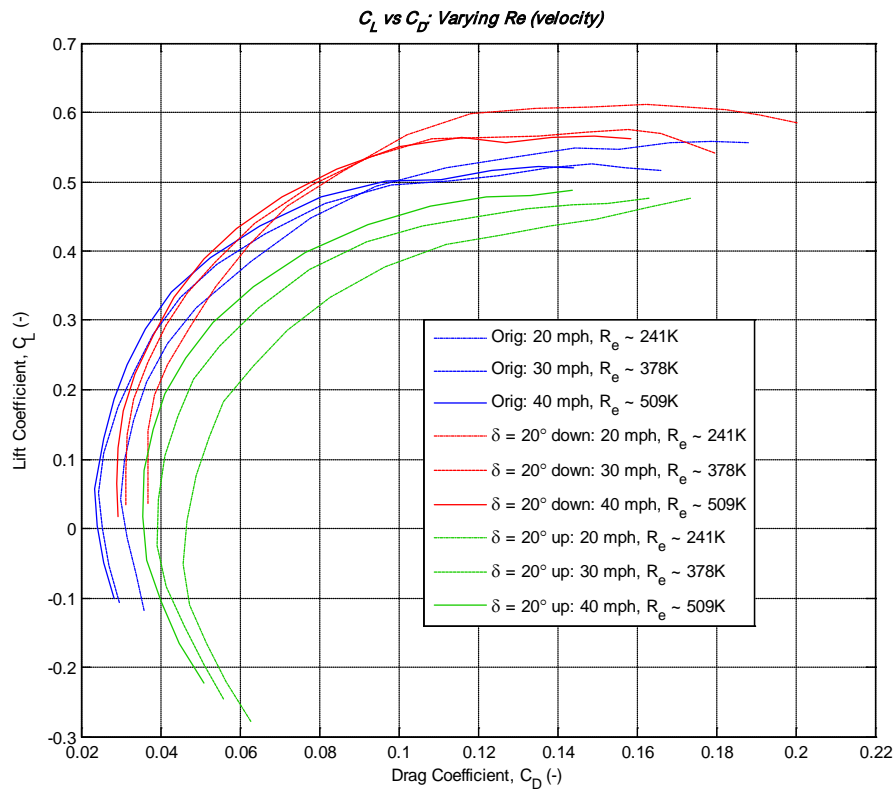
Body_Volume = 248.37 cubic inches
 Wing_Area = 289.3 square inches
 c_{bar} = 12.265 inches
 span = 23.58 inches
 root_chord = 16.64 inches
 CG located at 1/4 chord of planform area



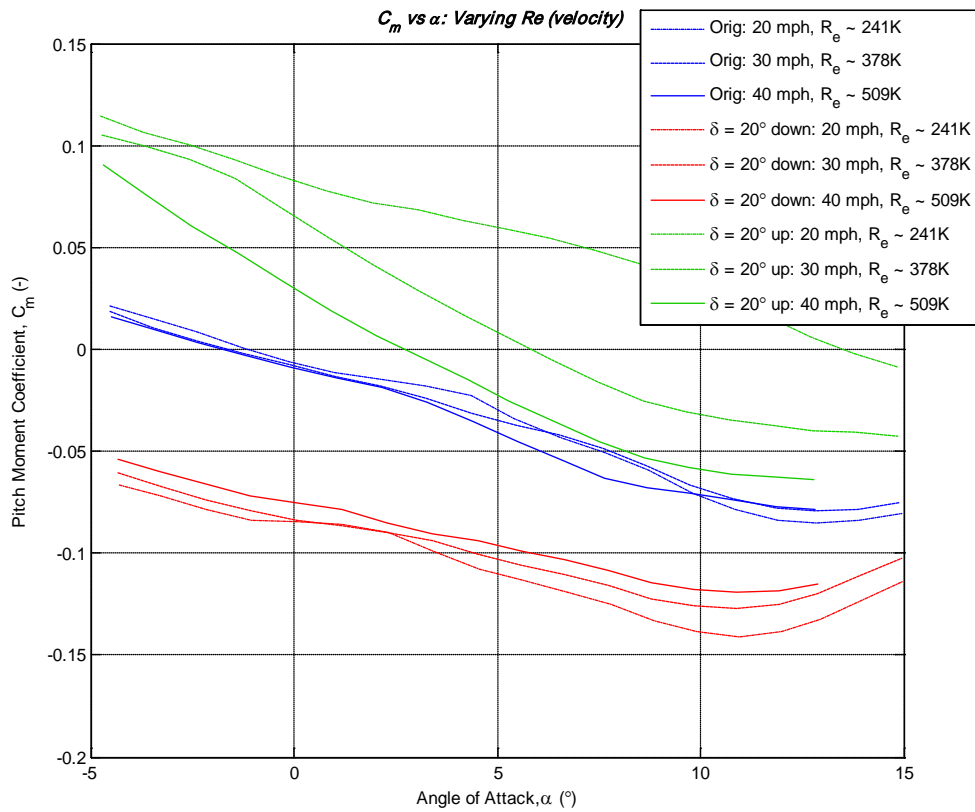
	(Original: Max L/D, AoA)	(20° down: Max L/D, AoA)	(20° up: Max L/D, AoA)
20 mph:	6.5 @ 4.25°	6.6 @ 3.75°	4 @ 7°
30 mph:	7.3 @ 4°	7.15 @ 2.5°	4.8 @ 6.5°
40 mph:	8 @ 3.75°	7.6 @ 3°	5.6 @ 5.5°



The C_L vs α curves can be seen above.



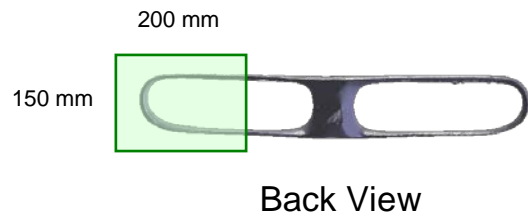
The C_L vs C_D plot can be seen above.



The C_m vs alpha plot can be seen above.

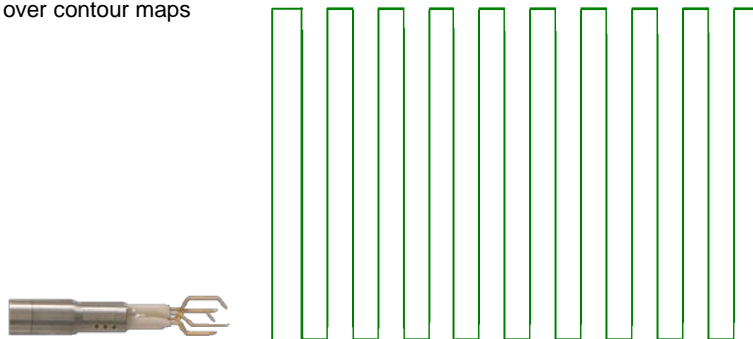
Hot Wire Results: Houck Configuration w/ 3 Different Aileron Settings

A hot wire probe is used to record the velocity behind the wing of the Houck model in three dimensions. The grid is 150 mm by 200 mm with 5 mm resolution. 1271 grid points were measured for each run. 3 angles were examined for each of the 3 aileron settings.



Original Configuration: AoA = -2° , 4° , and 8°
 Ailerons 20° down: AoA = -2° , 4° , and 8°
 Ailerons 20° up: AoA = -2° , 4° , and 8°

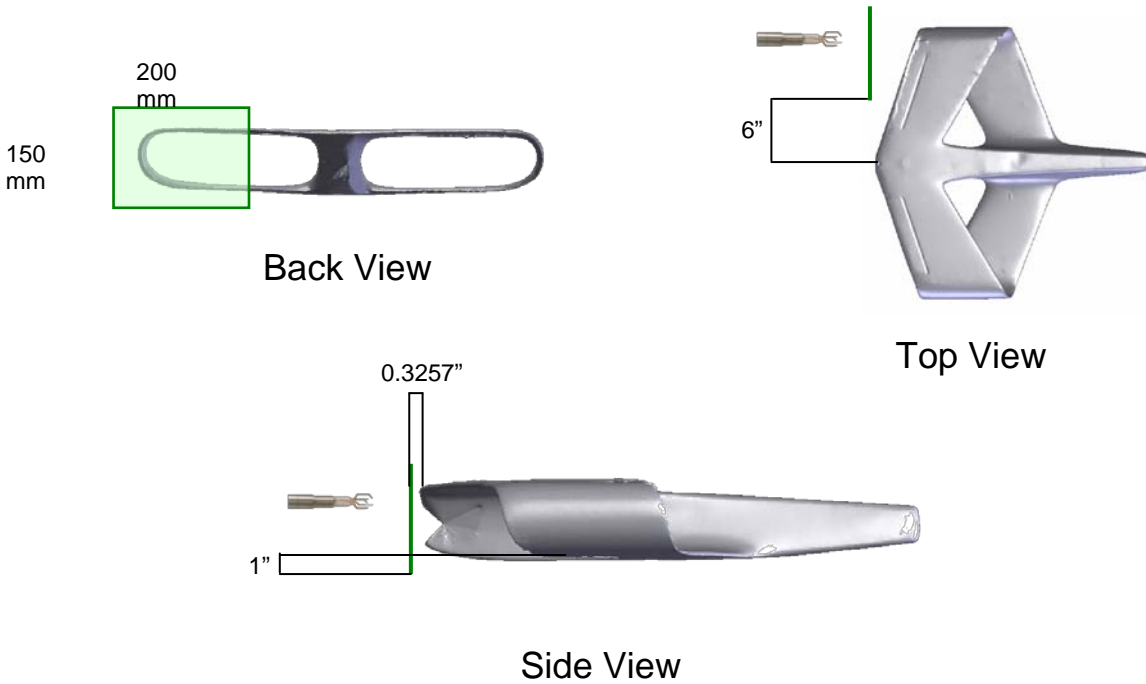
Contour maps can be made from grid point data. Vector plotting can be done as well. Since velocity measurements are in 3-D... Vector fields can be placed over contour maps



Path of the hot wire probe

Hot Wire Results: Houck Configuration w/ 3 Different Aileron Settings

Vertical: 1" below bottom surface of lower wing
 Horizontal: 6" from centerline of model
 Behind: 0.3257" from back of model



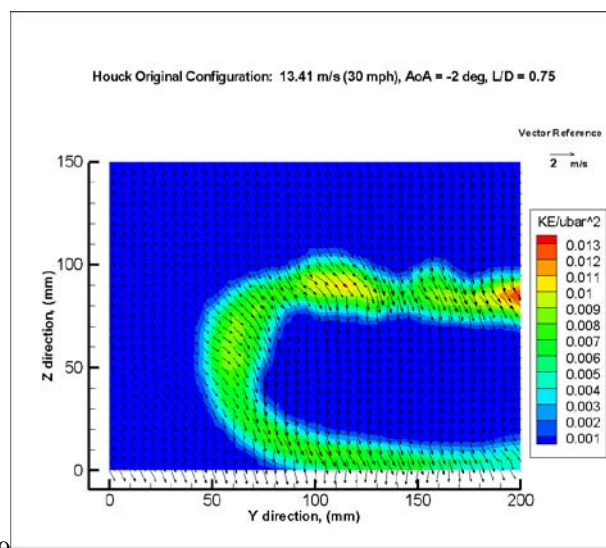
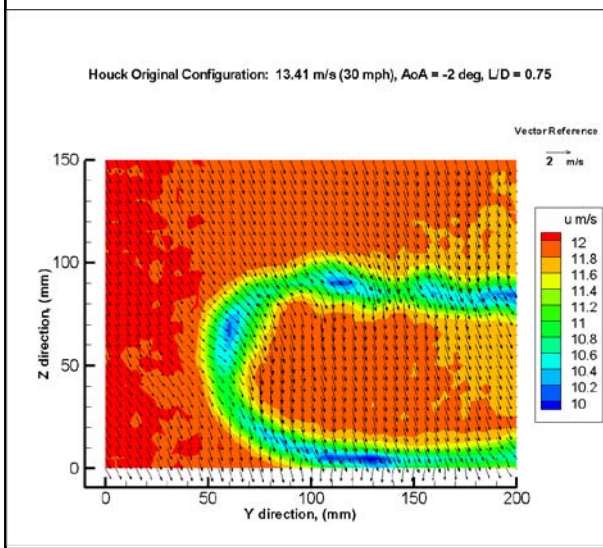
Original Configuration

AoA = -2°
 V = 13.41 m/s (30 mph)



Contour map of u component of velocity with vector field showing v & w components

Contour map of normalized kinetic energy per unit mass with vector field showing v & w components



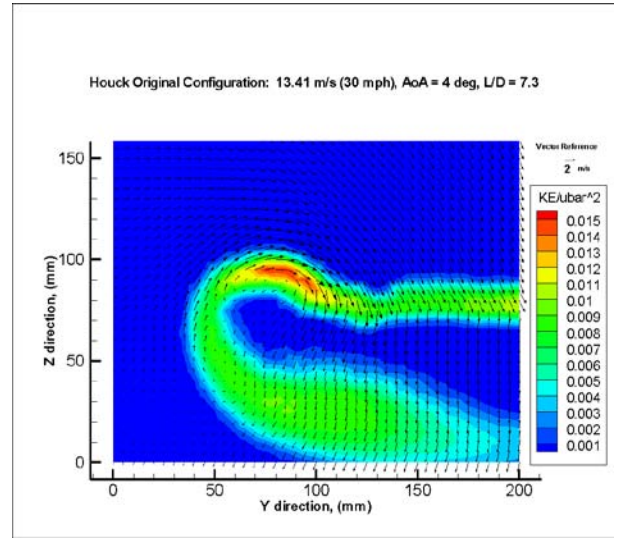
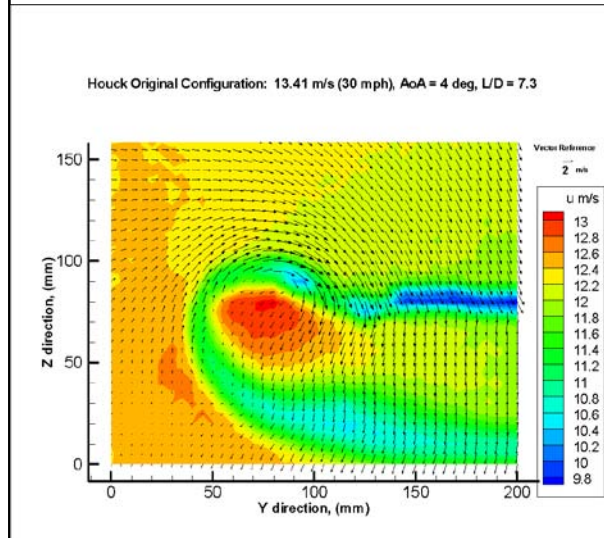
Original Configuration

AoA = 4°
V = 13.41 m/s (30 mph)



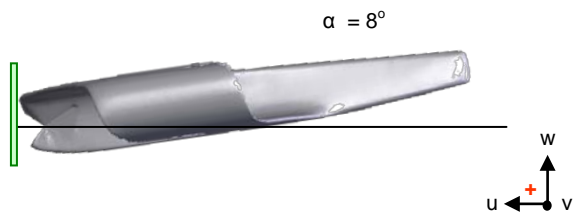
Contour map of u component of velocity with vector field showing v & w components

Contour map of normalized kinetic energy per unit mass with vector field showing v & w components



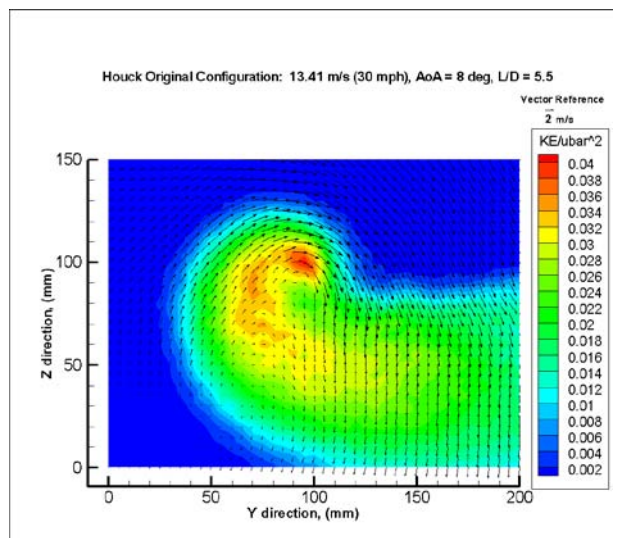
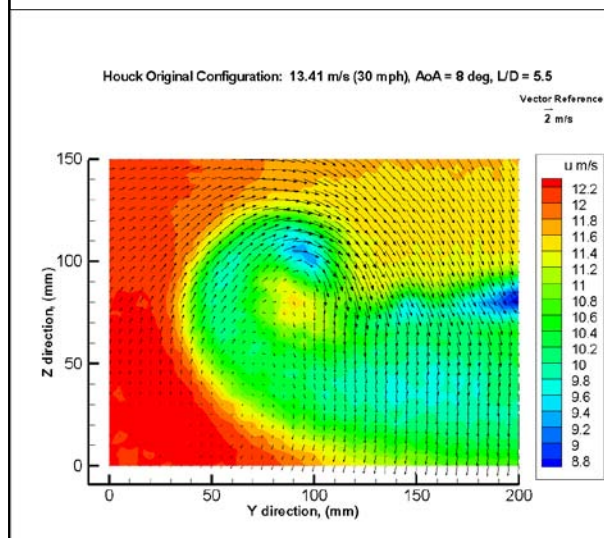
Original Configuration

AoA = 8°
V = 13.41 m/s (30 mph)



Contour map of u component of velocity with vector field showing v & w components

Contour map of normalized kinetic energy per unit mass with vector field showing v & w components



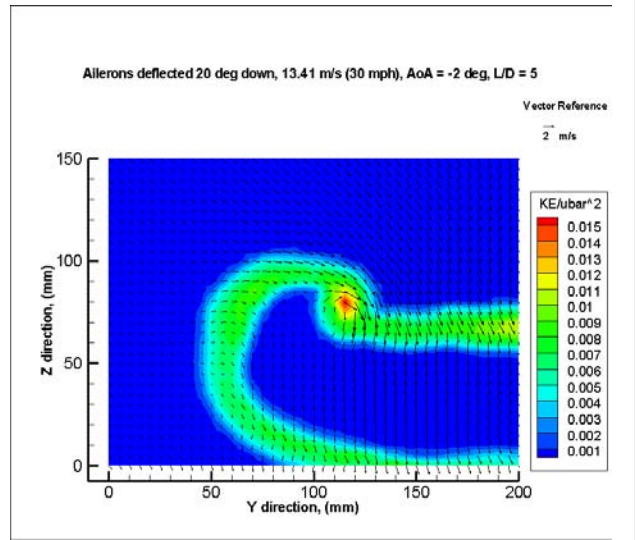
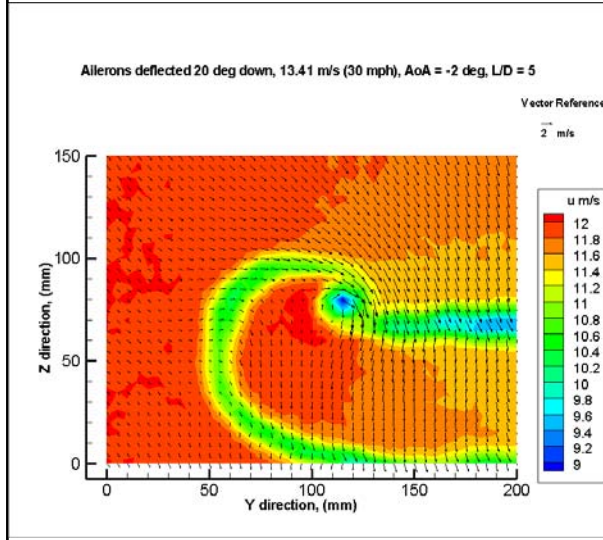
Ailerons: 20° Down

AoA = -2°
V = 13.41 m/s (30 mph)



Contour map of u component of velocity with vector field showing v & w components

Contour map of normalized kinetic energy per unit mass with vector field showing v & w components



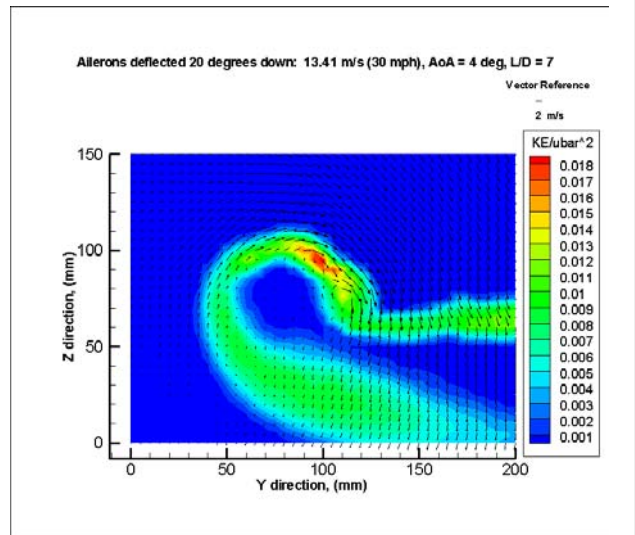
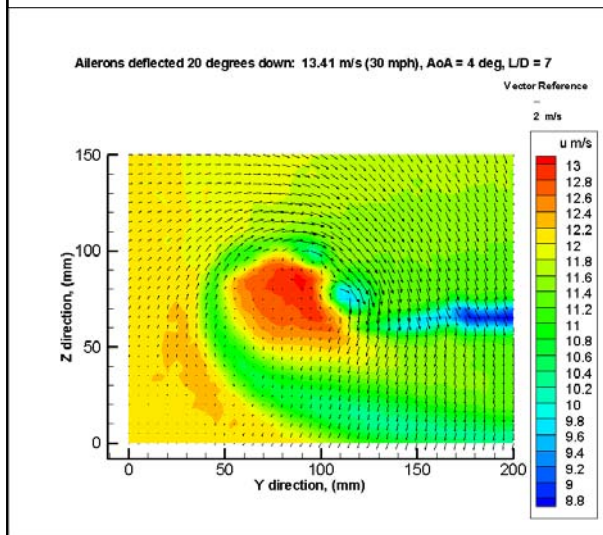
Ailerons: 20° Down

AoA = 4°
V = 13.41 m/s (30 mph)



Contour map of u component of velocity with vector field showing v & w components

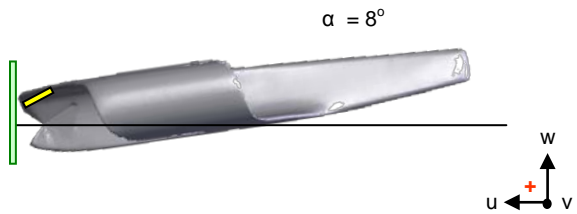
Contour map of normalized kinetic energy per unit mass with vector field showing v & w components



Ailerons: 20° Down

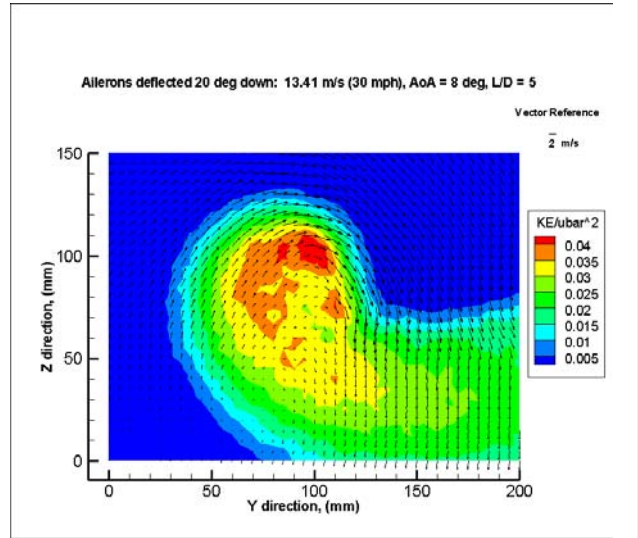
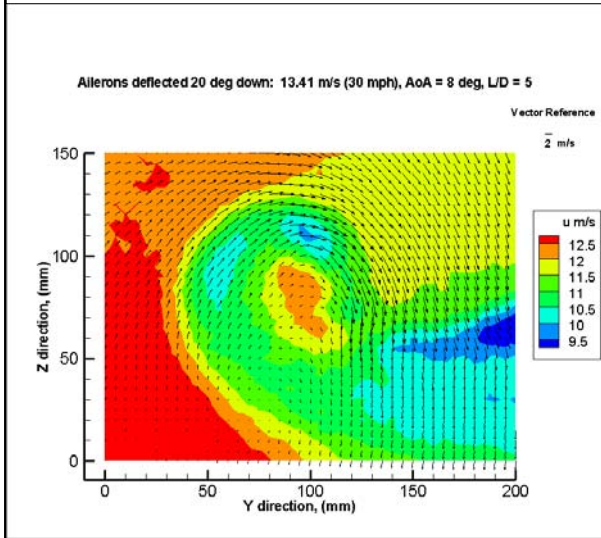
AoA = 8°

V = 13.41 m/s (30 mph)



Contour map of u component of velocity with vector field showing v & w components

Contour map of normalized kinetic energy per unit mass with vector field showing v & w components



Ailerons: 20° Up

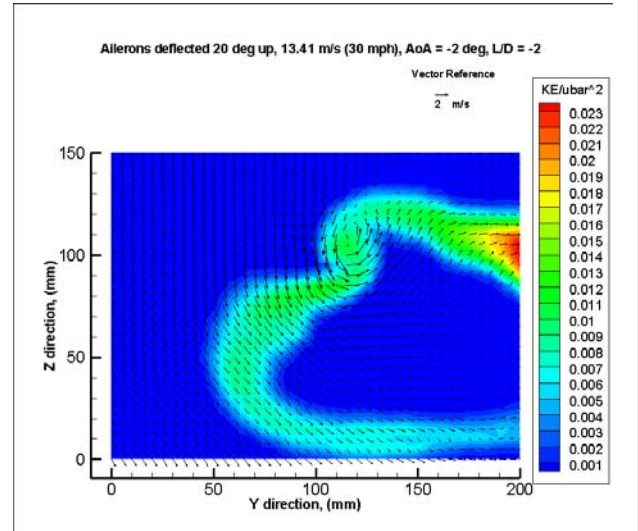
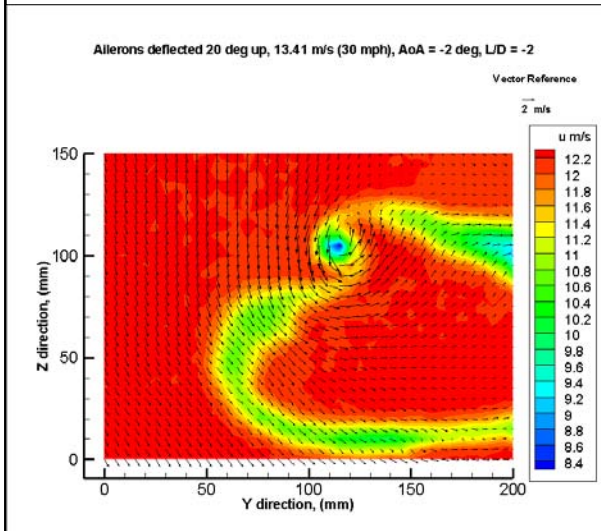
AoA = -2°

V = 13.41 m/s (30 mph)



Contour map of u component of velocity with vector field showing v & w components

Contour map of normalized kinetic energy per unit mass with vector field showing v & w components



Ailerons: 20° Up

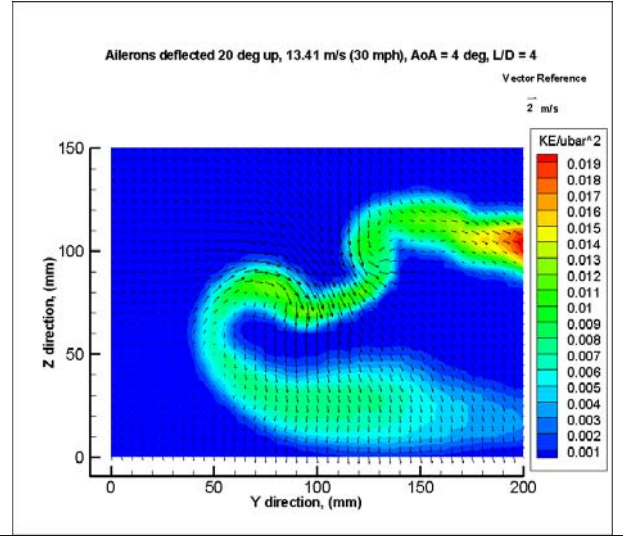
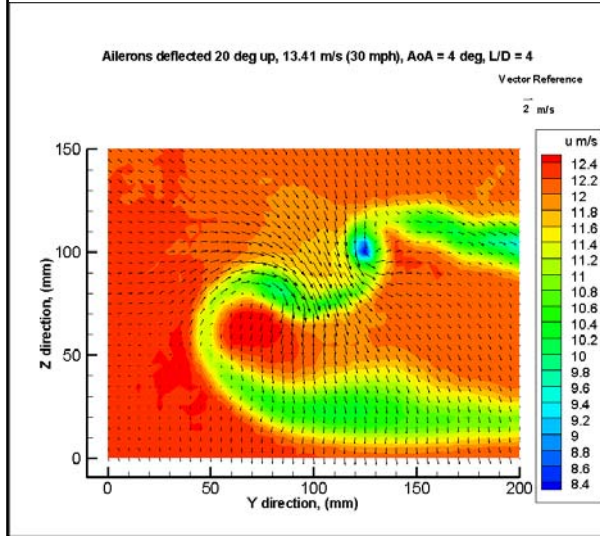
AoA = 4°

V = 13.41 m/s (30 mph)



Contour map of u component of velocity with vector field showing v & w components

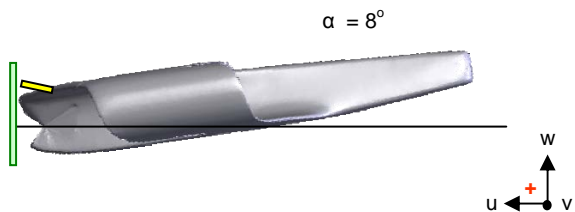
Contour map of normalized kinetic energy per unit mass with vector field showing v & w components



Ailerons: 20° Up

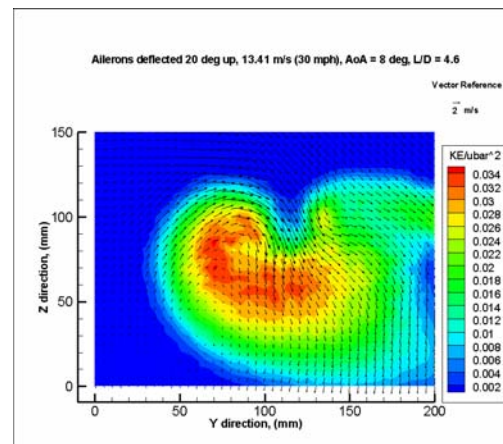
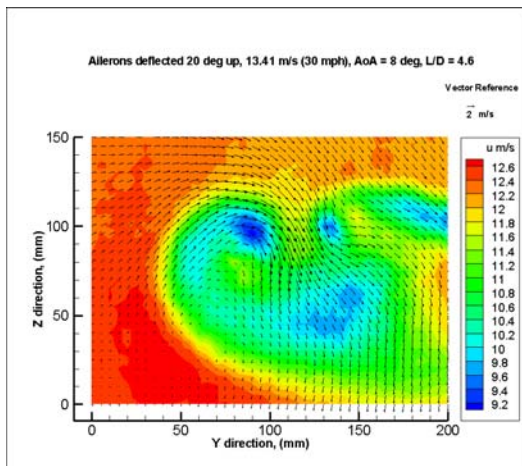
AoA = 8°

V = 13.41 m/s (30 mph)



Contour map of u component of velocity with vector field showing v & w components

Contour map of normalized kinetic energy per unit mass with vector field showing v & w components



Appendix B: Initial Aircraft Sizing Data by Mission

Mission # 1 - Local Surveillance:

INPUTS 1nm=1.151mi		Mission #1		
Payload	4	lb	Propulsion efficiency	0.6 Tbl 2.2 (p14)
Range	1.73761946	nm	Specific fuel consump (cp)	0.5 lbs/hp/hr
Loiter	3	hr		
Cruise or loiter speed	35	mph	Lift/Drag ratio	11
Altitude	1000	ft	Climax	1.2
Field length for TO (ground and upto 50ft)	500	ft	A (reg const Table 2.15 pg 47)	0.3411
Fuel reserve(fraction of mission fuel)	5	%	B (regression constant)	0.9519
Fuel trapped(% of WTO)	0.1	%		
Stall speed	32	mph	Alternate TO power calcs	
			Ground run to attain stall speed	100 ft
Propeller=0, electric=1	0		Horizontal dist to climb 50 ft	100 ft
Phase I (startup and warmup) W1/WTO	0.998	Table 2.1 (pg 12)		
Phase II (Taxi) W2/W1	0.998			
Phase III (Take off) W3/W2	0.998			
Phase IV (Climb to alt) W4/W3	0.995			
Phase V (Cruise) W5/W4	1	computed	0.999649027	
Phase VI (Loiter) W6/W5	1	computed	0.979011273	
Phase VII (Descent) W7/W6	0.995			
Phase VIII (Landing,taxi,shutdwn)W8/W7	0.995			
OUTPUTS				
mff	0.95828813		CommandButton1	
C (reg coeff)	0.95520253			
D (reg coeff)	4			
WTO	8.58759359	lb	Converged	
Wt of fuel used	0.35820463	lb		
Wt of reserve fuel	0.01791023	lb		
Wt of fuel for mission	0.37611486	lb		
Wt of empty plane	4.20289114	lb		
Wing area	2.85846876	ft2	Alternate Power Calcs	
Wing loading (W/S)	3.00426358	lb/ft2	Power to attain stall speed	0.18976275 hp
Power loading (W/P)	22.2772974		Power to climb 50 ft	0.43094732 hp
Power at takeoff	0.38548633	hp	Wing area based on payloadonly	1.3314411 ft2
Ground run distance for TO	301.204819	ft		
Ground run during landing	295.181938	ft		
Total distance for descent from 50 ft	572.062596	ft		
Power at cruise	0.07251517	hp		

Mission # 2 - Targeted Surveillance:

INPUTS 1nm=1.151mi		Mission #2		
Payload	4	lb	Propulsion efficiency	0.6 Tbl 2.2 (p14)
Range	8.68809731	nm	Specific fuel consump (cp)	0.5 lbs/hp/hr
Loiter	0.16666667	hr		
Cruise or loiter speed	35	mph	Lift/Drag ratio	11
Altitude	1000	ft	Clmax	1.2
Field length for TO (ground and upto 50ft)	500	ft	A (reg const Table 2.15 pg 47)	0.3411
Fuel reserve(fraction of mission fuel)	5	%	B (regression constant)	0.9519
Fuel trapped(% of WTO)	0.1	%		
Stall speed	32	mph	Alternate TO power calcs	
			Ground run to attain stall speed	100 ft
Propeller=0, electric=1	0		Horizontal dist to climb 50 ft	100 ft
Phase I (startup and warmup) W1/WTO	0.998	Table 2.1 (pg 12)		
Phase II (Taxi) W2/W1	0.998			
Phase III (Take off) W3/W2	0.998			
Phase IV (Climb to alt) W4/W3	0.995			
Phase V (Cruise) W5/W4	1	computed	0.998246368	
Phase VI (Loiter) W6/W5	1	computed	0.998822243	
Phase VII (Descent) W7/W6	0.995			
Phase VIII (Landing,taxi,shutdwn)W8/W7	0.995			
OUTPUTS				
mff	0.97630791		CommandButton1	
C (reg coeff)	0.97412331			
D (reg coeff)	4			
WTO	8.50625632	lb	Converged	
Wt of fuel used	0.20153095	lb		
Wt of reserve fuel	0.01007655	lb		
Wt of fuel for mission	0.2116075	lb		
Wt of empty plane	4.28614257	lb		
Wing area	2.83139482	ft2	Alternate Power Calcs	
Wing loading (W/S)	3.00426358	lb/ft2	Power to attain stall speed	0.18796542 hp
Power loading (W/P)	22.2772974		Power to climb 50 ft	0.42686561 hp
Power at takeoff	0.3818352	hp	Wing area based on payloadonly	1.3314411 ft2
Ground run distance for TO	301.204819	ft		
Ground run during landing	295.181938	ft		
Total distance for descent from 50 ft	572.062596	ft		
Power at cruise	0.07182835	hp		

Mission # 3 - Widespread Surveillance:

INPUTS 1nm=1.151mi		Mission #3		
Payload	4	lb	Propulsion efficiency	0.6 Tbl 2.2 (p14)
Range	8.68809731	nm	Specific fuel consump (cp)	0.5 lbs/hp/hr
Loiter	3	hr		
Cruise or loiter speed	35	mph	Lift/Drag ratio	11
Altitude	2000	ft	CImax	1.2
Field length for TO (ground and upto 50ft)	500	ft	A (reg const Table 2.15 pg 47)	0.3411
Fuel reserve(fraction of mission fuel)	5	%	B (regression constant)	0.9519
Fuel trapped(% of WTO)	0.1	%		
Stall speed	32	mph	Alternate TO power calcs	
			Ground run to attain stall speed	100 ft
Propeller=0, electric=1	0		Horizontal dist to climb 50 ft	100 ft
Phase I (startup and warmup) W1/WTO	0.998	Table 2.1 (pg 12)		
Phase II (Taxi) W2/W1	0.998			
Phase III (Take off) W3/W2	0.998			
Phase IV (Climb to alt) W4/W3	0.995			
Phase V (Cruise) W5/W4	1	computed	0.998246368	
Phase VI (Loiter) W6/W5	1	computed	0.979011273	
Phase VII (Descent) W7/W6	0.995			
Phase VIII (Landing,taxi,shutdwn)W8/W7	0.995			
OUTPUTS				
mff	0.9569435		CommandButton1	
C (reg coeff)	0.95379068			
D (reg coeff)	4			
WTO	8.9937923	lb	Converged	
Wt of fuel used	0.3872412	lb		
Wt of reserve fuel	0.01936206	lb		
Wt of fuel for mission	0.40660326	lb		
Wt of empty plane	4.57819525	lb		
Wing area	3.08308971	ft2	Alternate Power Calcs	
Wing loading (W/S)	2.91713611	lb/ft2	Power to attain stall speed	0.19873865 hp
Power loading (W/P)	22.9426639		Power to climb 50 ft	0.4513314 hp
Power at takeoff	0.39201168	hp	Wing area based on payloadonly	1.37120787 ft2
Ground run distance for TO	301.204819	ft		
Ground run during landing	295.181938	ft		
Total distance for descent from 50 ft	572.062596	ft		
Power at cruise	0.07594519	hp		

Mission # 4 - Stealth Observation:

INPUTS 1nm=1.151mi		Mission #4		
Payload	4	lb	Propulsion efficiency	0.6 Tbl 2.2 (p14)
Range	17.3761946	nm	Specific fuel consump (cp)	0.5 lbs/hp/hr
Loiter	0.33333333	hr		
Cruise or loiter speed	35	mph	Lift/Drag ratio	11
Altitude	2000	ft	Clmax	1.2
Field length for TO (ground and upto 50ft)	500	ft	A (reg const Table 2.15 pg 47)	0.3411
Fuel reserve(fraction of mission fuel)	5	%	B (regression constant)	0.9519
Fuel trapped(% of WTO)	0.1	%		
Stall speed	32	mph	Alternate TO power calcs	
			Ground run to attain stall speed	100 ft
Propeller=0, electric=1	0		Horizontal dist to climb 50 ft	100 ft
Phase I (startup and warmup) W1/WTO	0.998	Table 2.1 (pg 12)		
Phase II (Taxi) W2/W1	0.998			
Phase III (Take off) W3/W2	0.998			
Phase IV (Climb to alt) W4/W3	0.995			
Phase V (Cruise) W5/W4	1	computed	0.996495812	
Phase VI (Loiter) W6/W5	1	computed	0.997645873	
Phase VII (Descent) W7/W6	0.995			
Phase VIII (Landing,taxi,shutdwn)W8/W7	0.995			
OUTPUTS				
mff	0.97344799		CommandButton1	
C (reg coeff)	0.97112039			
D (reg coeff)	4			
WTO	8.51895377	lb	Converged	
Wt of fuel used	0.22619532	lb		
Wt of reserve fuel	0.01130977	lb		
Wt of fuel for mission	0.23750509	lb		
Wt of empty plane	4.27292973	lb		
Wing area	2.92031412	ft ²	Alternate Power Calcs	
Wing loading (W/S)	2.91713611	lb/ft ²	Power to attain stall speed	0.188246 hp
Power loading (W/P)	22.9426639		Power to climb 50 ft	0.4275028 hp
Power at takeoff	0.37131494	hp	Wing area based on payloadonly	1.37120787 ft ²
Ground run distance for TO	301.204819	ft		
Ground run during landing	295.181938	ft		
Total distance for descent from 50 ft	572.062596	ft		
Power at cruise	0.07193557	hp		

Mission # 5 - Local Surveillance with Larger Payload:

INPUTS 1nm=1.151mi		Mission #5			
Payload	10	lb	Propulsion efficiency	0.6	Tbl 2.2 (p14)
Range	1.73761946	nm	Specific fuel consump (cp)	0.5	lbs/hp/hr
Loiter	3	hr			
Cruise or loiter speed	35	mph	Lift/Drag ratio	11	
Altitude	1000	ft	Climax	1.2	
Field length for TO (ground and upto 50ft)	500	ft	A (reg const Table 2.15 pg 47)	0.3411	
Fuel reserve(fraction of mission fuel)	5	%	B (regression constant)	0.9519	
Fuel trapped(% of WTO)	0.1	%			
Stall speed	32	mph	Alternate TO power calcs		
			Ground run to attain stall speed	100	ft
Propeller=0, electric=1	0		Horizontal dist to climb 50 ft	100	ft
Phase I (startup and warmup) W1/WTO	0.998	Table 2.1 (pg 12)			
Phase II (Taxi) W2/W1	0.998				
Phase III (Take off) W3/W2	0.998				
Phase IV (Climb to alt) W4/W3	0.995				
Phase V (Cruise) W5/W4	1	computed	0.999649027		
Phase VI (Loiter) W6/W5	1	computed	0.979011273		
Phase VII (Descent) W7/W6	0.995				
Phase VIII (Landing,taxi,shutdown)W8/W7	0.995				
OUTPUTS					
mff	0.95828813		CommandButton1		
C (reg coeff)	0.95520253				
D (reg coeff)	10				
WTO	23.468984	lb	Converged		
Wt of fuel used	0.97893531	lb			
Wt of reserve fuel	0.04894677	lb			
Wt of fuel for mission	1.02788208	lb			
Wt of empty plane	12.4176329	lb			
Wing area	7.81189245	ft2	Alternate Power Calcs		
Wing loading (W/S)	3.00426358	lb/ft2	Power to attain stall speed	0.51860151	hp
Power loading (W/P)	22.2772974		Power to climb 50 ft	1.17773339	hp
Power at takeoff	1.05349332	hp	Wing area based on payloadonly	3.32860275	ft2
Ground run distance for TO	301.204819	ft			
Ground run during landing	295.181938	ft			
Total distance for descent from 50 ft	572.062596	ft			
Power at cruise	0.19817629	hp			

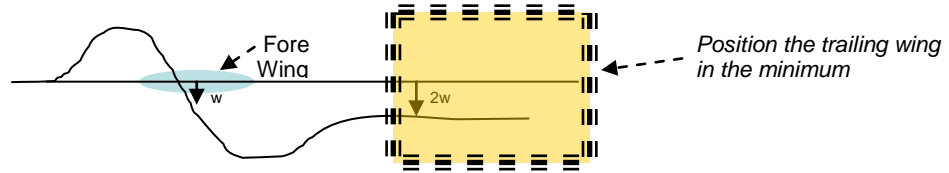
Appendix C: Interim Designs and Details in Configuration Development

This appendix contains a collection of drawings and text that provide documentation of many of the design iterations experienced in Phases III and IV of the Houck program.

Some Background Notes:

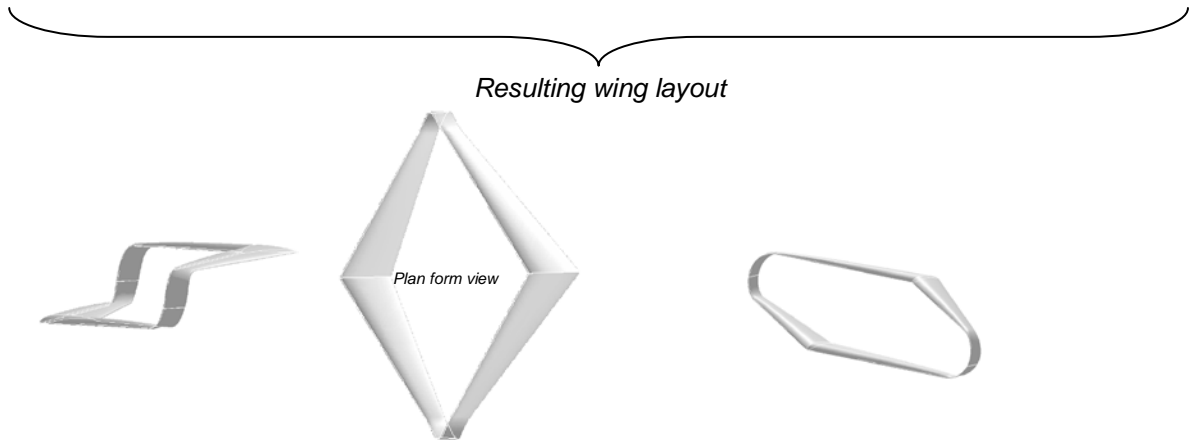
Wing layout selected to minimize fore/aft wing interference drag and maximize performance:

-Minimize downwash

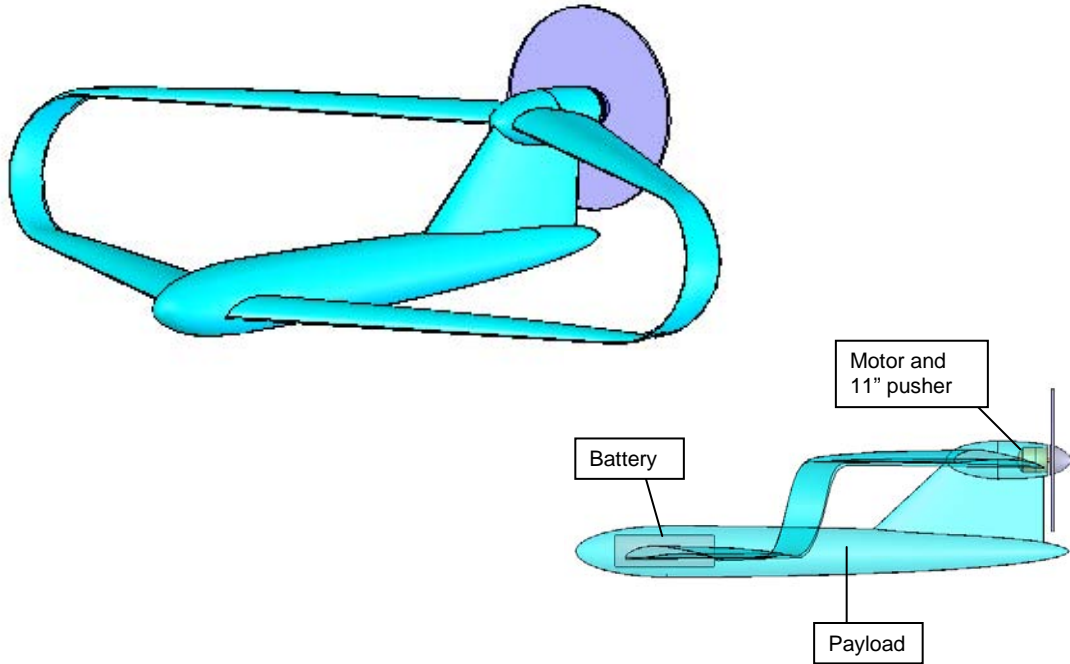


- Von Karman Institute findings for bi-planes, box-wings and C-wings used as a guidance in placing the wings suggested optimum overall height/span ~ 1

- Wing cross-section: Selig airfoil (selected based on recommendations received in prior team meeting)

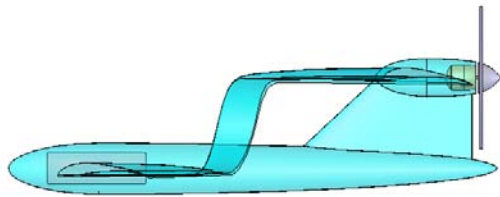


Initial Configuration Based on Preliminary Sizing Calculations (4/12/07):

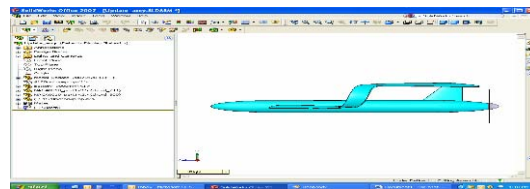


Some Steps in Houck Configuration Evolution:

Based on feedback overall configuration modified:

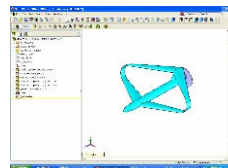


April 12, 2007



April 20, 2007

Thrust vector lined with center of fuselage (c.g.) and narrow tail



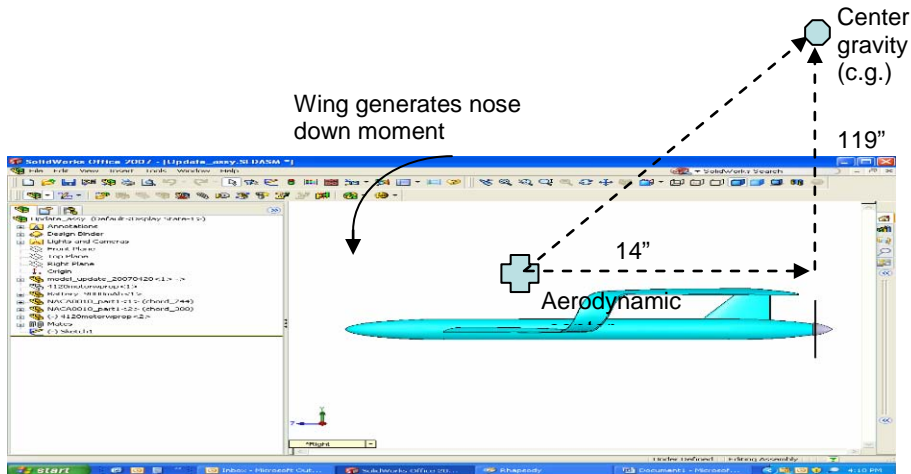
Is the current airplane trimmable? (can it maintain level flight ?)

Trim Considerations:

Trim (pitch) of 4/20/07 configuration:

Nose-down pitching moment 3 N-m for Lift of 40 N

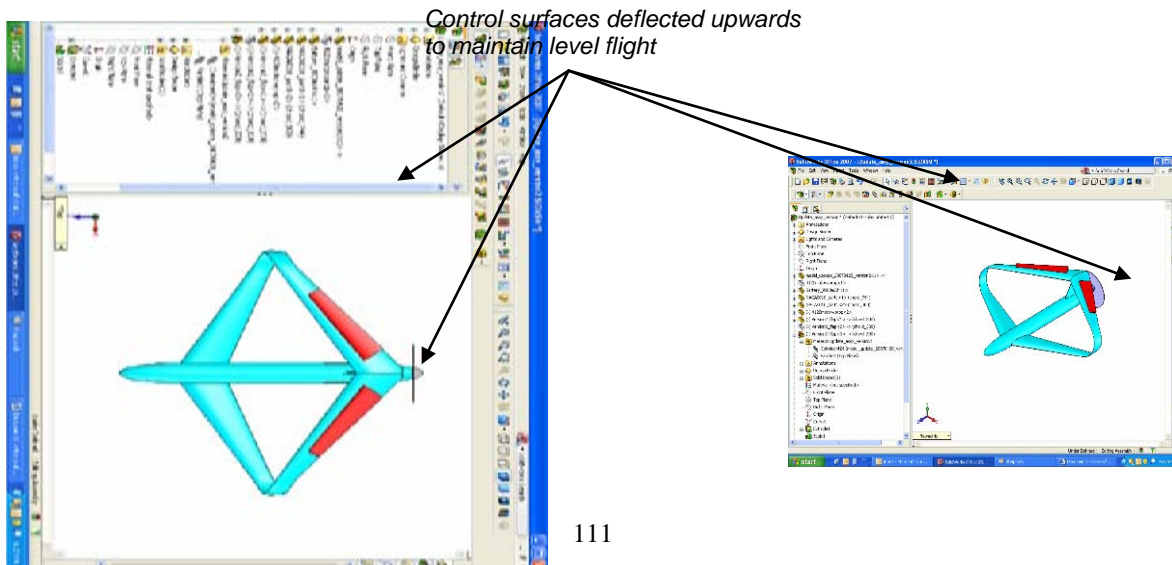
To maintain level flight locate c.g. at 14" behind a.c. and 119" above a.c. --- Not achievable
Nose-down moment is too large and cannot be counteracted by locating the c.g. will need to trim using control surfaces.



Houck UAV Configuration – Trim Option I:

Trim airplane using control surfaces on the current wing:

- Requires –ve Lift on control surface (20% negative lift)
- Reduction in L/D due to negative lift.
- Flow over wing will not be clean (performance and L/D adversely effected)

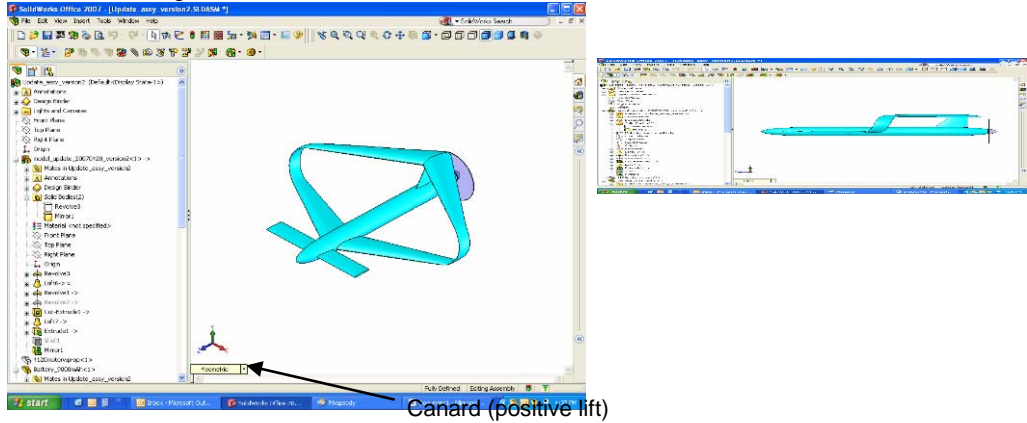


Houck UAV Configuration – Trim Option II:

Trim airplane using a canard:

- Canard contributes to lift (20% lift)
- Inherent stability in pitch and greater control.
- Allows integration of Houck wing gains with traditional aircraft technology.

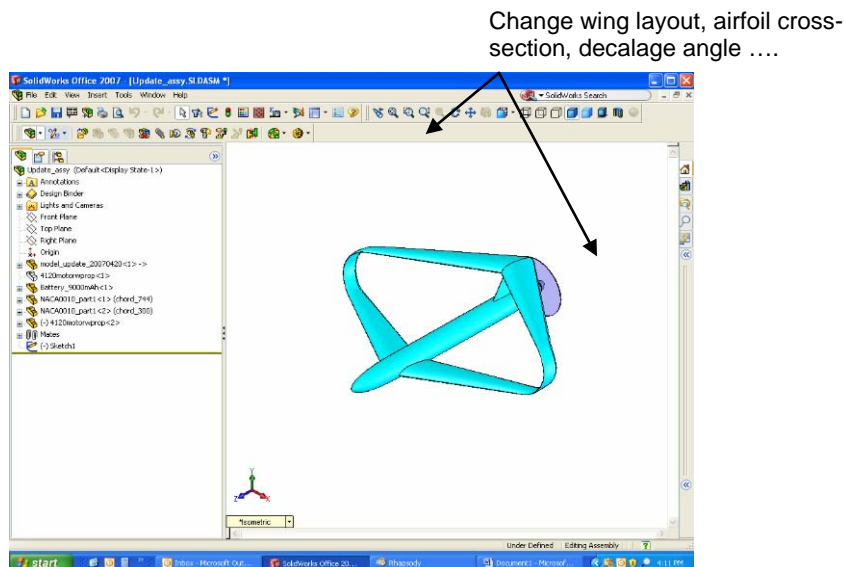
Canard area is 20% of wing area and is located at 17" from a.c.



Houck UAV Configuration – Trim Option III-A:

Redesign rear-wing:

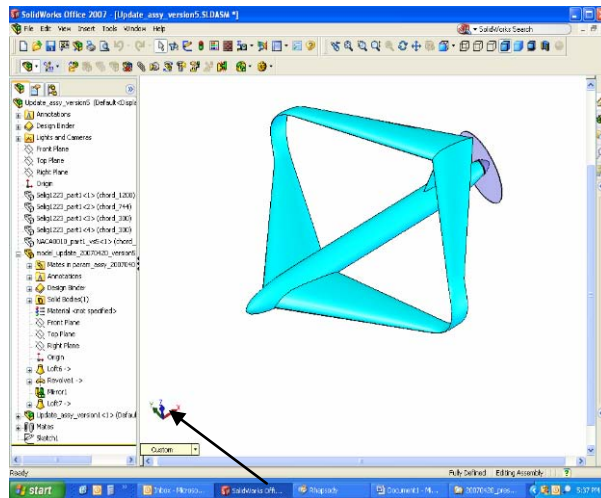
- Evaluate alternate airfoils, change decalage angle – may impact mission, may result in the same conclusions as current design.



Houck UAV Configuration – Trim Option III-B:

Redesign front-wing

- Integrate canard surface into wing to make it larger
 - Likely to alter lift distribution between leading and trailing wing resulting in less than optimum performance.

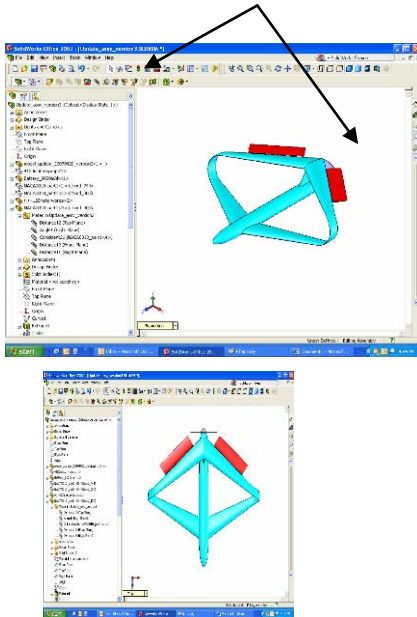


Larger front wing

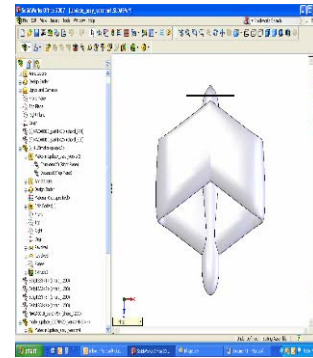
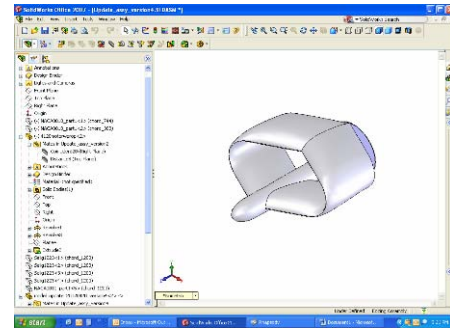
Houck UAV Configuration – Trim Option IV:

A) Redesign the plane to be similar to flying wing UAVs (locate auxiliary control surfaces at the trailing edge of wing).

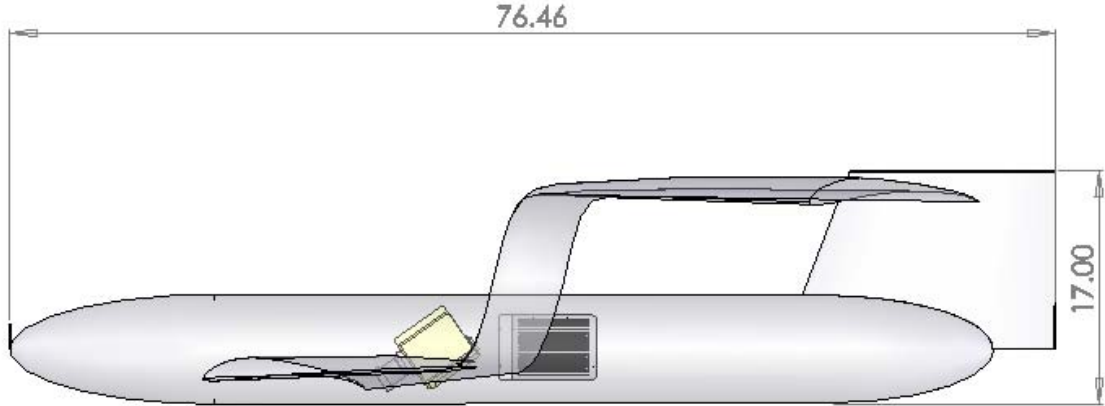
Locate auxiliary surfaces at the trailing edge of the wing. Surfaces deflected upwards (-ve lift) to counteract pitching moment.



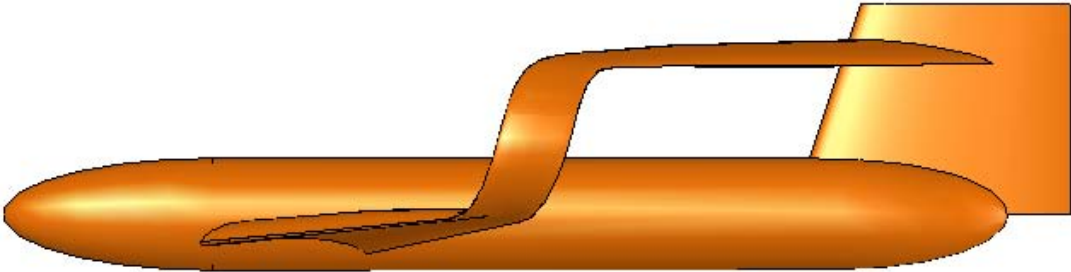
B) Reduced aspect ratio (will result in reduced L/D).
- Likely to compromise performance.



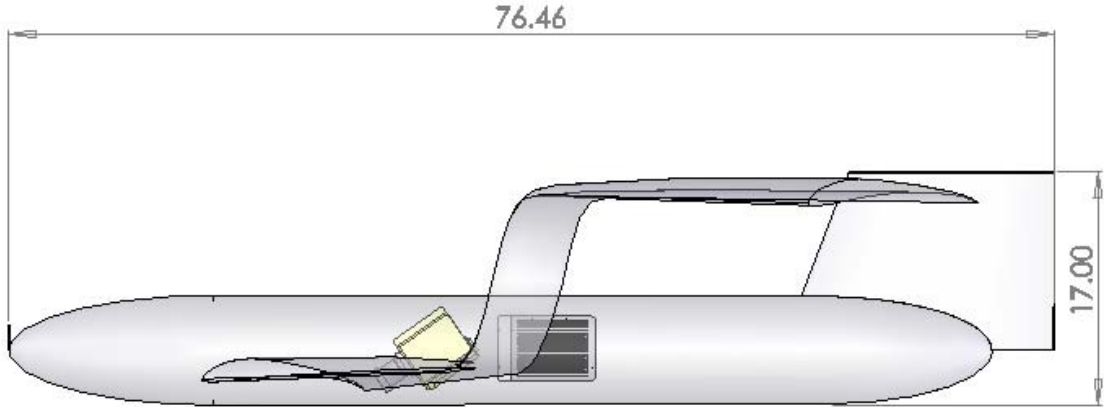
Heavy Lift Prototype Design – Rev 0



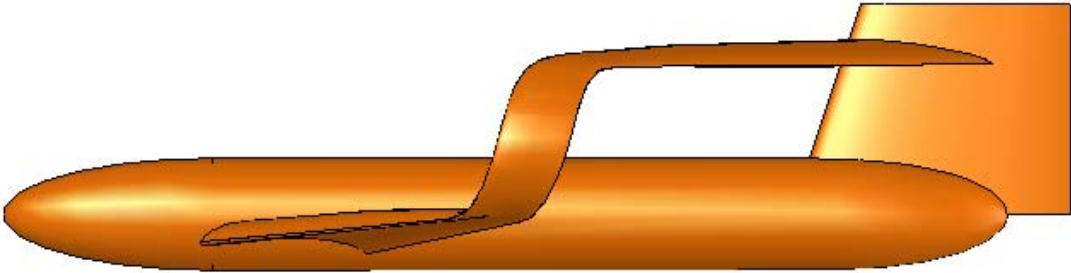
Enlarged
Tail



Design Comparison: Rev 0 to Rev 1



Enlarged Tail

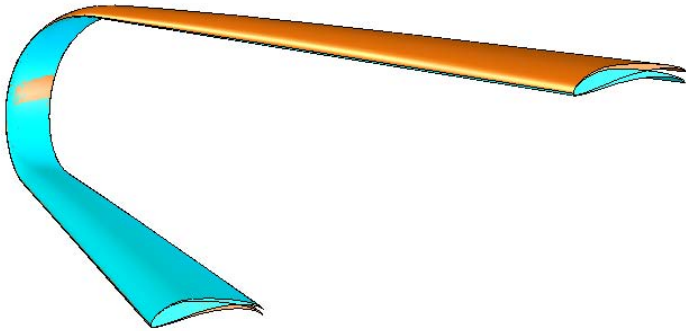


Detailed Design Modifications:

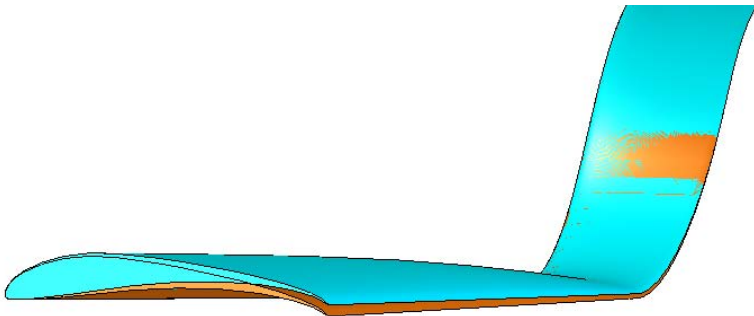
The following detailed design modifications were made to improve the trimmability of the aircraft.

Design 1 in light blue, Design 2 in orange.

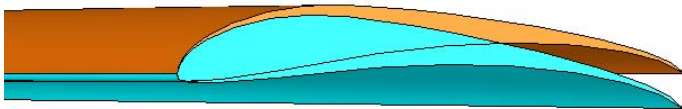
Isometric view



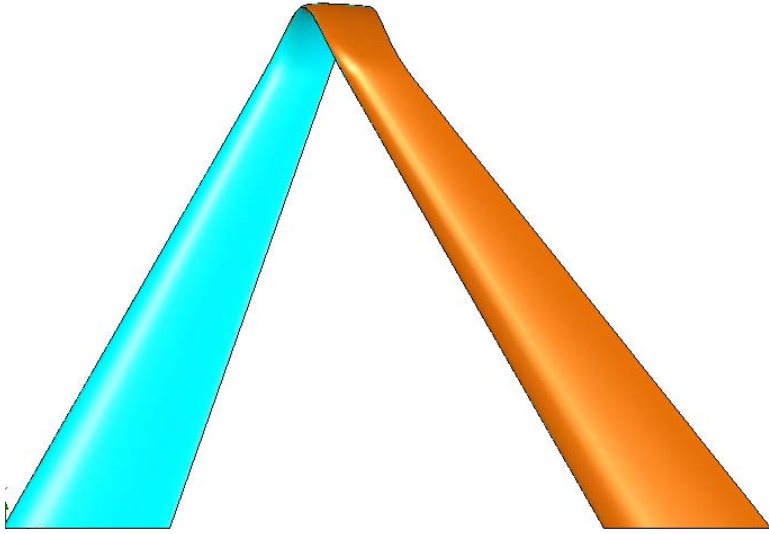
Detail of lower wing at root. Design 2 has 2 degrees higher angle of attack.



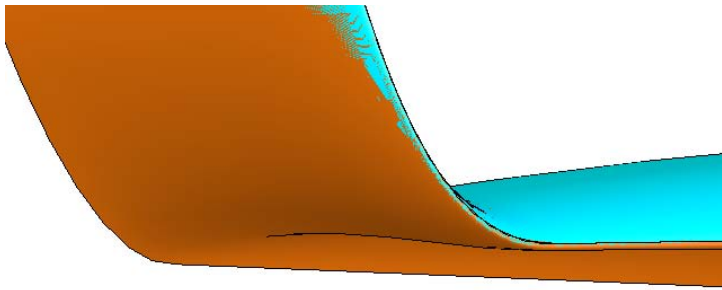
Detail of upper wing at root. Design 2 has 4 degrees lower angle of attack.



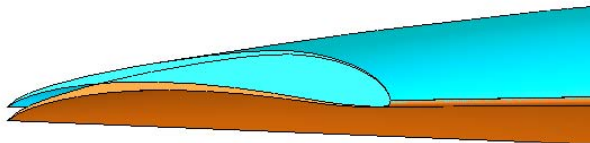
Plan view



Wingtip detail



Wingtip lower section view, Design 2 has 2 degrees higher angle of attack at wingtip



Wingtip upper section view, Design 2 has 4 degrees lower angle of attack at wingtip



Appendix D: VSAERO Evaluation Document

Status Update of VSAERO Evaluation (Feb 1, 2007)

Current Findings:

The ability to create a VSAERO input file has been explored. The key findings are as follows:

1. VSAERO works with a single input file. This file contains geometry, mesh, wake and flow conditions data. The file is quite cryptic in nature, uses a fixed format and is sensitive to the location of the input data (data needs to be specific columns).
2. VSAERO requires two types of geometry input. The first input specifies the body and surface panels. The second set of input describes the wake.
3. STL file is comprised of tessellated surfaces consisting of triangles. The vertices of the triangles and the connectivity information can be used to generate VSAERO geometry input. However, the triangles in the STL file have duplicate nodes and are of high aspect ratio. VSAERO prefers equilateral triangles and duplicate nodes are not allowed.
4. VSAERO requires duplicate nodes at the trailing edge (wake origination locations).
5. The wake specification is available only through a specialized GUI and based on the current information this step cannot be automated. It requires user intervention.

Immediate Next Steps:

1. Identify a method of creating high resolution STL files with nearly equilateral triangles. If this is possible then explore methods to remove duplicate nodes except at the trailing edge (wake attachment points).
2. If STL files are not suitable then explore alternate methods such as using IDEAS to create a mesh.
3. Test these geometries in VSAERO for compatibility.

Further Evaluation:

1. Evaluate the accuracy of VSAERO for previously computed solutions (Neely CFD and wind-tunnel data for Houck wing).
2. This will conclude the evaluation process. It must be noted that the VSAERO geometry data will be created using cutting and pasting of node and element information from a geometry file into a VSAERO input file; automation of this task will be investigated once the evaluation is completed.

Issues to Consider:

1. VSAERO provides rapid solutions; it is possible to create Cl vs. alpha curve for a wing configuration within a day. The same information can be generated using Fluent; however this will require about a week of elapsed time. The man-time using VSAERO and CFD will probably be the same but the solution time for a CFD solution will be huge.
2. VSAERO is not suitable for separated flow; a full N-S (Fluent) solution is required for such cases.
3. VSAERO is relatively unknown (as compared to Fluent) there may be hidden risks associated with this approach.
4. Development effort is required to automatically convert geometry data into VSAERO input.
5. The time benefits using a VSAERO based solution must carefully be weighed against a full blown CFD solution.

Appendix E: L/D_{\max} Calculations for Houck Concept

H.S. Pordal (April 26, 2007)

Standard Wing:

Using basic aerodynamic theory L/D_{\max} for a standard wing can be computed using equation

(1)

$$L/D_{\max} = 0.5 (\pi e \cdot AR/C_{do})^{1/2}, \quad (1)$$

where e efficiency, AR is aspect ratio and C_{do} is zero lift drag coefficient.

$$L_{sw} = q S_{sw} C_l \quad (2)$$

$$D_{sw} = q S_{sw} C_{do} + L_{sw}^2 / (\pi q e \cdot b_{sw}^2), \quad (3)$$

where q is dynamic pressure and b is wing span

Houck Wing:

The Houck wing and standard wing are designed to carry the same load and hence have the same wing loading. The wings are illustrated in Figure 1.

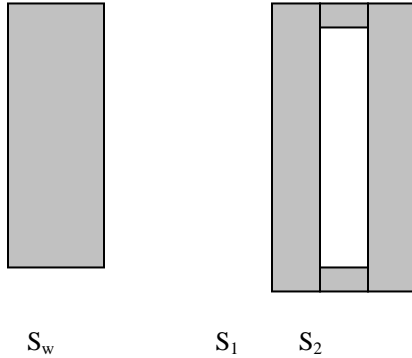


Figure 1: Wings

Wing areas are related using equation (4)

$$S_w = S_1 + S_2 \quad (4)$$

The lift is related using equation (5)

$$L_{sw} = L_1 + L_2 \quad (5)$$

Let $L_1 = f \cdot L_{sw}$, therefore $L_2 = (1-f) \cdot L_{sw}$, f is fraction

Let $b_h = g \cdot b_{sw}$, where b_h is span of Houck wing and b_{sw} is span of standard wing and g is ratio between the two.

$$(L/D)_{\max} = g \cdot (0.5) (\pi e \cdot AR/C_{do})^{1/2} / (2f^2 - 2f + 1), \quad (6)$$

L/D is maximized by increasing the span ratio (g) and decreasing the function, $(2f^2 - 2f + 1)$. The maximum allowable value of g is dependent on structural requirements. A plot of the function $(2f^2 - 2f + 1)$ as depicted in Figure 2 indicates a minimum at $f=0.5$. This indicates that to maximize the L/D for the Houck wing the loading on the front and back wing should be equal.

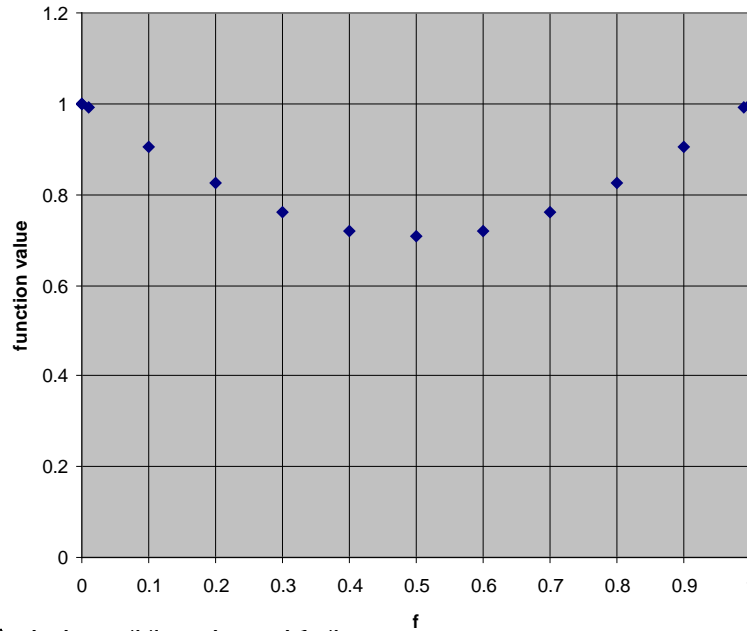


Figure 2: Variation of function with f.

At equal loading the maximum value of L/D for Houck wing is given by equation (7)

$$(L/D)_{\max} = g \cdot (2)^{1/2} (L/D)_{\max\text{standard}}, \quad (7)$$

where $(L/D)_{\max\text{standard}}$ is the maximum L/D for a standard wing.

Wing Analysis:

The performance of various Houck wing configurations is estimated and compared to that of a standard wing using VSAERO simulations. The wings analyzed are depicted in Figure 3. The ratio of L/D for Houck wing to standard wing is plotted. A ratio greater than 1.0 indicates that the Houck wing performs better than the standard wing; whereas a ratio less than 1.0 indicates that the Houck wing does not perform as well as the standard wing. The Houck wing configuration, wing #3 has a span that is half that of a standard wing. The L/D of this wing is only 70% that of the standard wing. Whereas the Houck wing configuration, wing #3 has a span that is 1.6 times that of the standard wing. Houck wing configuration wing #4 has a span that is twice that of the standard wing. The L/D_{\max} of this wing is about 2.5 times higher than that of the standard wing.

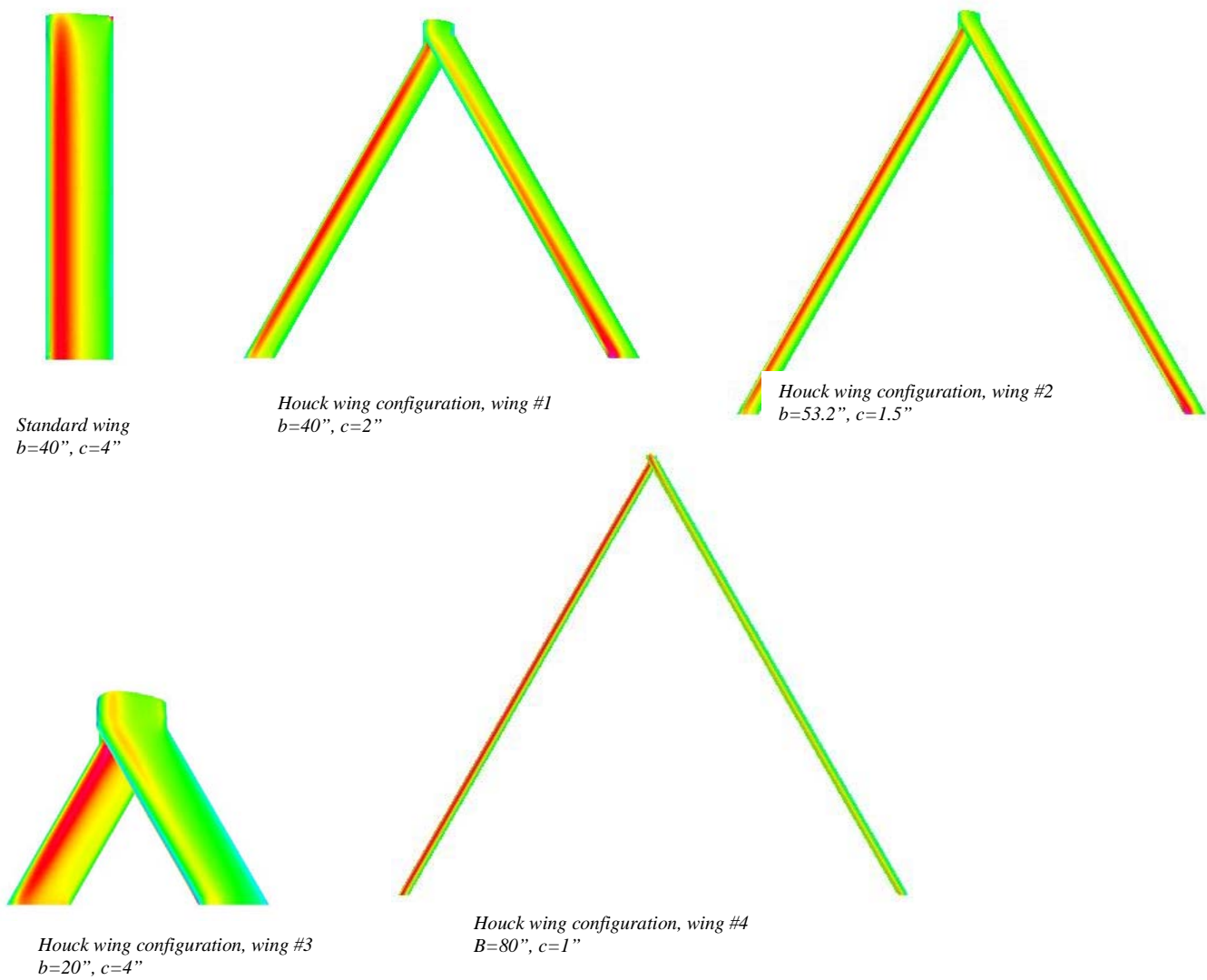


Figure 3: Wing configurations analyzed (half symmetry depicted).

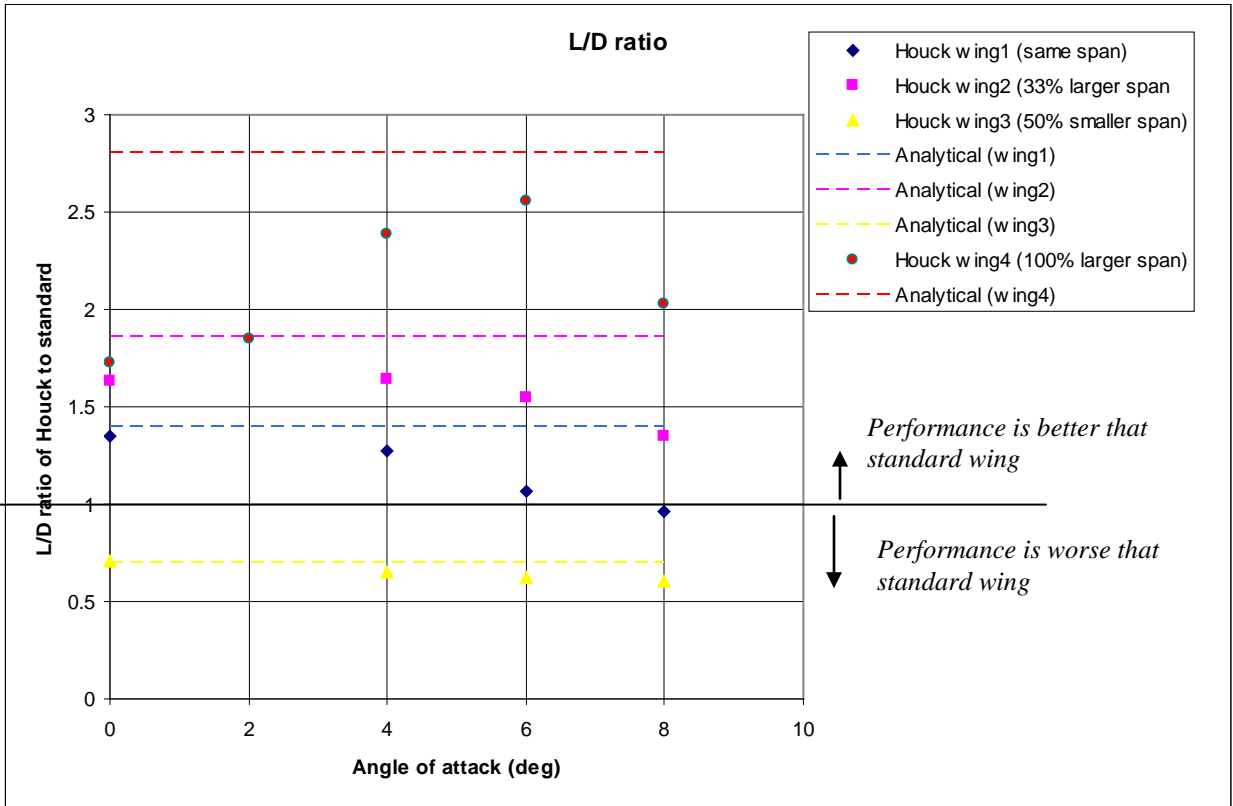


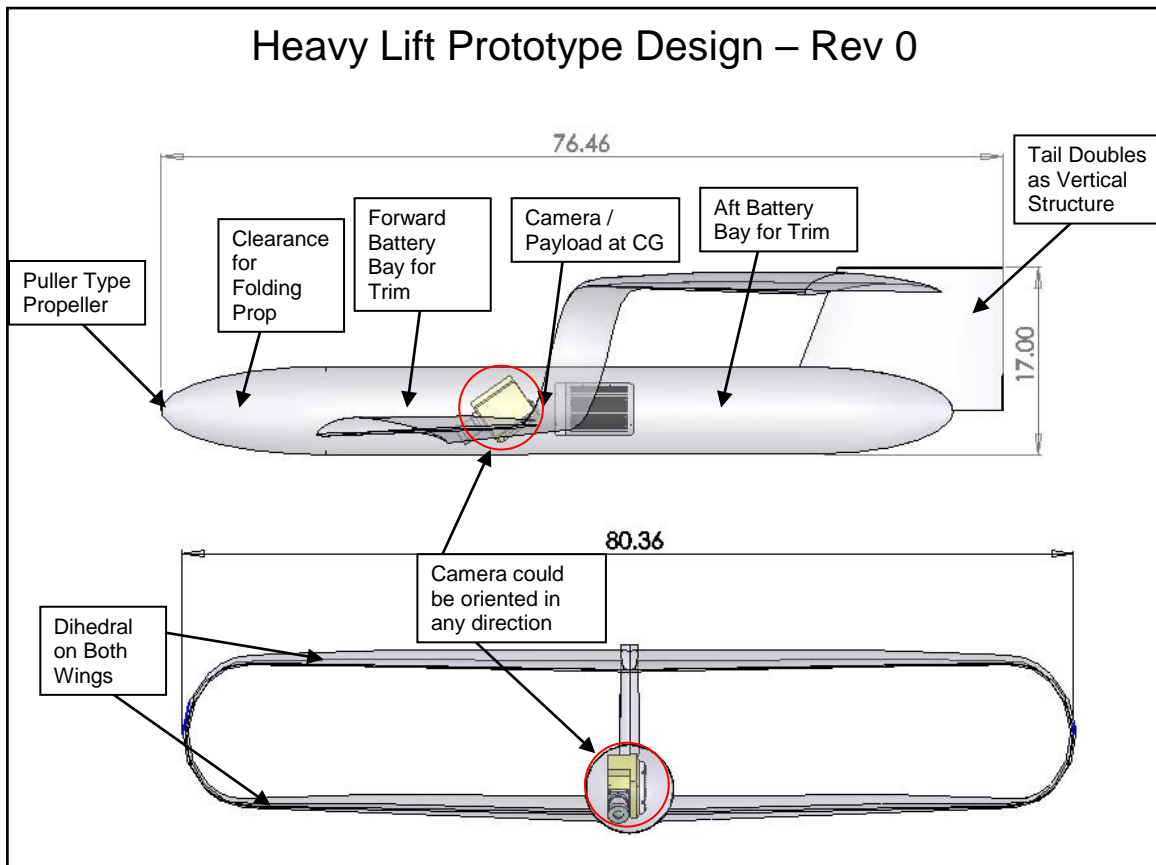
Figure 4: Wing performance.

VSAERO based predictions are also compared to those obtained using equation (7). The agreement with the analytical expression (equation 7) at zero angle of attack is reasonable, at higher angles of attack the value of f is not likely to be close to 0.5 and agreement between the two is not good.

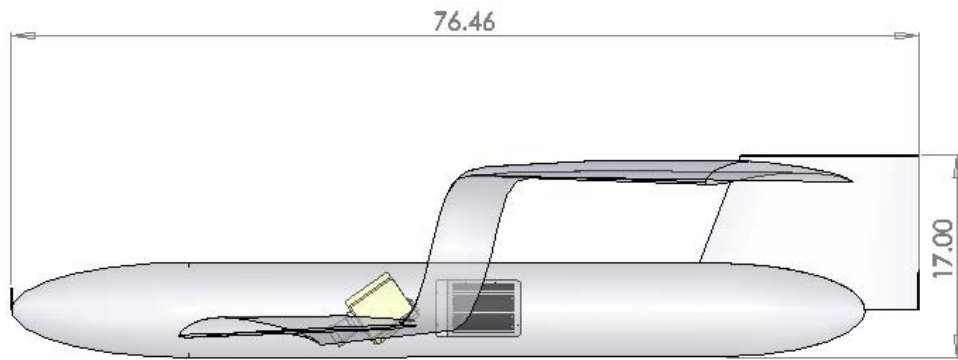
The analysis clearly demonstrates that maximizing the aspect ratio and maintaining equal loading on the two wings results in increased L/D for the Houck wing. High L/D values for the Houck wing are possible.

Appendix F: Houck UAV Prototype Design

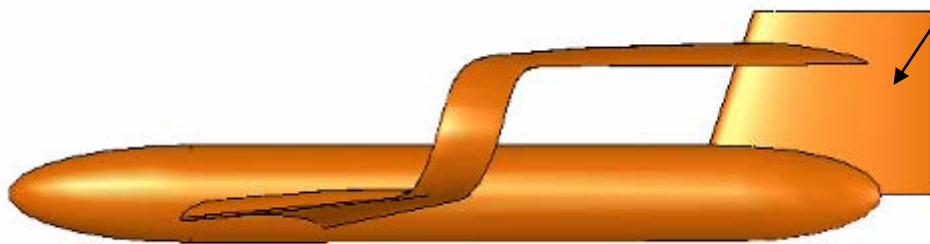
The following pages are duplicates of slides presented by Chris Gillum of Stress Engineering Services, Inc. to the Houck Airfoil Design Team at a meeting on July 19, 2007. These slides illustrate the design of the prototype aircraft and the early construction phase. Internal to the design team, the prototype design was designated “Heavy Lifter Rev.1.”



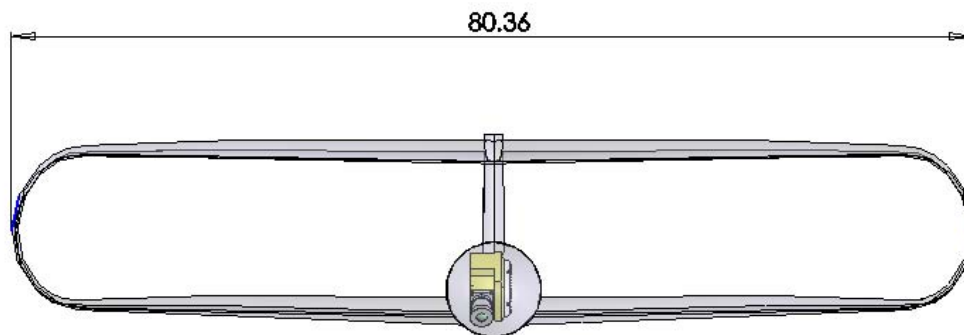
Design Comparison – Rev 0 to Rev 1



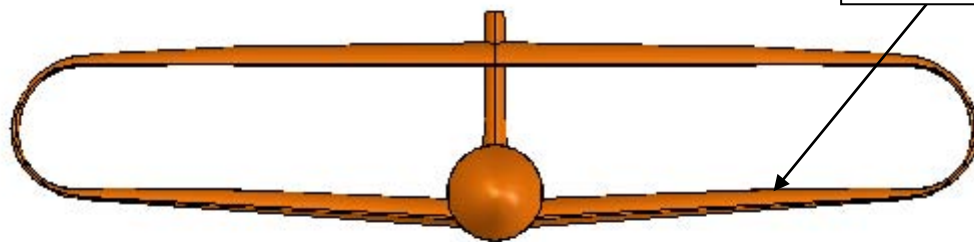
Enlarged Tail



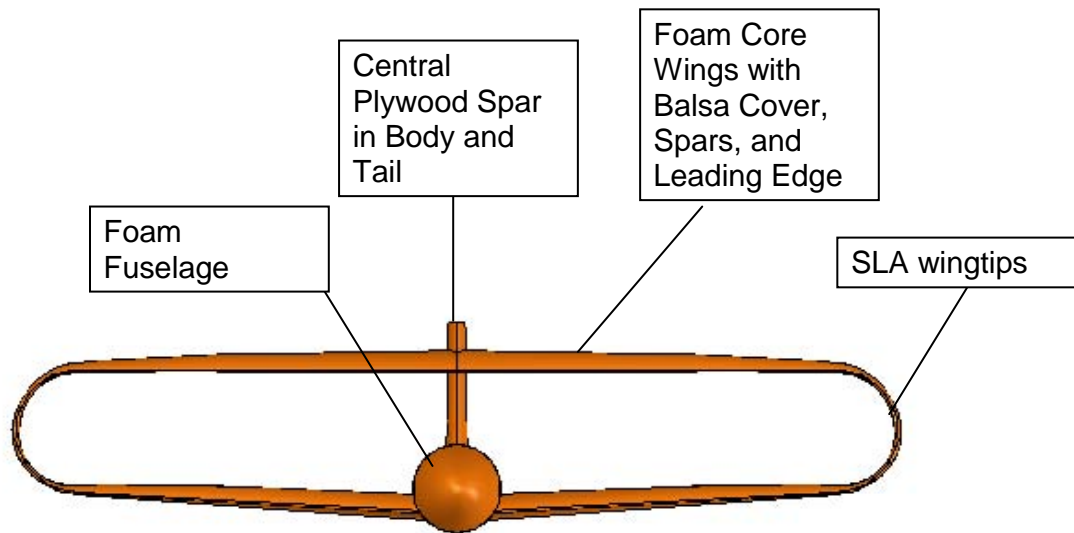
Design Comparison – Rev 0 to Rev 1



Increased Dihedral



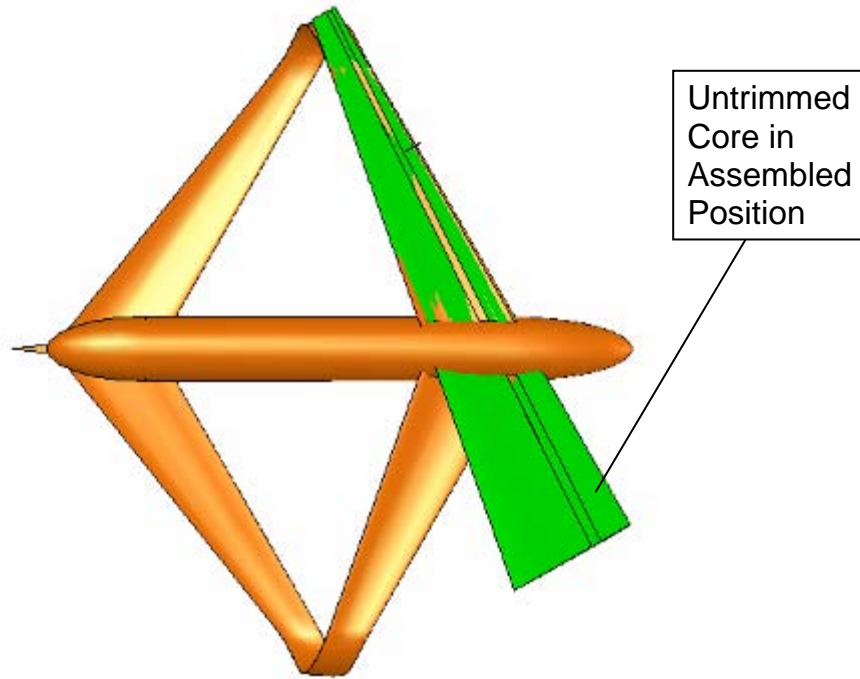
Prototype Construction Plan



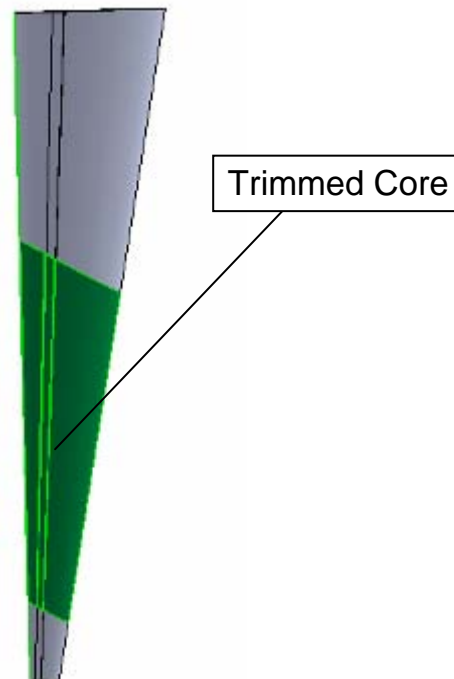
Prototype Construction Effort

- The foam cutter is working and making good cores.
- There are still some software issues being worked out to assist in design changes
- Expect to start prototype construction the week of the July 23rd, after the lift vehicle is complete

Prototype Construction Effort

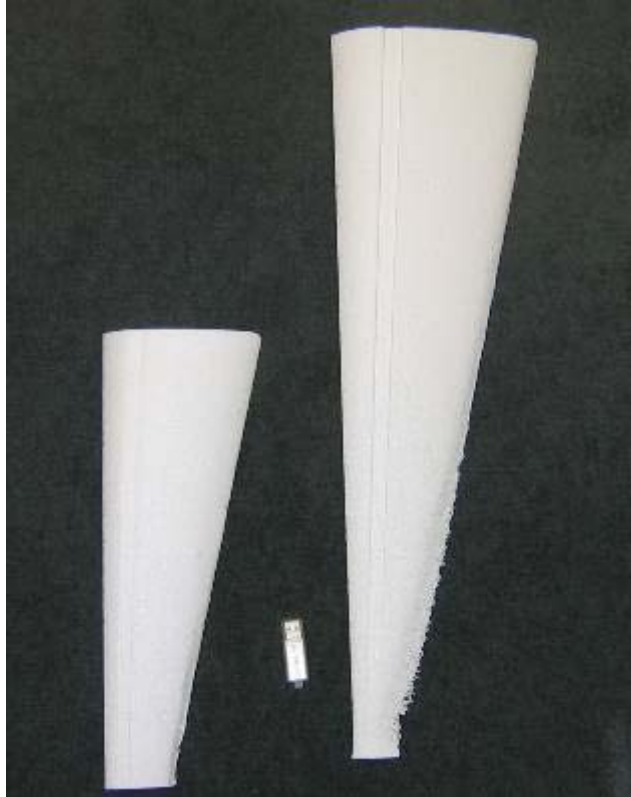


Prototype Construction Effort



Prototype Construction Effort

- Cutting Quality is very speed dependent. Too slow burns the trailing edge, too fast reduces resolution.
- The wings will need to be sectioned to limit speed changes
- Accuracy is quite good, especially on thicker sections



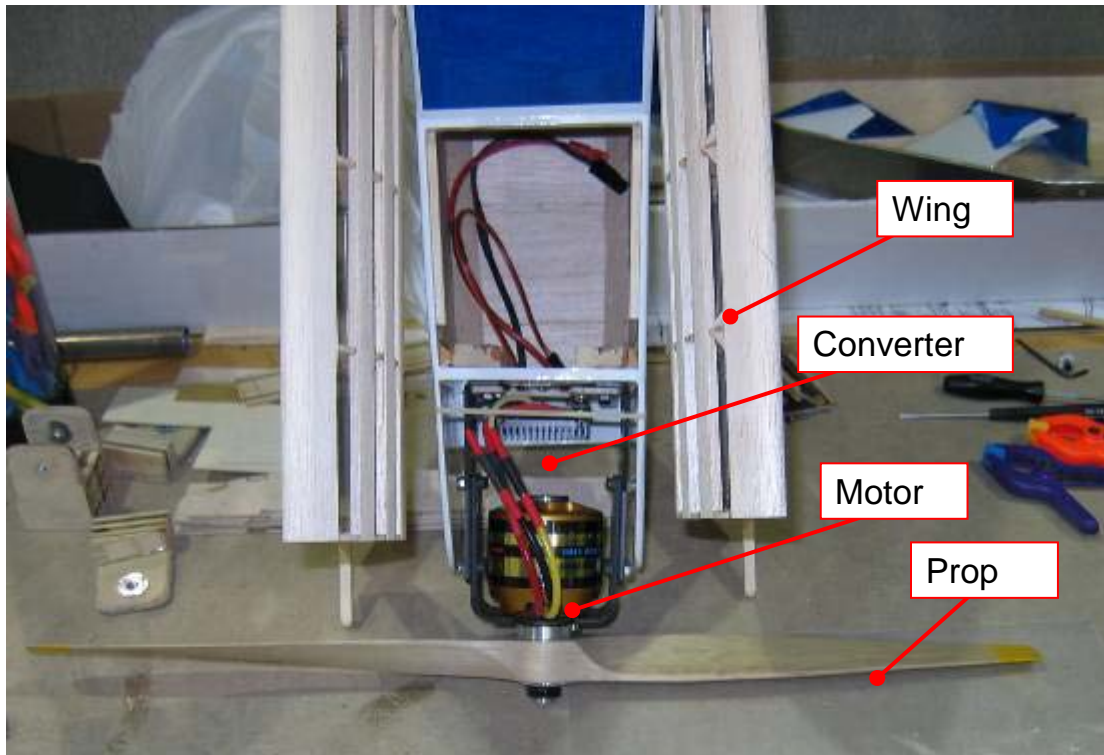
Lift Vehicle Construction Effort

- 95" Telemaster construction nearly complete
- Wings not yet finished
- First flight expected week of July 23
- Have conducted taxi-testing
- Will perform cut-and-try for the release mechanism, plan to attach a servo to the landing gear control

Lift Vehicle Construction Effort



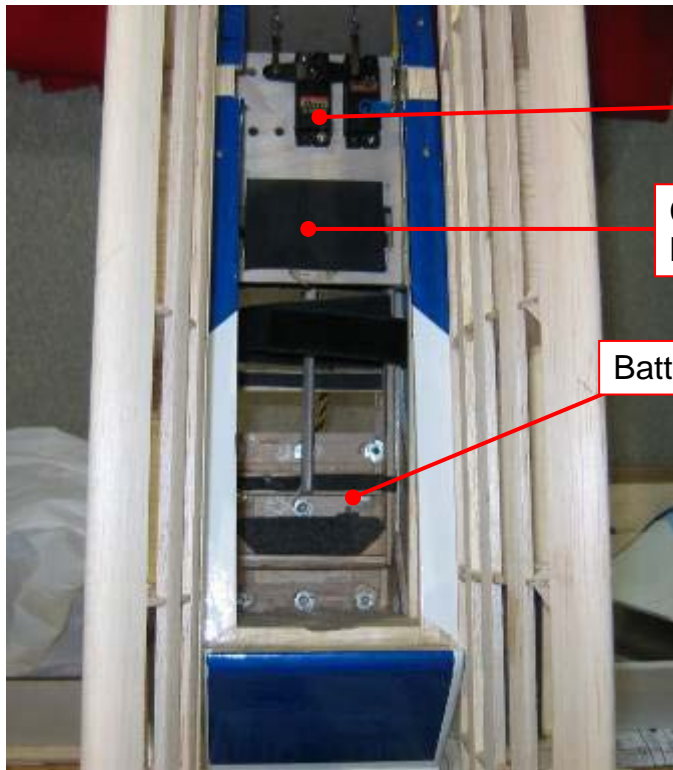
Lift Vehicle Construction Effort



Flight Testing Effort

- Obtained membership to an RC club near Mason with a suitable runway for the Telemaster
- Plan to fly Telemaster there next week
- We can change venue for the prototype if something better is available, or can fly prototype there.

Lift Vehicle Construction Effort



Elevator and
Rudder Servos

Computer
Mount

Battery Bay

Appendix G: Houck UAV Prototype Construction Methodology

The following pages are duplicates of slides presented by Chris Gillum of Stress Engineering Services, Inc. to the Houck Airfoil Design Team at a meeting on August 10, 2007. These slides illustrate the construction methodology of the prototype aircraft.



Houck UAV

Status Report

Chris Gillum
Stress Engineering Services, Inc.

10 August 2007

Houck UAV Prototype Build

- Balsa main spar with birch laminate



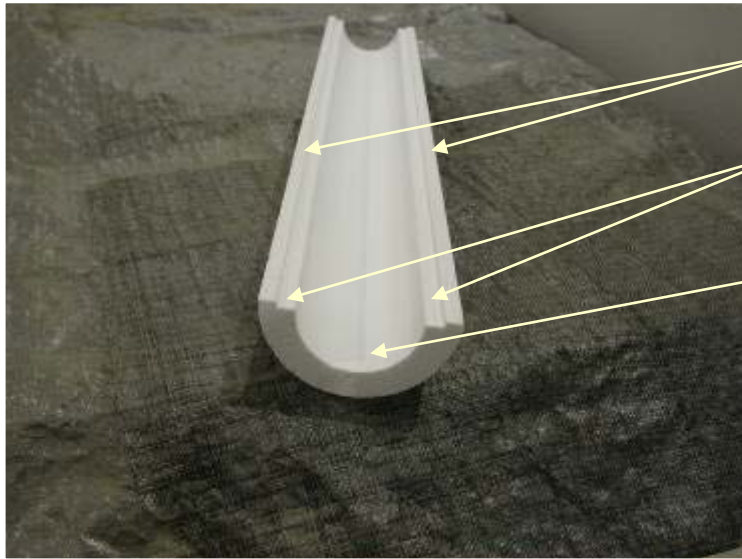
Houck UAV Prototype Build

- Foam core tail section over main spar



Houck UAV Prototype Build

- Fuselage core (half)



Mating
Faces to
Opposite
Half

Center Spar
Clearance

Internal
Clearance

Houck UAV Prototype Build

- Main spar, tail core, half fuselage core



Houck UAV Prototype Build

- Tail core, half fuselage core, nose cone



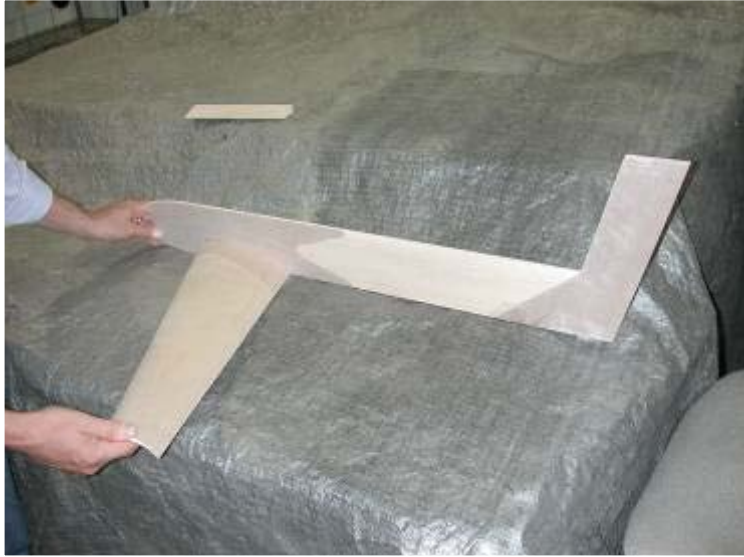
Houck UAV Prototype Build

- Tail core, half fuselage core, nose cone



Houck UAV Prototype Build

- Main spar and foreword left wing mock up



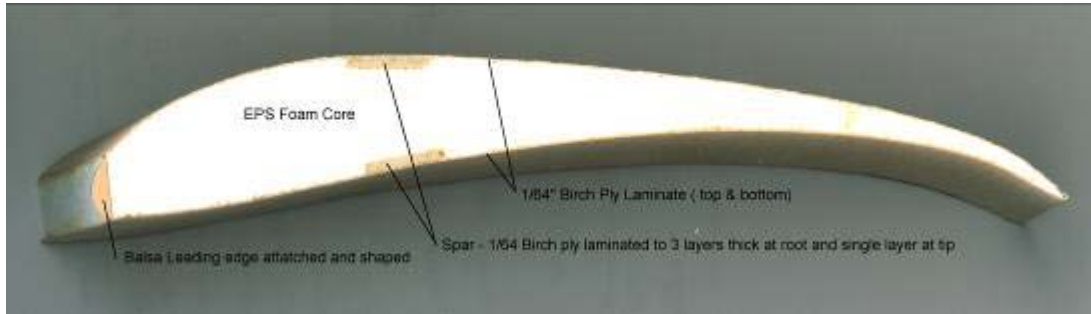
Houck UAV Prototype Build

- Main spar and motor mock up



Houck UAV Prototype Build

■ Wing construction and reference airfoil



Houck UAV Prototype Build

- Wingtip features to be SLA, ordered August 13
- All other components already on-site
- Final assembly underway
- Delivery of prototype anticipated for next status meeting-August 22